THERMODYNAMIC CYCLE MODELING OF INTEGRATED LEAD-COOLED FAST REACTOR AND CONCENTRATING SOLAR POWER

by

Brian T. White

A thesis submitted in partial fulfillment of

the requirements for the degree of

Master of Science

(Mechanical Engineering)

at the

UNIVERSITY OF WISCONSIN–MADISON

2022

Dedicated to my family, I wouldn't be where I am without your words of encouragement, guidance, and inherited rigor.

ACKNOWLEDGMENTS

I would like to thank the world-class knowledge, recommendations, and patience of my advisors Mike Wagner and Ben Lindley. You both gave me the ability to solve problems when I could not see a feasible path forward. I will always look back on my graduate research experience as some of the most challenging and rewarding times of my life, I owe it all to you both.

In addition to my advisors I would like to thank the many outside experts who aided in the completion of this research: Ty Neises from the National Renewable Energy Laboratory, Cory Stansbury and Peter Queenan from Westinghouse Electric Company, and professors Greg Nellis and Mark Anderson from the University of Wisconsin - Madison. Whether you know it or not, the suggestions and expertise you provided allowed me to advance in my research and overcome my many knowledge gaps.

My education gained from undergraduate and graduate studies in the College of Engineering at the University of Wisconsin – Madison, aided me in tackling my problems through a technical and open mind. Thank you to the University for giving me opportunity to be considered for a Mechanical Engineering Masters degree.

Finally, this research would not have been possible without funding from the Department of Energy Office of Nuclear Energy's Nuclear Energy University Program under contract number DE-NE0008988.

CONTENTS

LIST OF TABLES

LIST OF FIGURES

DISCARD THIS PAGE

NOMENCLATURE

Abbreviations

A	Alternator
CIRC	Circulator
CSP	Concentrating solar power
C2S	sCO_2-to-Salt heat exchanger
DOE	Department of Energy
EES	Engineering Equation Solver
FWH	Feedwater heater
HP	High pressure
HPT	High pressure turbine
HTR	High temperature recuperator
HX	Heat exchanger
IES	Integrated energy system
IPT	Intermediate pressure turbine
L	Liquid
LFR	Lead-fast reactor
LP	Low pressure
LPT	Low pressure turbine
LTR	Low temperature recuperator
M	Mixer
MC	Main compressor
MED	Multi-effect Distillation
MMR	Micro Modular Reactor
NREL	National Renewable Energy Laboratory

P	Pump
PC	Pre-cooler
PWR	Pressurized water reactor
RC	Re-compressor
RIE	Reduction in Efficiency
S	Splitter
sCO_2	Supercritical carbon dioxide
S2W	Salt-to-water heat exchanger
SSRC	Supercritical steam-Rankine cycle
T	Turbine
TES	Thermal energy storage
TFR	Throttle Flow Ratio
TTD	Terminal temperature difference
V	Vapor
W2S	Water-to-salt heat exchanger

Variables [Units]

CR	Capacitance ratio [-]
c	Specific heat [kJ/kg-K]
$\dot{C}$	Capacitance rate [MW/°C]
Δ	Temperature difference [°C]
δ	Approach temperature of heat exchanger [°C]
ε	Effectiveness of heat exchanger [-]
η	Isentropic efficiency [-]
h	Enthalpy [J/kg]
$\dot{m}$	Mass flow rate [kg/s]
N	Sub-heat exchanger sections [-]
NTU	Number of transfer units [-]
P	Pressure [Bar]
$\dot{Q}$	Heat transfer rate [W]
T	Temperature [°C]
UA	Conductivity of heat exchanger [MW/°C]
v	Volumetric flow rate [m^3/kg]
$\dot{W}$	Power [MW]
y	Splitter fraction [-]

Subscripts

A	Feedwater heater A
A	Alternator
avg	Average
B	Feedwater heater B
C	Feedwater heater C
c	Cold Fluid
cond	Condenser
CSPHX	Lead-cooled fast reactor heat exchanger
C2S	sCO_2-to-Salt heat exchanger
D	Feedwater heater D
E	Feedwater heater E
F	Feedwater heater F
G	Feedwater heater G
gen	Generated
h	Hot fluid
heatstorage	TES heat storage
HP	High pressure pump
HPT	High pressure turbine
HTR	High temperature recuperator
HX	Heat exchanger
i	Index
in	Inlet
IPT	Intermediate pressure turbine
LFR	Lead-cooled fast reactor

LFRHX	Lead-cooled fast reactor heat exchanger
LP	Low pressure pump
LPT	Low pressure turbine
LTR	Low temperature recuperator
max	Maximum
MC	Main compressor
min	Minimum
out	Outlet
PC	Pre-cooler
$pump$	Pump
RC	Re-compressor
$surr$	Surrounding
T	Turbine
t, exh	Turbine exhaust

ABSTRACT

Renewable technologies such as solar, have innate problems with low solar irradiance caused by cloud coverage, seasonal changes, and time of day. Low solar irradiance reduces the available power output of solar power plants, therefore requiring thermal energy, battery, or potential energy storage systems to be flexible to grid demand. With high fixed costs and low operating costs, nuclear power plants often operate at full capacity acting as base loads for the electrical grid. The ability to load follow, adjusting the power plant's output according to grid demand, is a possibility, but is often not financially appealing. Therefore, load following for the electrical grid is typically accomplished with fossil fuel plants like coal, natural gas, or petroleum.

In this thesis, potential synergies through coupling of complementary solar and nuclear technologies with energy storage are explored. Lead-cooled fast reactor (LFR) and concentrating solar power tower (CSP) technologies are considered due to their similar operating temperatures and, consequently, the ability to utilize shared thermal energy storage (TES). Implementing TES within a coupled CSP and LFR power cycles allows for either technology to store thermal energy during low grid demand periods and increase power production during high demand periods, effectively increasing dispatchability. To investigate the integration of LFR and CSP technologies, two power cycle types are considered: supercritical carbon dioxide recompression Brayton cycle and supercritical steam-Rankine cycle.

Three cycle configurations for supercritical carbon dioxide recompression Brayton are studied: two-cycle configuration, which uses CSP and LFR heat for dedicated turbocompressors, has the highest efficiencies of the studied configurations but with less component synergies; a combined cycle with CSP and LFR heat sources in parallel is the simplest with the lowest efficiencies; and a combined cycle with separate high temperature recuperators for both the CSP and LFR is a compromise between efficiency and component synergies. Additionally, four thermal energy storage charging techniques are studied: the turbine positioned before CO_2-to-Salt heat exchanger, requiring a high LFR outlet temperature

for viability; the turbine after the CO_2-to-Salt, reducing turbine inlet temperature and therefore power; the turbine parallel to the CO_2-to-Salt producing moderate efficiency; and a dedicated circulator loop offering flexibility and high heat storage efficiency but increased cost.

The supercritical steam-Rankine cycle studies examine a cycle with three modes of operation. The modes of operation are as follows: 'off', the LFR is the sole heat input into the cycle operating as a typical supercritical Rankine cycle; 'discharging' where the TES is transferring heat into the cycle to increase steam mass flow rate; and 'charging', heat from the turbine exhaust is being stored in TES for later dispatch. In addition to the on-design modes of operation, the quantity of steam mass flow in 'discharging' mode and the salt mass flow in 'charging' mode are adjusted from the design specifications in an off-design study to investigate the affects of TES storage on the performance of the cycle. Results indicate 508 MW of power generation with 52.53% efficiency efficiency in 'off' mode of operation. In the 'Charging' mode of operation salt is being stored in the hot TES decreasing power generation and cycle efficiency. The 'Discharging' mode of operation increases steam mass flow rates and power generation while reducing cycle efficiency due to dissimilar temperature heat sources. The total power generation range of the supercritical steam-Rankine cycle while LFR remains full-capacity operation is 477.1 MW to 587.8 MW.

Comparisons between the supercritical carbon dioxide Brayton recompression cycle configurations and supercritical steam-Rankine cycle are drawn. The supercritical steam-Rankine cycle has similar LFR and CSP synergies with higher power generation and cycle efficiencies than the supercritical carbon dioxide Brayton cycle configurations. Therefore, the supercritical steam-Rankine cycle is the preferred option for future studies.

1 INTRODUCTION

1.1 Motivation

The United States produced approximately 4,116 billion kWh of energy in 2021 with fossil fuels, comprised of natural gas, coal, and petroleum, accounting for 60.8% of total energy production. The amount of energy produced by nuclear energy was 778 billion kWh, or 18.9%, and solar thermal was 3 billion kWh, or 0.1% [2]. Despite the climate, energy security, and health consequences, burning fossil fuels for thermal or electrical generation is still prevalent due to the lack of alternative energies, flexibility to grid demand, and lower associated costs. Renewable energy technologies such as wind and solar photovoltaic can incorporate battery energy storage systems, but with high additional cost for installation and maintenance, the storage amount is economically limited. As a consequence, when grid demand is low, renewable technologies without energy storage are forced to curtail production to reduce electrical power generation thereby wasting energy.

TES — in industrial settings — costs less per-kWh of energy storage while having larger discharge duration when compared to battery storage [3]. Solar thermal energy technologies typically incorporate TES, allowing for dependable energy production during low solar irradiance and high grid demand, then storing thermal energy during high solar irradiance and low grid demand periods for later use. Nuclear energy can load follow, increasing or decreasing power output as needed, but with high upfront fixed costs and relatively low operating and fuel costs, most nuclear plants remain at full-capacity operation acting as a base load for the grid with more flexible energy sources like coal or natural gas providing load following. A novel solution addresses the drawbacks of renewable and nuclear energy by combining complementary heat sources with similar operating temperatures — specifically CSP and LFR — into a single synergistic cycle. In the combined cycle, when grid demand is lower than the LFR base load, excess heat from the LFR can be stored in the TES simultaneously with heat from the CSP, to be dispatched at a

later time. The CSP in isolation produces less energy if the solar irradiance is low, but when coupled with the LFR, the TES can still be thoroughly utilized. The heat stored in the TES, charged by the LFR and CSP, is dispatched to the cycle during high grid demand periods, increasing cycle generation. This capability allows for the LFR to operate at full-capacity while the cycle load-follows with stored thermal energy in the TES in place of fossil fuel alternatives.

Integrated solar-nuclear power plants have been studied in prior literature with an emphasis on either being fossil fuel alternatives to fuel production or a single cycle configuration analysis without included nuclear TES charging capabilities. Therefore, there is a need in literature for a comparison of cycle types and configurations while integrating solar-nuclear with thermal energy storage. To study the integration these solar-nuclear technologies, this thesis produces thermodynamic cycle modeling and comparison for combined CSP-LFR with TES for two dissimilar cycle types: supercritical carbon dioxide Brayton and supercritical steam-Rankine. These models will serve as the power cycles in a larger integrated energy system (IES) where the cycle receives CSP and LFR performance maps and generates waste heat and electrical generation maps for multi-effect distillation process and electrical power grid simulations. Additionally, the IES has potential to save cost with the LFR and CSP sharing a single power block, grid interconnect, and transmission. Background information on the associated CSP, LFR, and TES technologies and the two cycle types, sCO_2 Brayton and SSRC, are provided in the following sections.

1.2 Concentrating Solar Power

CSP has four primary technologies: linear Fresnel, parabolic dish, parabolic trough, and tower power. The power tower configuration is the subject of the CSP technology investigated in this thesis due to its direct integration with molten salt TES. A diagram outlining a conventional CSP tower is illustrated in Figure 1.1.

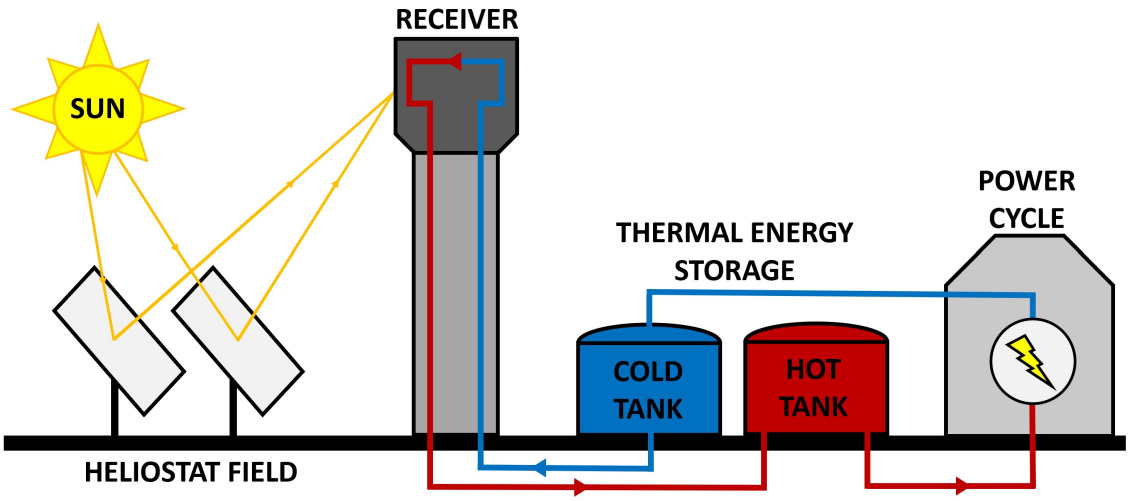

Figure 1.1: Diagram of concentrating solar power tower plant with thermal energy storage.

CSP tower technologies with TES are typically made up of four primary components: heliostat field, receiver, thermal energy storage, and power cycle. The heliostat field, comprised of an array of mirrors with controlled axes to adjust focus according to the sun's position, is responsible for reflecting and concentrating solar irradiance from the sun to the receiver. In the receiver, the concentrated solar irradiance is absorbed by a heat exchanger and transferred to the cold molten salt pumped to the receiver at the pinnacle of the tower. The now heated molten salt flows to the hot storage tank in the TES system. When the plant is producing power, hot molten salt is pumped from the hot storage tank in the TES to the power cycle where heat is extracted and converted to electrical power. The now cold molten salt is stored in the cold storage tank in the TES where, when demanded, it is pumped back to the top of the receiver and the cycle repeats. If the CSP is required to provide electrical generation throughout a 24-hour day cycle, 10-16 hours of TES molten

salt storage is typically included to meet demand [4].

1.3 Lead-cooled Fast Reactor

In nuclear reactors, controlled nuclear reactions produce heat. Lead-cooled fast reactors are a subcategory of nuclear reactors where the nuclear fuel is cooled by a submerged high temperature pool of flowing liquid lead that circulates throughout the reactor exchanging heat with both the nuclear core and power cycle. The LFR considered in this thesis is designed by Westinghouse Electric Company and has an outlet temperature compatible with molten salt TES [5]. A simplified diagram of the Westinghouse LFR is displayed in Figure 1.2.

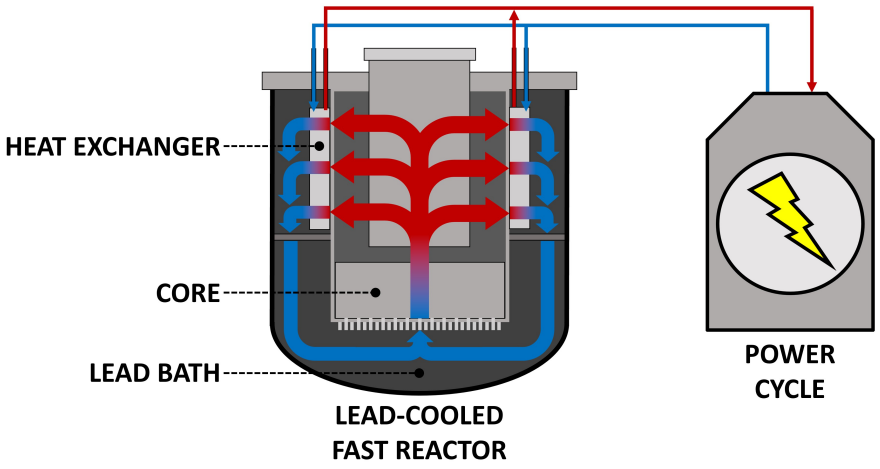

Figure 1.2: Cross section diagram of lead-cooled fast reactor.

The LFR operates by pumping (pumps not shown in Figure 1.2) the liquid lead through the base of the core. The core undergoes a heat-producing nuclear reaction while being cooled by the liquid lead passing through it. The heated lead from the core is forced radially through the microchannel heat exchangers encompassing the core barrel. The microchannel heat exchangers transfer heat to the working fluid of a power cycle where it is transformed into electrical power. The cooled liquid lead outlet from the heat exchangers is then recirculated by the pumps to the base of the core barrel where the process is repeated.

1.4 Thermal Energy Storage

Presently, the notable TES techniques are: (i) sensible (single-phase) storage wherein the heat transfer medium is used for storage at constant-phase form of liquid, solid, or gas; (ii) thermochemical wherein energy is stored as chemical energy in a chemical looping process; and (iii) latent heat wherein energy is stored during a material phase change at constant temperature. For a complementary CSP-LFR cycle, the TES technology must be operable within the range of the CSP and LFR operating temperatures. Therefore, two-tank sensible storage is considered with the storage medium of liquid solar salt, or 60% $NaNO_3$ – 40% KNO_3. The temperature at which solar salt can be stored is restricted to the freeze and decomposition temperature range, with commercial solar thermal plants having temperatures around 350 °C to 565 °C. TES contains several components with two storage tanks, hot and cold defined by their relative temperatures, pumps to circulate the molten salt, and heat exchangers to transfer heat into and out of the salt loop.

1.5 Brayton Cycle

Supercritical carbon dioxide (sCO_2) Brayton cycles are promising cycle configurations offering higher efficiencies, compact design, and reduced turbomachinery cost while operating with non-toxic working fluid. sCO_2 closed Brayton cycles, operating at turbine inlet temperatures of 650 °C - 750 °C, have been modeled and experimentally tested to cycle efficiencies of 50%, allowing these cycles to be a competitive alternative to steam-Rankine and air-Brayton cycles over a range of temperatures. Brayton cycles operate with a constant gas phase working fluid and are designed — depending on the use case — in two types: open and closed. Open Brayton cycles indicate that the working fluid (typically air) enters the cycle through an intake and is compressed, heated, expanded in the turbine, then exhausted from the cycle. The heating process in open Brayton cycles is commonly accomplished by combustion of fuel mixed with the intake air. In the research presented

in this thesis, all Brayton cycles are of the closed type. Closed Brayton cycles recycle the working fluid and can achieve higher pressures, both of which are required for the sCO_2 operation. Additionally, closed Brayton cycles use external heat sources, introducing heat into the cycle through heat exchangers instead of combustion gases, reducing turbine blade erosion and heat exchanger fouling. A simple diagram of a closed Brayton power cycle is illustrated in Figure 1.3.

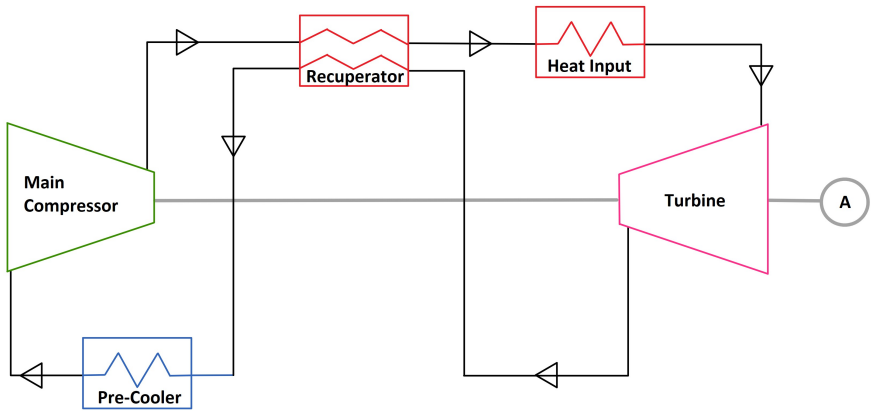

Figure 1.3: Simple closed Brayton power cycle with single recuperator.

This simple closed Brayton cycle performs multiple operations on the working fluid to produce electrical energy. The sCO_2 enters the main compressor (MC) where the pressure is mechanically increased to the high pressure side of the cycle. As the high pressure sCO_2 flows through the recuperator, waste heat is recovered from the hot turbine exhaust, pre-heating the sCO_2 before the main heat input. The sCO_2 enters the heat input heat exchanger and the temperature is increased to turbine inlet requirements. The turbine expands the high pressure and temperature sCO_2 through a series of blade stages transforming heat energy into mechanical energy. The turbine is connected to a shaft providing mechanical energy to the compressor and alternator, generating electricity. The sCO_2 exits the turbine to the low pressure side of the cycle at a relatively lower temperature and supplies pre-heating through the recuperator to the high pressure sCO_2 entering the heat input. The sCO_2 flow then has waste heat removed through the pre-cooler, reducing temperature to an acceptable level for the MC to compress and recycle the fluid. Modifications to this

simple Brayton cycle, including additional recuperative heat exchangers and compressors, allow for increases in cycle efficiency with the drawback of added complexity and cost.

1.6 Steam-Rankine Cycle

Steam-Rankine cycles are established cycle designs used in many applications including coal-fired, solar thermal, nuclear, and geothermal power production. While in operation, the working fluid (water) is vaporized by the steam generator, passed in the gaseous phase through turbines, has waste heat removed and condensed back to liquid, and then pumped again in liquid phase to the steam generator repeating the process. The supercritical steam-Rankine cycle (SSRC), operating at pressures above 220 Bar or the critical point of water, typically have increased cycle efficiencies due to higher temperature operation and no latent heat cost in the boiler. In Figure 1.4, a simple Rankine cycle is displayed for reference.

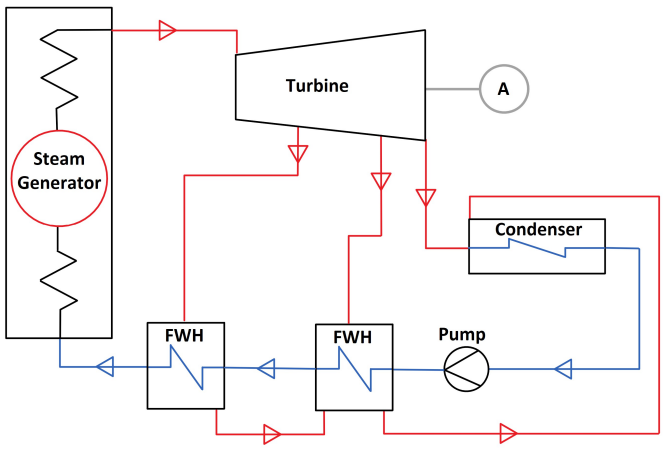

Figure 1.4: Simple Rankine power cycle containing two feedwater heaters with drains pumped backwards.

In the simple subcritical Rankine cycle liquid-state feedwater enters the steam generator where the fluid experiences a phase change to steam. The dry saturated steam can then be further superheated. The superheated steam enters the turbine where the flow is expanded through a series of turbine blades. The turbine shell has extraction points were a fraction of high quality steam flows from the turbine to the feedwater heaters (FWH).

The purpose of the two FWHs in Figure 1.4 is to gradually preheat the feedwater from the low temperature outlet of the pump to the higher temperature inlet of the steam generator. Preheating of the feedwater via FWHs increases the cycle thermodynamic efficiency by reducing the temperature rise across the steam generator and therefore reducing heat transfer irreversibilities [6]. In the FWH, the extracted high quality steam transfers heat to the feedwater, condensing and subcooling, and then flows through the drain to the next, lower pressure, feedwater heater. After the extractions, the main steam flow exits the final stage of the turbine and recombines with the drains from the feedwater heaters before the condenser removes waste heat and fully condenses the flow. The flow is then pumped through the feedwater heaters and is preheated in the FWHs by the turbine extractions before entering the steam generator and repeating the cycle.

1.7 Objective and Scope

The research presented in this thesis aims to develop reference configurations for, and outline synergies and challenges associated with, combining LFR and CSP technologies with shared TES. To accomplish this task, multiple promising cycle configurations are modeled and tested, sCO_2 recompression Brayton cycle and SSRC, to outline the advantages or drawbacks of each. Additionally, performance metrics of the various cycle configurations studies are discussed with emphasis on cycle efficiency, power output, heat rejection, and TES usage. The scope is limited to thermodynamically accurate cycle design, performance metrics, and interaction of coupled technologies with TES. Exhaustive off-design analysis of CSP and LFR performance, further development of component modeling, and economic and dispatch analysis are out of the scope of this thesis and are subjects of future or other ongoing research.

2 LITERATURE REVIEW

Research undertaken in this thesis pertains to complementary LFR and CSP with TES modeling in two dissimilar power cycle technologies: sCO_2 Brayton cycle and SSRC. This section will first review publications related to sCO_2 Brayton cycles, then SSRC, and finally comparison studies between the two cycles.

Various sCO_2 Brayton cycles have been modeled in literature, with the recompression cycle having efficiency advantages over other proposed cycle arrangements in solar and nuclear applications [7, 8, 9]. The recompression cycle can reach efficiencies of 50% in some scenarios (with turbine inlet temperatures in the 650–750 °C range), allowing these cycles to be a competitive alternative to steam Rankine and air Brayton cycles over a range of temperatures [7, 10]. Due to the benefits of sCO_2 Brayton cycles, the United States Department of Energy is investigating these conversion cycles for use with heat sources including nuclear and solar [11]. Multiple research funding opportunities have been established [12], with the National Energy Technology Laboratory offering $144M award for demonstration and performance verification of a sCO_2 Brayton cycle [13] and the Office of Energy Efficiency Renewable Energy offering $2.6M award in their Brayton Energy project for a integrated concentrating solar power (CSP) receiver, thermal energy storage (TES), and power block in one sCO_2 Brayton system [14]. Previous research has modeled CSP technology as the thermal source for Brayton sCO_2 cycles with promising results in efficiency gains and high temperature thermal energy storage [7, 9, 15, 16, 17, 18]. Thermal energy gathered from the CSP is stored and can be dispatched into the sCO_2 Brayton cycle when grid demand increases. With comparable temperature to the hot TES, 560 °C, a lead-cooled fast reactor (LFR) is capable of transferring heat to thermal storage for later dispatch. An LFR uses fission reactions to heat a heat transfer fluid — in this case liquid lead — to 650 °C. Nuclear sCO_2 Brayton cycles have been studied with similar gains in efficiency seen in CSP sCO_2 Brayton cycles [19, 20]. Physical testing of simple sCO_2 Brayton

cycles has been performed at Sandia National Laboratories [21] and in Korea [22], with at least three commercial companies (Echogen, Net Power, and Heliogen) having progressed to building pilot cycles [23, 24, 25].

Various studies on complementary solar-nuclear systems have been carried out:

- Monnerie et al. (2011): In search of an alternative to the typical fossil fuel-based process, reports on synthesizing hydrogen with complementary solar-nuclear technologies being utilized as consistent heat sources for chemical decomposition of sulphuric acid to aid in simple, low-temperature electrolysis [26].

- Curtis J.D. (2015): Massachusetts Institute of Technology thesis reports cycle configuration, performance, and development of complementary solar-nuclear systems with a focus on shale oil extraction and production from kerogen deposits [27].

- Wang et al. (2020): Implements a combined solar and nuclear plant discussing a sCO_2 Brayton recompression cycle layout with an emphasis on a cycle design's performance to varying solar irradiance and demonstration of feasibility [28].

- Son et al. (2021): Study on modeling and the feasibility of complementary CSP and KAIST Micro Modular Reactor (KAIST-MMR) in a sCO_2 power cycle with TES for island microgrids [29].

The economic and physical feasibility of producing shale oil and hydrogen with complementary solar-nuclear cycles, as discussed in the Curtis J.D. (2015) thesis and Monnerie et al. (2011) article, is not within the scope of sCO_2 Brayton recompression cycle electrical generation and storage presented in this thesis.

The single cycle configuration in Wang et al. (2020) has a higher-temperature operating salt, 67% KCl-33% $MgCl_2$, as the heat transfer fluid in the CSP which is capable of temperatures in the range of 450–1400 °C. The lower operating point of the studied solar salt in this thesis, 60% $NaNO_3$-40 %KNO_3, with a temperature range of 250–585 °C, is

employed because the technology is more established when compared to KCl-$MgCl_2$ [30]. The higher temperature salt requires preheating which is achieved prior to the CSP heat addition by a small modular lead-cooled fast reactor. The small modular LFR operates at a low temperature and a fixed location when compared to the higher temperature lead and variable location that the studied Westinghouse LFR is capable of. Due to the similar operating temperatures of the CSP and LFR, multiple cycle configurations are studied that are not possible with the similar components in Wang et al. (2020).

Power production for island micro grids by utilizing complementary CSP and MMR with TES in a single sCO_2 cycle is studied in Son et. al. (2021). The presented research focuses on a micro reactor, with a 20 year refueling timeline, acting as a base load while the CSP with TES inject additional heat to meet peaking demand [29]. The nuclear reactor does not have TES charging capability due to the KAIST-MMR's dissimilar operating temperatures while the studied cycle has the TES providing reheating after the primary turbine, distinguishing this studied cycle and components from the research in this thesis.

Steam Rankine cycles with nuclear reactors as the primary heat source may include a form of TES to increase adaptability to grid demand. F. Carlson et. al (2019) describes that instabilities caused by renewable energies can be amended by adding TES capability to a nuclear subcritical steam-Rankine cycle, allowing these base load power sources to discharge and charge TES, adjusting power output to grid demand [31]. Further analysis of nuclear with TES is conducted by the same primary author, F. Carlson and J. Davidson (2021), including detailed descriptions of parametric studies, cost performance, and multiple cycle arrangements [32]. The thermal energy storage technologies studied in these articles are latent heat storage and sensible storage; without considering molten solar salt storage or a CSP TES charging capability. An article which studies a combined solar and gas-fired supercritical steam-Rankine cycle with TES is L. Meroueh and G. Chen (2020). The thermal energy storage in this research is molten silicon which is either electrically charged by a photovoltaic plant or thermally charged by a gas-peaking boiler. The TES

can be discharged, heating additional steam prior to the intermediate pressure turbine, increasing the power production and grid flexibility of the plant [33]. These three studies contain forms of TES with similar steam-Rankine power plant design but do not consider solar thermal and nuclear integration with molten salt TES.

Studies modeling coupled solar-nuclear technologies in a Rankine cycle often lack the capability to charge the TES. In three studies, a small nuclear power source provides heating to the feedwater until the steam reaches saturated vapor conditions where additional superheating and reheating is accomplished by salt to water heat exchangers intermediate to the solar salt storage tanks. G. Wang and J. Yin model and evaluate parabolic trough solar-thermal in combination with a small pressurized water reactor (PWR) [34]. Design and modeling of a hybrid CSP and small PWR is accomplished in D. Popov and A. Borissova [35] with an economic analysis of an identical power cycle accompanied by waste heat desalination was produced by G. Wang et. al [36]. The three aforementioned studies do not consider TES charging capability via the small PWR, have dissimilar solar-thermal and nuclear technologies, desalination occurs via a heat exchanger internal to the CSP salt cycle, and the steam-Rankine cycle is subcritical, differentiating these models from the SSRC design. B.C. Zhao et. al performed analysis on a combined solar-nuclear power system with a small modular reactor capable of charging a single tank packed-bed TES, as opposed to two tanks for cold and hot storage [37]. The packed bed TES is the exclusive provider of thermal power to the subcritical steam-Rankine cycle, while the small modular reactor and CSP are not directly exchanging heat into the cycle but instead act as peripheral thermal sources through TES charging.

Comparison studies between the sCO_2 Brayton and steam-Rankine types are now reviewed. Coal-fired sCO_2 Brayton and ultra-supercritical steam-Rankine cycles have been investigated by J. Miller et. al (2017) to gain insight into efficiency and cost comparison between state-of-the-art cycles. In this article, the performance and cost models of four sCO_2 Brayton cycles are developed and compared against similarly-sized steam cycles

published by the DOE/National Energy Technology Laboratory [38]. A study by J. Xu et. al (2021) performed economic and thermodynamic comparisons between coal-fired sCO_2 Brayton and ultra-supercritical steam-Rankine cycles. This study observed comparable cycle efficiencies with the sCO_2 cycle being more economically and thermodynamically attractive [39]. With a focus on a single coal-fired heat input and plant economics, these two articles are dissimilar to the performance comparison of combined LFR and CSP with TES cycles modeled in this thesis.

Similarly to coal-fired, multiple comparisons between SSRC and sCO_2 Brayton have been accomplished for CSP or nuclear heat inputs. V. Cheang et. al (2015) models three sCO_2 Brayton cycle configurations and compares against two steam-Rankine cycles: commercial CSP superheated steam-Rankine and fossil-fuel SSRC. This study concludes that both of the steam-Rankine cycles are more thermodynamically efficient and cost effective when compared to the sCO_2 Brayton alternatives, mostly due to the transient nature, corrosion resistance, and increased complexity [40] of CSP. An additional study compares transcritical sCO_2 and steam-Rankine for CSP applications in P. Garg et. al (2014). This study found similar efficiency results for the two dissimilar power cycles. The published conclusions by P. Garg et. al indicate that sCO_2 cycles accept a wider range of source temperatures, have more compact turbomachinery, but require larger solar fields while steam-Rankine cycles operate at lower temperatures, but contain larger turbomachinery and require multiple recuperative processes [41]. Cycle comparisons of sCO_2 Brayton, helium Brayton, superheated steam-Rankine, and SSRC with liquid salt or liquid metal nuclear reactors are investigated in V. Dostal et al. (2006). This article examines the thermodynamics, plant cost, optimization, and integration into nuclear of the various cycles. The results indicated that sCO_2 is the most compatible to nuclear with potential for capital cost reductions while operating at a lower temperature and high efficiencies [42]. These previous studies on sCO_2 Brayton and steam-Rankine do not incorporate combined CSP and Nuclear with TES integration, but do provide insight into the idiosyncrasies of cycle configurations when

coupled to Nuclear or CSP heat sources.

3 SUPERCRITICAL CARBON DIOXIDE BRAYTON CYCLES

3.1 Introduction

sCO_2 Brayton cycles are promising cycle configurations offering higher efficiencies, compact design, and reduced turbomachinery cost while operating with non-toxic working fluid. Utilizing complementary technologies such as solar concentrating power and lead-cooled fast reactors can offset the drawbacks of each. These drawbacks include CSP dependency on weather conditions and time of day, while the LFR in isolation does not incorporate thermal energy storage for meeting peak demand. Coupling these technologies into an interconnected cycle allows for consistent weather-independent generation, cycle component sharging, and thermal storage for high dispatchability during high grid demand periods. A CSP has an array of mirrors concentrating solar rays towards a tower receiver, transferring the energy into a solar salt, and storing the solar salt in tanks. CSP systems require direct sunlight to operate at full power therefore causing variability based on weather conditions and time of day. This chapter specifically studies the effects of dissimilar cycle configurations on cycle efficiency — defined as the total power generated by the cycle divided by the heat inputs — and heat storage efficiency — defined as the quantity of heat transferred to storage divided by the total heat input. In this work, the LFR serves a dual purpose of providing heat for electrical generation and for supplementary CSP TES charging. This chapter provides an overview of contending recompression sCO_2 Brayton cycles with varied positioning of complementary CSP and LFR heat additions in the cycle. Additionally, the location of TES heat extraction from the sCO_2 Brayton cycles is studied with the results discussed.

3.2 Materials and Methods

Cycle Component Modeling

Components present in the cycles are modeled using various techniques and are discussed in more detail below. Turbines and compressors are analyzed using isentropic efficiencies. Counter-flow heat exchangers (HX) are modeled using the effectiveness-NTU method while simplified "black box" heat exchangers that use a simple energy balance for state point calculations are used in lieu of more detailed component models where data is available. The lead-cooled fast reactor is assumed to be a black box heat exchanger because of the constant heat input and state points on the sCO_2 inlet and outlet are provided. The molten salt loop for the CSP is modeled with necessary components including hot and cold TES, receiver, pumps and counter-flow heat exchangers.

Turbines and Compressors

Turbines and compressors are modeled for each cycle using constant isentropic efficiency values which are summarized in Table 3.1. Turbines take the high pressure sCO_2 and expand it through a series of blades allowing a production of energy, while compressors input mechanical energy to increase the pressure of the sCO_2. The turbines and compressors are assumed to be at steady state, exchange no heat with the surroundings, and have single inlet and outlet streams. Using this estimate, along with a known low and high side pressures, temperature and enthalpy outlets of the turbine and compressor are calculated [43].

Black Box and Counter-Flow Heat Exchangers

Black box heat exchangers are simplified heat exchangers which have no approach temperature or pinch point and are modeled as a perfect heat transfer into or out of the cycle. These heat exchangers use an energy balance with mass flow inlet energy, heat input or

output, and mass flow outlet energy. The energy balance equation used for all black box heat exchangers is Equation (3.1).

$$\dot{m} \cdot h_{in} + \dot{Q}_{HX} = \dot{m} \cdot h_{out}, \tag{3.1}$$

In this equation the energy input to the system is on the left hand side with $\dot{m}$ multiplied by h_{in} being energy from the mass flow while $\dot{Q}_{HX}$ is heat transfer directly into, positive, or out of, negative, the flow from an outside source. The right hand side of the equation is heat leaving the black box heat exchanger with $\dot{m}$ and enthalpy of h_{out}. Black box energy balances are used in three situations, the receiver, LFR heat exchanger, and pre-cooler heat exchanger. These heat exchangers are not exhaustively modeled because the state points on the inlet and outlet are defined by design parameters.

Counter-flow heat exchangers are modeled with two fluids flowing in opposite directions exchanging heat from the hot side to the cold side. The smallest temperature difference of the hot and cold flows on either the low or high end of the heat exchanger is defined as the approach temperature of the counter-flow heat exchanger and a calculation is performed to identify whether the hot end of cold end is limiting. A diagram showing a simplified counter-flow heat exchanger is illustrated in Figure 3.1.

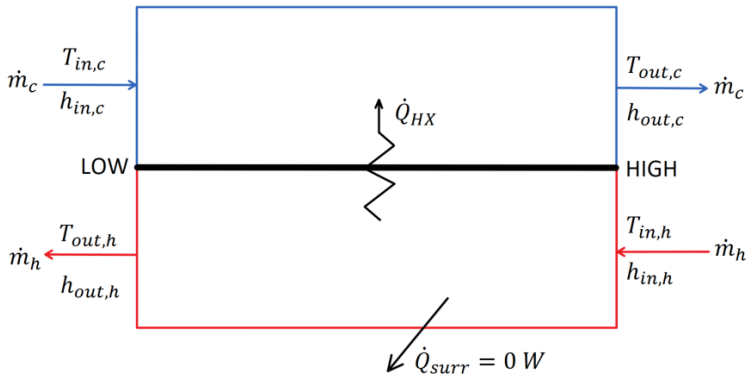

Figure 3.1: Simplified counter-flow heat exchanger diagram.

Additional assumptions of the counter-flow heat exchanger model are: no heat loss to the surroundings, no pressure drops across the heat exchangers, and no fouling resistances.

In Figure 3.1 the subscript 'out' denotes where the streams are leaving, 'in' denotes the entering streams, 'c' and 'h' signify cold and hot streams respectively, $\dot{Q}_{HX}$ is the total heat transfer from the hot to cold stream, and $\dot{Q}_{surr}$ is the heat transfer to the surroundings.

Counter-flow heat exchanger calculations require two known state points, fluid properties, mass flow rate of hot and cold side, and a specified approach temperature. In the modeled cases, the approach temperature is set to value of 10 °C, based off prior model development of sCO_2 Brayton cycle heat exchangers [44]. The fluid libraries referenced are built into Engineering Equation Solver (EES). for Carbon Dioxide and Salt (60% $NaNO_3$ 40% KNO_3) [45, 46].

To analyze the counter-flow heat exchanger a side is chosen, usually the high side, to start the calculations. The approach temperature is initially subtracted from the hot stream on the high temperature side to find the missing cold temperature according to Equation (3.2).

$$T_{out,c} = T_{in,h} - \delta_T, \tag{3.2}$$

where $T_{out,c}$ is the cold stream outlet temperature and $T_{in,h}$ is the hot stream inlet temperature. Knowing the two state points allows for the enthalpy out to be found using correlations from the fluid property libraries. This enthalpy then allows for the heat transfer of the heat exchanger to be found with Equation (3.3).

$$\dot{Q}_{HX} = \dot{m}_c(h_{out,c} - h_{in,c}), \tag{3.3}$$

where $\dot{Q}_{HX}$ is the total heat transfer rate from the hot stream to the cold stream, $\dot{m}_c$ is the mass flow rate of the cold stream, $h_{out,c}$ is the enthalpy at the outlet of the cold side, and $h_{in,c}$ is the inlet of the cold side. The known heat transfer of the counter-flow heat exchanger can then solve for the enthalpy out of the hot stream, $h_{out,h}$. This is accomplished with Equation (3.4).

$$h_{out,h} = h_{in,h} - \frac{\dot{Q}_{HX}}{\dot{m}_h}, \tag{3.4}$$

Knowing the hot stream enthalpy out allows for all states to be set on the outlets and inlets of the counter-flow heat exchanger. The temperature difference of the low side is then checked to ensure that it is larger than the approach temperature, defined at 10°C. If the temperature difference on the low side is smaller than the approach temperature, the same computations are carried with the low side as the starting point.

Knowing the state points on all inlets and outlets of the counter-flow heat exchanger allows for the heat exchanger performance metrics to be calculated. Performance metrics include effectiveness (ε), capacitance (CR), conductance (UA), and number of transfer units (NTU) for heat exchangers. Effectiveness is the ratio of the actual heat transfer rate to the maximum heat transfer rate, a perfect heat exchanger has an effectiveness of one with no approach temperature. Assuming the approach temperature is on the high side, the maximum heat transfer rate, $\dot{Q}_{max}$ is found with the maximum enthalpy. Maximum enthalpy of the cold stream is found with correlations by setting the temperature to $T_{in,h}$ with same pressure on the cold outlet. Using the maximum enthalpy, h_{max}, the maximum heat transfer rate is calculated using Equation (3.5).

$$\dot{Q}_{max} = \dot{m}_c(h_{max} - h_{in,c}), \tag{3.5}$$

Calculating the maximum heat transfer rate allows for effectiveness to be calculated using the ratio in Equation (3.6).

$$\varepsilon = \frac{\dot{Q}_{HX}}{\dot{Q}_{max}}, \tag{3.6}$$

All of the prior equations are carried out in a built-in function within EES. EES is an iterative solver, therefore as long as there is a feasible solution, the functions can take any of the four state points around the heat exchanger and converge on a solution.

After the effectiveness is solved for, capacitance ratio is necessary. The capacitance ratio is defined as the average minimum capacitance rate, $\dot{C}_{min}$, over the average maximum capacitance rate, $\dot{C}_{max}$. Average capacitance rates for the hot and cold streams are found by multiplying the addition of the specific heat at the inlet and outlet of the stream by the mass flow and dividing by two as seen in Equation (3.7).

$$\dot{C}_{avg} = \frac{\dot{m}(c_{in} + c_{out})}{2}, \tag{3.7}$$

Where C_{avg} is the average capacitance rate across the hot or cold stream and c_{in} and c_{out} is the specific heat at the inlet and outlet respectively. Specific heat is found using library correlations, with the average capacitance rate assumed to be constant during the analysis. Once both average capacitances are calculated for the hot and cold streams, one has a larger value, $\dot{C}_{max}$, and one has a smaller value, $\dot{C}_{min}$. These maximum and minimum values are used to find the capacitance ratio, CR, in Equation (3.8).

$$CR = \frac{\dot{C}_{min}}{\dot{C}_{max}}, \tag{3.8}$$

Assuming constant average capacitance rate is suitable for most engineering purposes, especially when there is uncertainty associated with other design parameters [47]. To justify the assumption of constant average capacitance rate, two graphs for the LTR and HTR are plotted. To ensure that there is no internal pinch point, the temperatures of the hot and cold streams as a function of dimensionless length in the LTR and HTR are shown in Figure 3.2 b,d respectively. Additionally, to confirm approximate linearity of specific heats at differential steps throughout the counter-flow heat exchanger, the specific heat as a function of dimensionless length of the hot and cold streams in the LTR and HTR are plotted in Figure 3.2 a,c respectively.

The calculations used to discretize the counter-flow heat exchangers into a sub-heat exchanger model, shown in Figure 3.2, are from Dyreby 2014 thesis [48]. Figure 3.2 is

constructed using the most extreme temperature values experienced by the recuperators—the cold inlet and hot outlet are the lowest and highest modeled temperature values, respectively. As demonstrated, the capacitance ratio determines the approach temperature instead of any possible internal pinch point within the recuperator. All pinch points recorded are on the high-temperature end.

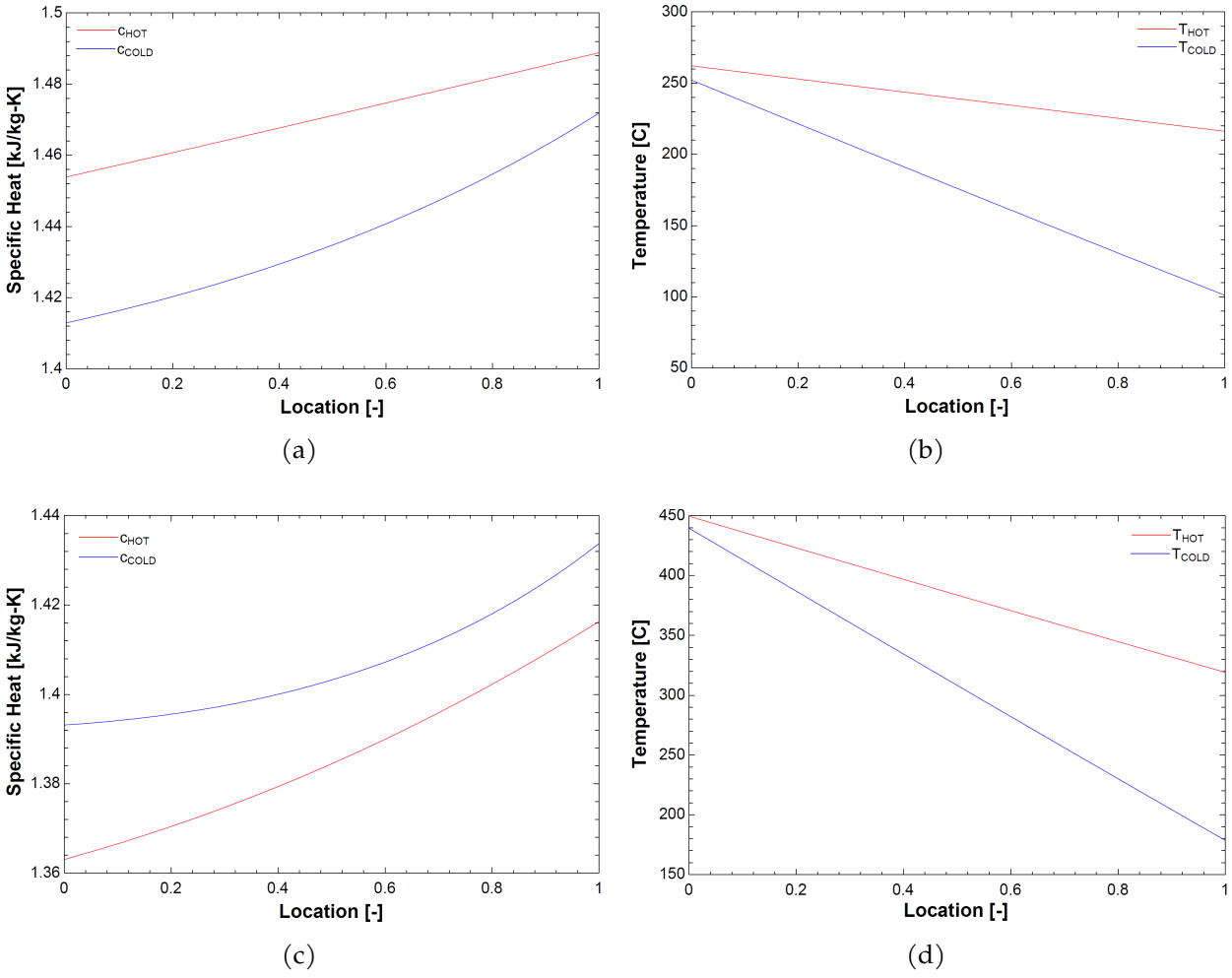

Figure 3.2: Specific heats and temperatures of hot and cold streams as a function of dimensionless location for the low temperature recuperator and high temperature recuperator. (**a**) Specific heat as a function of location for LTR; (**b**) Temperature as a function of location for LTR; (**c**) Specific heat as a function of location for HTR; (**d**) Temperature as a function of location for HTR.

Lead-Cooled Fast Reactor

Lead-cooled fast reactors use energy from a controlled nuclear reaction to heat molten lead. This lead is used to cool the core and transfer heat into the sCO_2 Brayton power cycle [49, 50]. The lead-cooled fast reactor is assumed to be a black box heat transfer and is labeled in the cycle models LFR HX. The inlet, outlet and heat transfer rates are provided by our industry partner, Westinghouse, making the black box simplification viable. The energy balance for the black box assumption can be seen in Equation (3.9).

$$\dot{m} \cdot h_{inlet} + \dot{Q}_{LFRHX} = \dot{m} \cdot h_{outlet}, \tag{3.9}$$

Where the left hand side, $\dot{m}$, h_{inlet}, and $\dot{Q}_{LFRHX}$, is the energy into the flow and the right hand side, $\dot{m}$ and h_{outlet}, is the energy brought out from the flow of sCO_2. The amount of energy transferred into the cycle, $\dot{Q}_{LFRHX}$, is set at 950 MW, and outlet temperature of the sCO_2 from the LFR HX is set at a value of 595 °C. The outlet temperature of the LFR is specified because of high temperature material limits on the LFR lead side. The low temperature side is allowed to vary over a range of values with some considerations. The lead flow velocity is limited by the erosion of the fuel, the slower the lead flow velocity reduces fuel erosion and therefore leads to a more desirable compact design. At constant lead velocity (and hence mass flow rate), reducing sCO_2 inlet temperature allows for a higher coolant temperature increase in the LFR core and hence a higher thermal power output LFR sCO_2 inlet temperature has a lower bound of 340 °C before the lead begins to freeze, which is operationally unacceptable. When the inlet temperature of sCO_2 is increased the temperature difference across the LFR is decreased leading to an increase in power conversion cycle thermodynamic efficiency but a reduction in LFR power below 950 MW. There is a compromise between high LFR efficiency and LFR power, therefore a temperature of 400 °C for the sCO_2 inlet temperature is the optimal value provided by Westinghouse.

Concentrating Solar Power Cycle

The CSP salt cycle modeled in this chaper is composed of hot and cold thermal energy storage, pumps, receiver, sCO_2-to-salt counter-flow heat exchanger (C2S), and CSP counter-flow heat exchanger (CSP HX). The diagram for this CSP salt loop is seen in Figure 3.3.

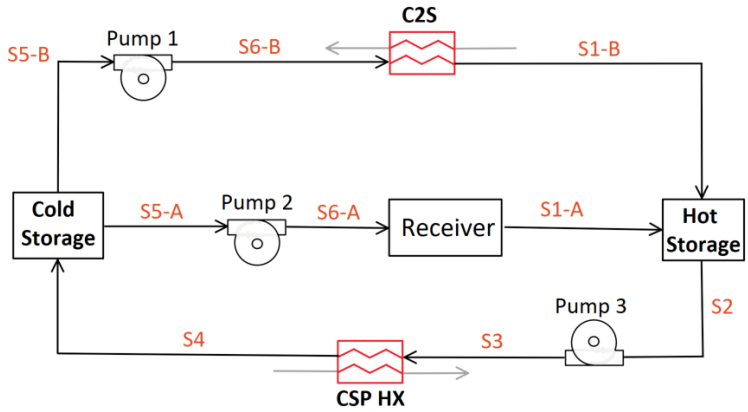

Figure 3.3: Diagram for CSP cycle with cold and hot thermal energy storage, pumps, and CSP black box heat input

The CSP salt cycle uses 60% sodium nitrate, $NaNO_3$, and 40% potassium nitrate, KNO_3, 'solar salt' as the heat transfer fluid. Solar salt stored in the hot TES can be dispatched on demand through the CSP HX when grid demand increases and held when grid demand is low. Current CSP salt cycles heat solar salt with receivers and store it in hot TES tanks at temperatures around 565 °C. Future CSP salt cycles are hypothesized to have bulk hot TES temperatures of up to 720 °C, but here the hot TES temperature is set at 560 °C for all modeled cycles [12] as this has been commercially proven. The cold TES temperature takes on three different values according to cycle configuration capabilities: 390 °C, 410 °C, and 440 °C. In addition to the lower hot TES temperature, current CSP salt cycles lack a secondary option for charging the hot TES [51]. The studied CSP salt cycle has two TES charging options: a receiver, which generates heat from a heliostat field, and C2S heat exchanger, which draws excess heat from the sCO_2 Brayton cycle. While the hot TES is charging, the receiver and LFR are storing heat for later use when grid demand increases. The hot TES storage is not dispensing salt for use in the CSP cycle while charging.

The C2S heat exchanger is active in the 'charging' cycle operating modes, when the focus is on heat storage for later use. Pump 1 is actively moving solar salt from cold TES to hot TES through the C2S heat exchanger extracting heat from the sCO_2 Brayton cycle. Additionally, while the focus is on heat storage, and the heliostat field is inputting heat, pump 2 is actively transporting solar salt through the receiver to be stored in the hot TES.

'Non-charging' cycle operating modes are characterized by operations wherein the CSP salt cycle is discharging the hot TES, the C2S heat exchanger is not transferring heat, and the LFR is dispatching heat directly to generate electricity. When electrical generation is occurring and solar resource is available, the heat input in the CSP salt cycle is modelled through a black box energy balance across states S6-A and S1-A with a heat addition of 750 MW from the heliostat field. The hot TES solar salt is moved through Pump 3 and transfers heat into the sCO_2 Brayton cycle through CSP HX to be converted into electricity. The cooled salt is stored in cold storage and moved through Pump 2 where the heat from the receiver is again transferred into the CSP cycle.

When grid demand for electrical power increases, a series of operating modes are activated. During the highest demand times, cycle operation focuses on maximum electrical generation. This is achieved through the C2S being turned off for direct electrical production from the LFR and the hot TES is discharging heat through the CSP HX for electrical production in the sCO_2 Brayton cycle. As grid demand diminishes, CSP HX ramps down heat extraction until no power is being dispatched through the salt and the hot TES begins charging. During this process, the LFR gradually adds a larger fraction of heat input to the TES through C2S, supplementing the heat produced by the CSP which is also used to charge the TES. This process continues until no electrical production is occurring in the cycle and all heat is stored in TES for later use.

Standardization of Cycle Modeling

In order to draw a more direct comparison, the cycles are standardized in terms of isentropic efficiencies, heat exchanger approach temperatures, pressures, heat input, and pump constants. These values are summarized in Table 3.1.

Table 3.1: Standardized constant cycle parameters with definition, variable and set value.

Parameter	**Variable**	**Design Point Value**
Efficiencies		
Main Compressor	η_{MC}	0.91 (-)
Re-Compressor	η_{RC}	0.89 (-)
Turbine	η_{T}	0.90 (-)
Pumps 1–3	η_{P}	0.90 (-)
Approach Temperatures		
Low Temperature Recuperator	δ_{LTR}	10 (°C)
High Temperature Recuperator	δ_{HTR}	10 (°C)
CSP Heat Exchanger	δ_{CSPHX}	10 (°C)
Pressures		
Pressure Ratio	PR	3.27 (-)
High Side Pressure	P_{2A}	288 (Bar)
Heat Into System		
LFR Heat Transfer	$\dot{Q}_{LFRHX}$	950 (MW)
CSP Heat Transfer	$\dot{Q}_{CSP}$	750 (MW)
Temperature		
Main Compressor Inlet	T_{1A}	40 (°C)
LFR sCO_2 High Temperature	T_5,T_{2C},T_{6A},T_{5C}	595 (°C)
Pumps		
Pressure Rise Across Pump	Δ_P	37.26 (Bar)
Pump Low Side Pressure	P_{S5-B}	30 (Bar)

The values displayed in Table 3.1 are representative of CSP and the Westinghouse LFR. In Table 3.1, variable names require further explanation. The high side pressure with the variable label P_{2A}, is the constant pressure outlet on the compressors and inlet to the turbines. In all models the value is set by the outlet of the main compressor and held constant with the assumption that there is no pressure drop across heat exchangers. In addition to this pressure, temperatures are also set. The inlet temperature of the main

compressor, T_{1A}, is set to a value of 40 °C in all models. The temperature of the sCO_2 on the outlet of the LFR HX has different variable names, T_5, T_{2C}, T_{6A}, and T_{5C}, according to the associated cycle configuration diagram.

In addition to standardized parameters, all cycles have identical recompression sides. The recompression side contains a precooler (PC), low temperature recuperator (LTR), and two compressors; main compressor (MC) and recompressor (RC). The modeled cycles are summarized in Table 3.2.

Table 3.2: Summary of all modeled non-charging and charging cycles with descriptions.

Cycle Label	**Description**
Non-Charging	
C-LFR-ON	Two-cycle configuration with LFR as heat source.
C-CSP-ON	Two-cycle configuration with CSP as heat source.
C-1HTR1T-ON	CSP and LFR heat sources in parallel with one turbine.
C-2HTR3T-ON	CSP and LFR loops each with dedicated HTR and turbine.
Charging	
C-LFR-PRE	Turbine is prior to the C2S.
C-LFR-POST	Turbine is after the C2S.
C-LFR-PAR	Turbine is parallel to the C2S.
C-LFR-CIRC	Circulator bridges the LFR and C2S.

Non-Charging Cycle Configurations

Various cycles are modeled to test their advantages and disadvantages. These cycle models fall into two categories: non-charging and charging. The non-charging category is used to determine the configuration of the cycle with a focus on electricity generation. This includes the number and location of turbines, recuperators, and heat input to the system by the CSP and LFR. To quantify the effectiveness of the non-charging configurations, a cycle efficiency, η_{cycle}, is defined in Equation (3.10).

$$\eta_{cycle} = \frac{\dot{W}_T - \dot{W}_{MC} - \dot{W}_{RC}}{\dot{Q}_{LFRHX} + \dot{Q}_{CSPHX}}, \tag{3.10}$$

The numerator in Equation (3.10) is the alternator power, or the power produced from the turbines, $\dot{W}_T$, minus the required power of the compressors, $\dot{W}_{MC}$ and $\dot{W}_{RC}$. The denominator is the total power input into the system from the LFR HX, $\dot{Q}_{LFRHX}$, and CSP HX, $\dot{Q}_{CSPHX}$.

Two-Cycle Configuration: C-LFR-ON and C-CSP-ON

The two-cycle configuration that is tested has independent sCO_2 loops that share a common CSP salt cycle. This cycle has two sCO_2 Brayton Cycles: C-LFR-ON and C-CSP-ON. Configuration of components for these two cycles is identical with the exception of heat inputs. C-LFR-ON has heat provided from a LFR while C-CSP-ON has heat provided from the CSP. These two cycles individually operate when the focus of plant operation is primarily electricity generation.

The cycle that is using the LFR heat input in the two-cycle configuration is labeled as C-LFR-ON and the cycle diagram is illustrated in Figure 3.4. Two separate sensitivity studies on the LFR inlet temperature are completed for C-LFR-ON. The constrained study is calculated by setting the LFR inlet temperature to the design value of 400 °C, which is a requirement of the LFR primary circuit to maximize power output within material limits. In addition to the constrained studies, unconstrained studies are required to test the penalties that LFR inlet temperature has on efficiency. The unconstrained study is performed by gradually increasing the mass flow to the main compressor through a parametric study while maximizing cycle efficiency. In Figure 3.4, the location of the C2S heat exchanger while charging falls between state point 5 and 6 in any of the studied charging configurations: parallel, pre, circulator, or post.

The cycle that is using the CSP heat input in the two-cycle configuration is labeled C-CSP-ON and the cycle diagram is shown in Figure 3.5.

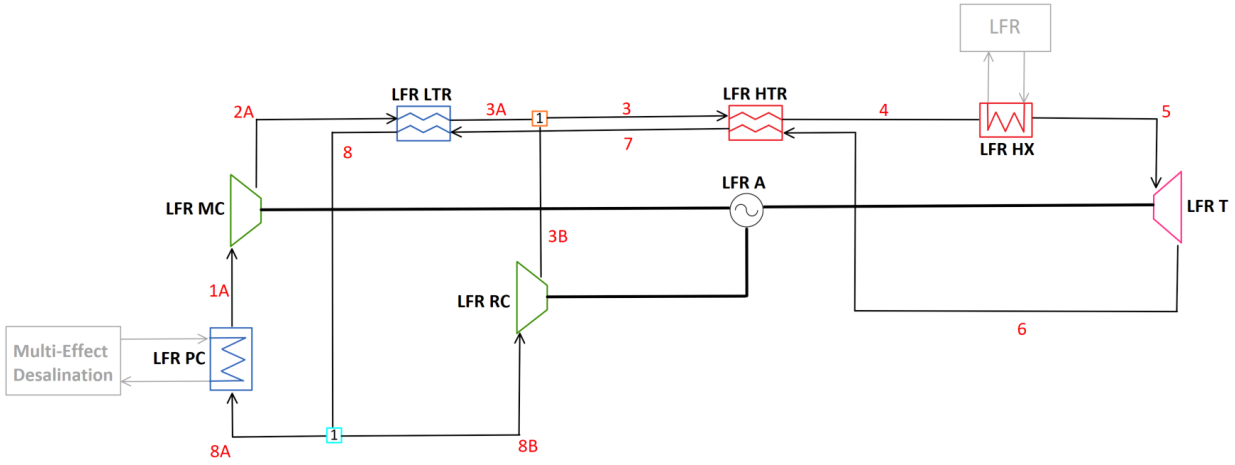

Figure 3.4: Diagram for C-LFR-ON with focus on electricity generation

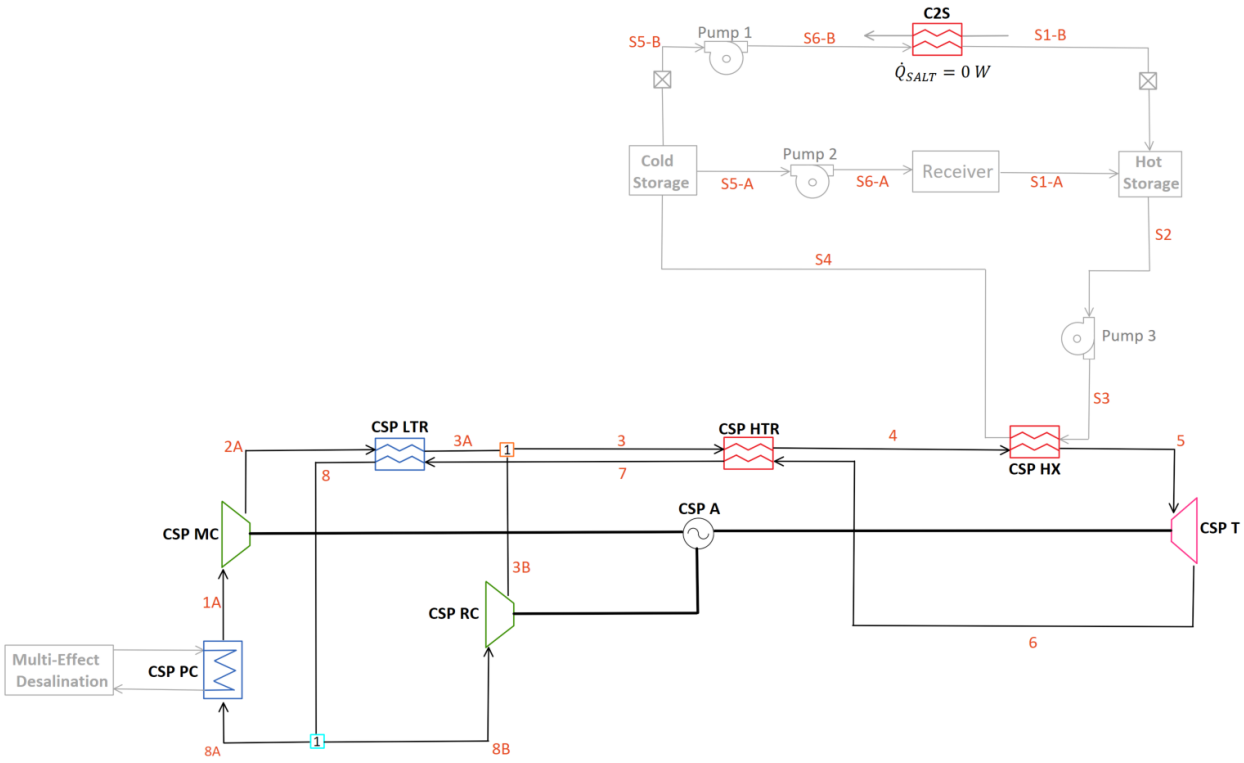

Figure 3.5: Diagram for C-CSP-ON with focus on electricity generation

Due to the individual operation while the cycles are generating electricity, C-CSP-ON is not directly impacted by the LFR low end temperatures. Instead, a sensitivity study is done on the temperature of the cold TES. Two temperatures are tested, 390 °C and 440 °C, to observe the impact of cold TES temperature on cycle efficiency. Efficiencies need to be combined to draw a comparison of the two-cycle configurations to the single cycle configurations; C-1HTR1T-ON and C-2HTR3T-ON. Equation (3.11) is used to calculate this combined two-cycle efficiency.

$$\eta_{combined} = \frac{\dot{W}_{A,\text{C-LFR-ON}} + \dot{W}_{A,\text{C-CSP-ON}}}{\dot{Q}_{LFRHX} + \dot{Q}_{CSPHX}}, \tag{3.11}$$

Equation (3.11) is the ratio of total alternator (net) power of C-LFR-ON, $\dot{W}_{A,\text{C-LFR-ON}}$, and C-CSP-ON, $\dot{W}_{A,\text{C-CSP-ON}}$, to the total heat input into the cycles from the LFR and CSP heat exchangers, $\dot{Q}_{LFRHX} + \dot{Q}_{CSPHX}$.

C-1HTR1T-ON

One drawback of having a two-cycle design, as seen in the C-LFR-ON and C-CSP-ON, is doubling the number of system components. Combining the two cycles into one would reduce redundancy, complexity, and cost. Heat addition from the CSP HX and LFR HX in parallel orientation is therefore studied in the C-1HTR1T-ON model. This model studies what impact mixing different temperature flows prior to the turbine has on cycle efficiency. The diagram for this cycle is illustrated in Figure 3.6.

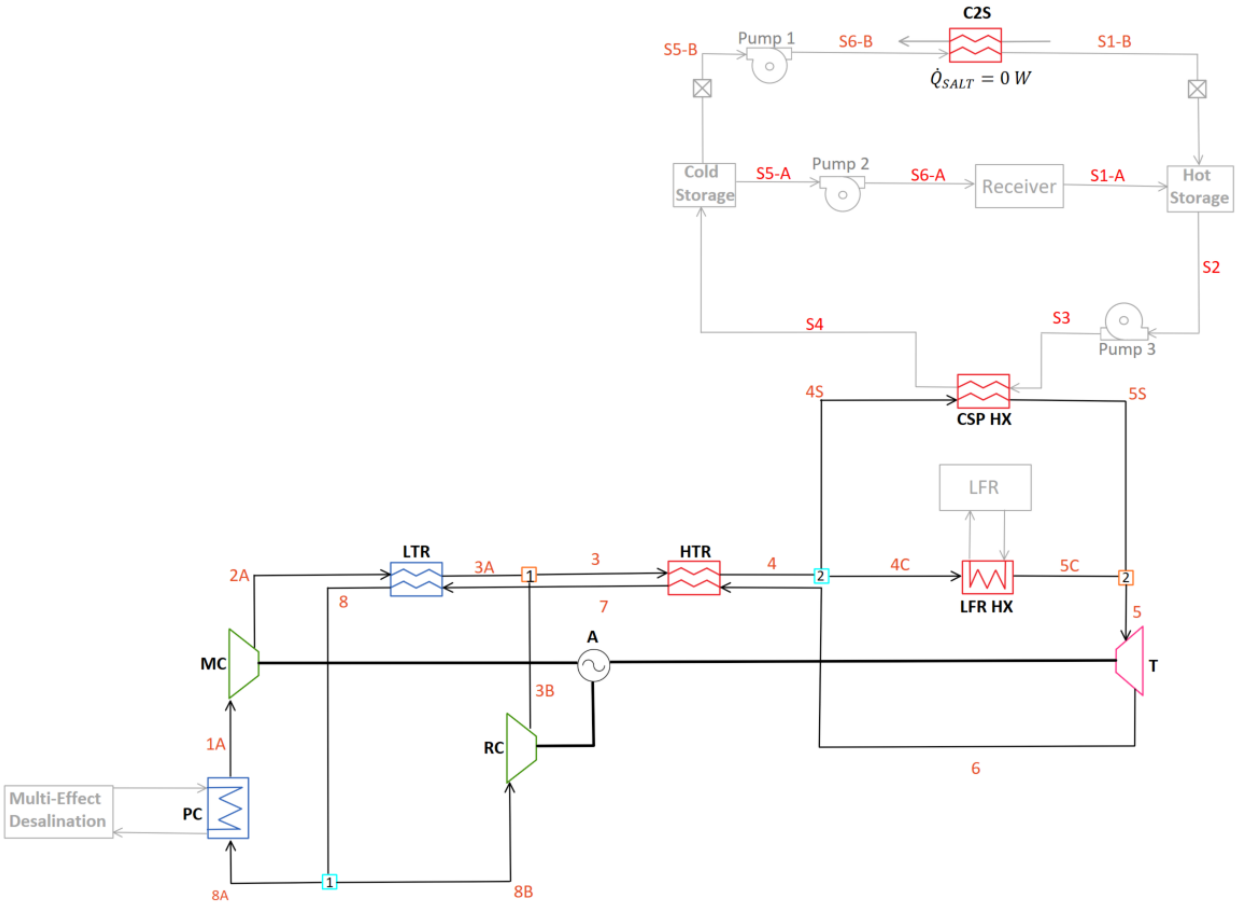

Figure 3.6: Diagram for C-1HTR1T-ON with focus on electricity generation

The C2S is located around the turbine and LFR at state points 5 to 6 depending on the charging cycle configuration: pre, parallel, post or circulator. In the C-1HTR1T-ON cycle, the LFR HX and CSP HX have identical inlet temperatures due to splitting the flow prior to their parallel orientation. Therefore, three sensitivity studies are done on the model. The initial two studies have the low LFR temperature constrained to the value of 400 °C with varied cold CSP TES temperature and maximized cycle efficiency. To achieve a maximum cycle efficiency, the split fraction amount of flow to the main compressor, y_1, is parametrically studied. Two cold TES temperatures are tested with constrained LFR low temperature of 400 °C:

- 410 °C: Lowest cold TES temperature possible due to the sCO_2 cold inlet constrained from the LFR to 400 °C and the addition of 10 °C approach temperature;

- 440 °C: Upper bound temperature on cold TES storage;
- 390 °C: Unconstrained LFR cold inlet temperature allows a lower cold TES of 390 °C to be achieved. This allows for a larger temperature drop across the CSP HX, increasing dispatchability.

C-2HTR3T-ON

The identical inlet temperatures due to the parallel configuration makes the C-1HTR1T-ON cycle configuration restricted. Another single cycle configuration is desired to allow dissimilar inlet temperatures for the CSP HX and LFR HX while additionally testing the effect that mixing flows downstream from the HTR has on cycle efficiency.

In practice, sCO_2 cycles typically have three turbines, with two of these driving the compressor and recompressor. Therefore, this configuration will not in general require additional turbines compared to the C-1HTR1T-ON configuration. Furthermore, it is anticipated that the cost of the high temperature recuperator (HTR) is likely most related to its volume, and hence having two smaller high temperature recuperators is unlikely to cost significantly more than one large one.

This cycle, C-2HTR3T-ON, can be seen in Figure 3.7 and has two high temperature recuperators and three turbines. The LFR is powering one turbine, T1, and transferring unused heat to the flow entering LFR HX through a dedicated high temperature recuperator, HTR. The cycle with heat addition from the CSP powers the other two turbines, which for modeling purposes are combined into a single turbine T2, while having a dedicated high temperature recuperator, HTR2. The two turbines displayed as T2 can be modeled as a singular turbine because their isentropic efficiencies are identical causing the inlet and outlet conditions of the turbines to be consistent with a singular turbine. Additionally, the power produced by the two turbines is proportional to mass flow rate, each receives a fraction of the mass flow rate therefore producing the same fraction of power. Summing these power fractions together yields the total power of a singular turbine in the same

position. After the high temperature recuperators, the two flows are combined and sent to the LTR hot side.

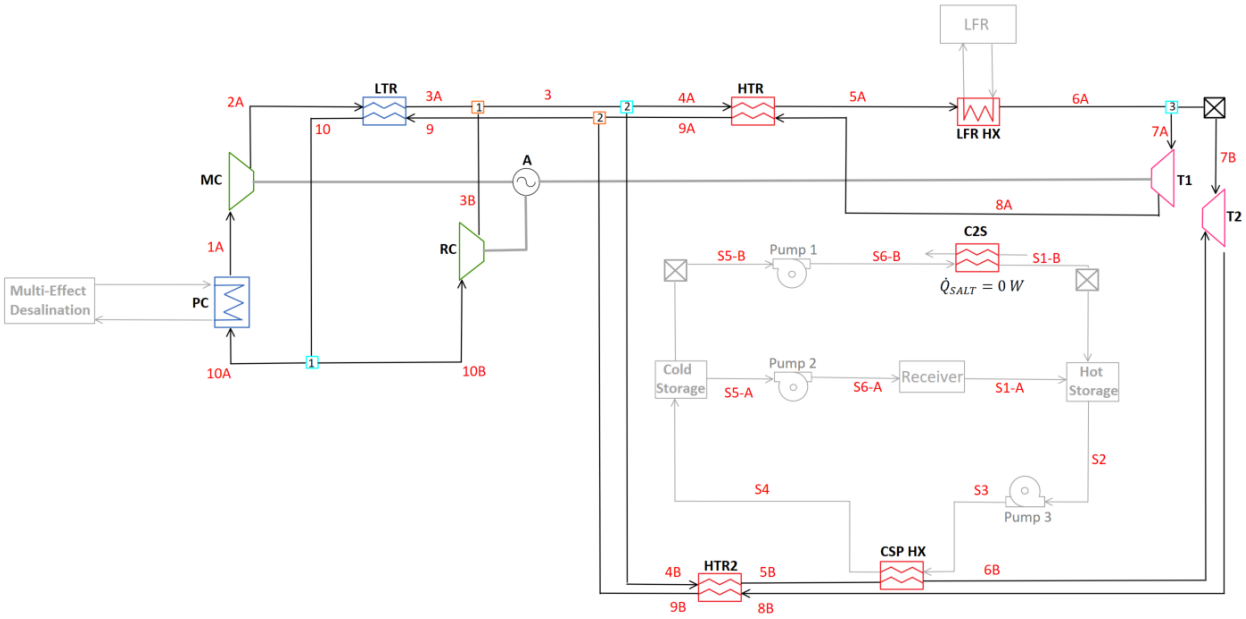

Figure 3.7: Diagram for C-2HTR3T-ON with focus on electricity generation

The C2S heat exchanger is located around the turbine and LFR at 7A to 8A depending on the charging configuration: pre, post, parallel or circulator. Three sensitivity studies are done on the C-2HTR3T-ON model — two with the LFR low temperature constrained and one without this constraint. The two constrained studies, with an LFR temperature of 400 °, have varied cold CSP TES temperature with the lowest temperature of 390 °C and highest temperature of 440 °C. The unconstrained low LFR inlet study is calculated at a cold CSP TES temperature of 390 °C.

Thermal Energy Storage Charging Techniques

Charging cycle configurations accommodate energy storage modes of operation. These configurations examine the location of LFR heat extraction via C2S. To maximize the available heat for extraction, alternator net power is set to zero, therefore requiring the turbine power to balance with the compressors' demand. Despite the components being non-ideal

and consuming power, the recompression cycle continues to operate, ensuring that there is mass flow to transfer heat from the Brayton cycle to C2S. The excess energy from the LFR is thermally stored in the TES for later use when grid demand increases. Comparison of the heat extraction point in the cycle, C2S, is accomplished by implementing C2S in different locations around the turbine in the C-LFR-ON non-charging cycle configuration; C-LFR-PRE has the turbine prior to C2S, C-LFR-POST has the turbine after C2S, C-LFR-PAR has the turbine in parallel to C2S, and C-LFR-CIRC uses a circulating loop instead of in-flow implementation. C-LFR-ON is the configuration used for these studies because during charging operation, flow through the CSP HX is deactivated, effectively making all non-charging cycles take the identical form of C-LFR-ON. To quantify the effectiveness of TES charging techniques, Equation (3.12) defines the heat storage efficiency, $\eta_{heatstorage}$.

$$\eta_{heatstorage} = \frac{\dot{Q}_{C2S}}{\dot{Q}_{LFRHX} + \dot{Q}_{CSPHX}}, \tag{3.12}$$

In the heat storage efficiency equation, $\dot{Q}_{C2S}$ is the amount of heat transferred through C2S, and the addition of $\dot{Q}_{LFRHX}$ and $\dot{Q}_{CSPHX}$ is the total amount of heat input into the system from the LFR HX and CSP HX.

C-LFR-PRE

The high temperature sCO_2 leaving the LFR HX flows through the LFR turbine converting thermal energy to usable work. The outlet temperature of the LFR turbine is at a temperature suitable to charge the hot TES, therefore the flow is passed through C2S exchanging heat to the cold solar salt. The diagram outlining this process is C-LFR-PRE in Figure 3.8.

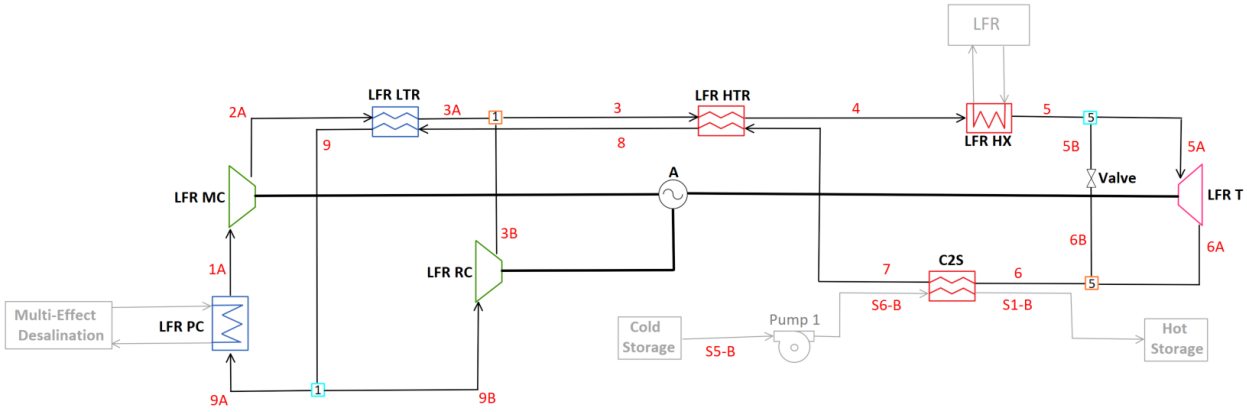

Figure 3.8: Diagram for C-LFR-PRE thermal energy storage charging orientation.

A problem arises with this salt charging configuration. The temperature out of the turbine is not high enough to charge the hot CSP TES to the required value of 560 °C when the turbine power is balanced with the compressor demand. To raise the temperature, some of the high temperature flow before the turbine is redirected through a valve and combined after the turbine. Limiting the flow through the turbine reduces the turbine power and compressor power because of the balancing requirement. Due to the reduction in available compressor power, the LFR RC is effectively bypassed, and a large portion of usable heat is expelled in the LFR PC before the LFR MC. The thermal storage efficiency reduces as a result of the large amount of heat rejected in the LFR PC.

C-LFR-POST

Moving the heat extraction prior to the turbine is analyzed in C-LFR-POST. This diagram is seen in Figure 3.9.

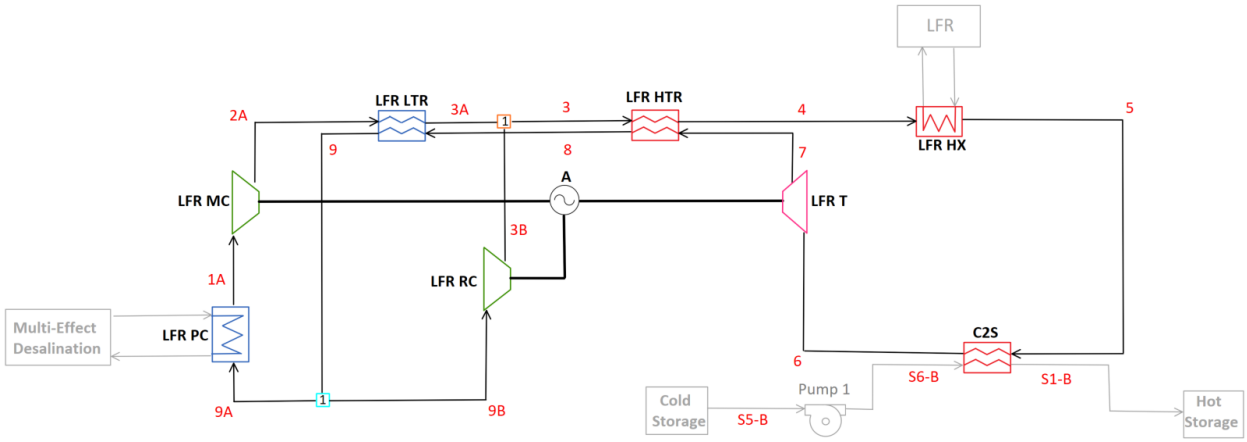

Figure 3.9: Diagram for C-LFR-POST thermal energy storage charging orientation.

This TES charging cycle extracts heat before the turbine and therefore has a large negative effect on the amount of work that the turbine is producing. The turbine power offsets the requirements of both compressors, requiring the turbine inlet temperature to be high. The amount of energy that is extracted before the turbine is small and therefore the heat storage efficiency is fractional compared to other charging techniques. There is no quantitative study done on this case because, due to the efficiency losses, it is non-viable.

C-LFR-PAR

The requirements of the turbine and CSP hot TES can be satisfied by splitting the flow before the turbine. The flow through the salt heat exchanger in this cycle is therefore separate from the turbine. After the salt heat exchanger, a valve is needed to reduce the pressure, this TES charging cycle is C-LFR-PAR shown in Figure 3.10.

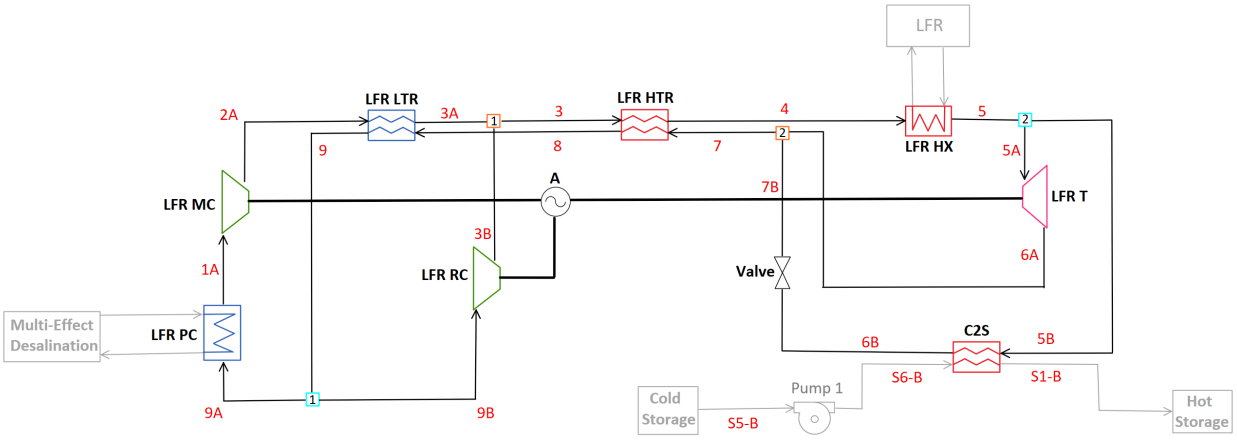

Figure 3.10: Diagram for C-LFR-PAR thermal energy storage charging orientation.

A sensitivity study with varying cold CSP TES temperature is carried out to determine the impact on heat storage efficiency. The study considers two temperature values of 390 °C and 440 °C.

C-LFR-CIRC

The full diagram for C-LFR-CIRC is shown in Figure 3.11.

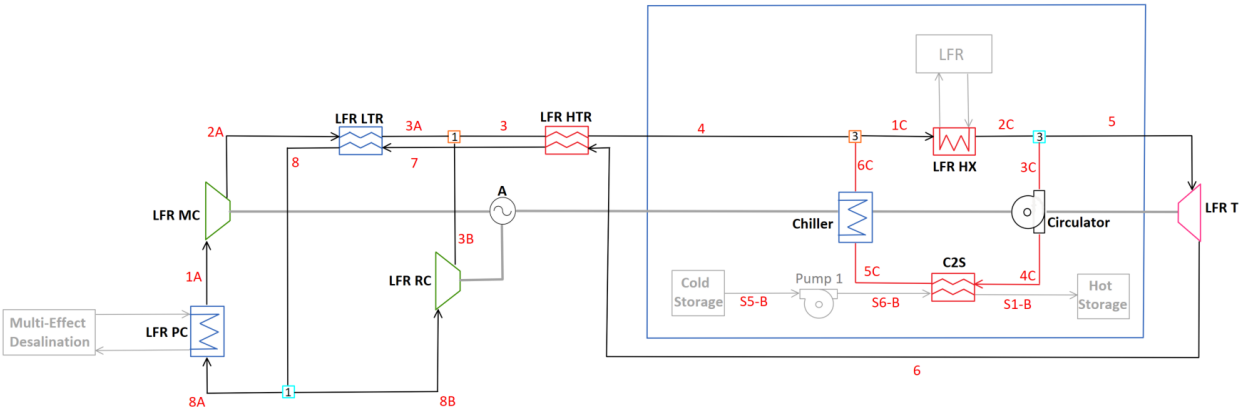

Figure 3.11: Full diagram for C-LFR-CIRC thermal energy storage charging orientation.

The charging subsection of this diagram is composed of a circulation cycle that has heat inputted through the LFR heat exchanger. A separated circulation cycle has a loop which avoids the losses associated with compressor and turbine, therefore achieving higher heat

storage efficiency than possible with full cycle operation. This subsection is encircled in blue and can be seen in Figure 3.12.

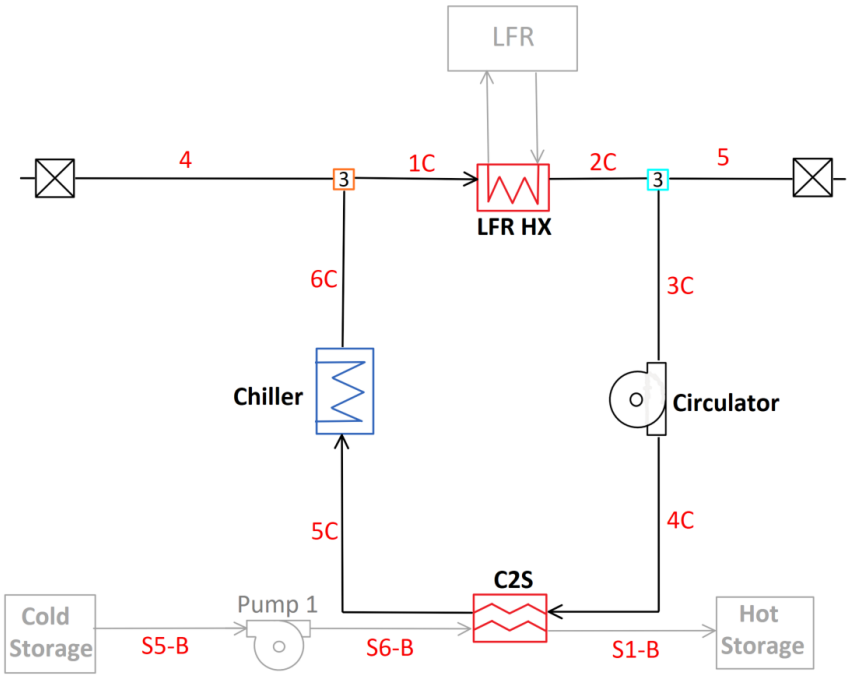

Figure 3.12: Diagram for C-LFR-CIRC sub-cycle thermal energy storage charging orientation.

The flow continues through a circulator which is assumed to have negligible pressure rise (i.e. there is assumed to be negligible pressure drop in this case). A heat exchanger, C2S, extracts heat from the flow, storing the thermal energy in the hot TES for later use. Excess heat that is not extracted is then dumped into a reservoir through the chiller to bring the temperature of the flow down to LFR cool side operating temperature of 400 °C. Three different cold TES temperatures; 390 °C, 410 °C, and 440 °C, are compared in a sensitivity study.

3.3 Results and Discussion

For all cycle configurations presented, with constrained or unconstrained LFR low temperature inlet and varied cold TES temperature, cycle and heat storage efficiencies are maximized using parametric studies on flow splitter fractions. All calculations were carried out using EES, with the results obtained using standardized values found in Table 3.2 for a more direct comparison between cycles. Presentation and discussion of the results is fulfilled in the following section.

Non-Charging Cycle Configurations

The three non-charging cycle models have a focus on producing the highest positive alternator power to heat input, or cycle efficiency. The two-cycle configuration, composed of C-LFR-ON and C-CSP-ON, has independent recompression cycles with dedicated compressors, turbine, recuperators, and pre-cooler for the LFR and CSP. C-1HTR1T-ON, with the heat additions in parallel, and C-2HTR3T, with dedicated HTR for both heat additions, are cycles which incorporate the CSP and LFR in the same cycle. The results from studies done on these cycles are displayed in Table 3.3.

The calculated values reported in Table 3.3 are component power, mass flow fractions, and counter-flow heat exchanger specifications. Columns labeled with 'C' headers have the LFR sCO_2 low inlet temperature constrained to 400 °C while those labeled with 'U' are unconstrained and calculated based off of a parametric study on the MC mass flow fraction. Values listed in the Cold TES Temperature row are set to values of 390 °C, 410 °C, or 440 °C to study the effects that cold TES temperature has on cycle efficiency and to accommodate certain characteristics of cycle configurations. Cycles that do not contain the listed component omit the associated values.

Table 3.3: Calculated system parameters for non-charging cycle configurations with constrained (C) and unconstrained (U) lead-cooled fast reactor low-end temperature.

		C-LFR-ON		C-CSP-ON		C-1HTR1T-ON			C-2HTR3T-ON		
Definition	**Variable**	U	C	N/A	N/A	U	C	C	U	C	C
Cycle Efficiency (%)	η_{cycle}	47.08	45.28	45.58	45.93	44.9	44.22	44.22	46.10	44.34	44.35
LFR Inlet Temperature (°C)	$T_{4,4C,5A}$	415.1	400	·	·	380	400	400	415.2	400	400
Cold TES Temperature (°C)	T_{CS}	·	·	390	440	390	410	440	390	390	440
Alternator Power (MW)	$\dot{W}_A$	447.3	430.2	336.3	340.6	763.9	752.3	752.6	783.7	753.7	754
PC Heat Transfer (MW)	$\dot{Q}_{PC}$	502.7	519.8	415.0	420.2	937.4	949.2	949.3	917.6	947.6	947.9
MC Power (MW)	$\dot{W}_{MC}$	115	118.9	94.94	96.13	214.5	194.8	194.8	209.9	216.8	216.9
RC Power (MW)	$\dot{W}_{RC}$	116.6	77.3	96.41	97.71	217.4	285.7	285.7	213.5	140.8	140.8
T1 Power (MW)	$\dot{W}_{T1}$	678.9	626.4	527.7	534.5	1196	1233	1233	679.3	626.3	626.3
T2 Power (MW)	$\dot{W}_{T2}$	·	·	·	·	·	·	·	527.8	485	485.4
MC Mass Flow Fraction (-)	y_1	0.7	0.7844	0.6996	0.6994	0.7	0.6333	0.6333	0.6993	0.7846	0.7846
LFR Mass Flow Fraction (-)	y_2	·	·	·	·	0.4485	0.4928	0.4929	0.5478	0.5486	0.5484
LTR UA Value (MW/ °C)	UA_{LTR}	54.68	22.84	45.0	45.53	102	91.63	91.64	134.4	41.56	41.57
LTR Capacitance Ratio (-)	CR_{LTR}	0.9867	0.8473	0.9858	0.9854	0.9867	0.9066	0.9066	0.9853	0.847	0.847
LTR Heat Transfer Rate (MW)	$\dot{Q}_{LTR}$	656.8	366.5	543.7	551.4	549.2	614.9	615.1	1204	667.1	667.3
LTR Effectiveness (-)	ε_{LTR}	0.92	0.8742	0.9201	0.9202	0.92	0.9485	0.9485	0.9414	0.8741	0.8741
HTR UA Value (MW/ °C)	UA_{HTR}	48.29	42.71	34.29	34.72	78.22	82.3	82.34	48.32	42.69	42.69
HTR Capacitance Ratio (-)	CR_{HTR}	0.8657	0.8143	0.8593	0.8594	0.8595	0.8754	0.8755	0.8661	0.8142	0.8142
HTR Heat Transfer Rate (MW)	$\dot{Q}_{HTR}$	998.1	1161	659.9	667.7	679.2	742.6	743	545.7	636.8	636.6
HTR Effectiveness (-)	ε_{HTR}	0.9544	0.9627	0.9436	0.9436	0.9445	0.9441	0.9441	0.9542	0.9627	0.9627
HTR2 UA Value (MW/ °C)	UA_{HTR2}	·	·	·	·	·	·	·	34.29	31.61	31.63
HTR2 Capacitance Ratio (-)	CR_{HTR2}	·	·	·	·	·	·	·	0.8594	0.8074	0.8074
HTR2 Heat Transfer Rate (MW)	$\dot{Q}_{HTR2}$	·	·	·	·	·	·	·	298.1	363.4	363.8
HTR2 Effectiveness (-)	ε_{HTR2}	·	·	·	·	·	·	·	0.9436	0.9561	0.9561
CSPHX UA Value (MW/ °C)	UA_{CSPHX}	·	·	70.75	26.92	33.72	73.4	35.05	70.88	44.92	23.13
CSPHX Capacitance Ratio (-)	CR_{CSPHX}	·	·	0.9924	0.701	0.8104	0.9957	0.8034	0.9926	0.9138	0.6454
CSPHX Heat Transfer Rate (MW)	$\dot{Q}_{CSPHX}$	·	·	751.3	760.8	751.3	751.5	751.9	751.3	751.3	751.9
CSPHX Effectiveness (-)	ε_{CSPHX}	·	·	0.945	0.945	0.945	0.9381	0.9374	0.9450	0.9493	0.9493

Two-Cycle Configuration: C-LFR-ON and C-CSP-ON

The two-cycle configuration has the CSP and LFR operating in separate recompression cycles when the focus is on electrical generation, therefore these two cycles are analyzed individually. C-LFR-ON has the highest efficiency during unconstrained operation with a gain of 1.8 percentage points. The unconstrained case allows for smaller temperature gradient across the LFR, an increase in recuperator effectiveness, and an increase in recuperator capacitance ratio, all of which reduce sources of irreversibility in the cycle [43]. Increasing the LFR sCO_2 inlet temperature above the design value of 400 °C is favorable from a cycle efficiency perspective, but reduces the LFR thermal power. This is because the LFR mass flow rate and outlet temperature are constrained by materials properties (to limit creep, corrosion and erosion), so a lower inlet temperature implies a lower thermal power. In principle, dropping the LFR inlet temperature further, to as low as 340 °C (beyond which

lead freezing becomes limiting), would further increase thermal power at the expense of cycle efficiency, so a trade-off is needed. When unconstrained, the sCO_2 inlet temperature to the LFR increases by 15.1 °C to a value of 415.1 °C, increasing LFR efficiency but demanding a larger, more idealized, LFR heat exchanger.

C-CSP-ON is not affected by constrained or unconstrained LFR sCO_2 inlet temperature because C2S is turned off and therefore the two cycles are not tethered during non-charging configuration. Two individual studies are conducted on the C-CSP-ON cycle cold TES temperature, one with a lower design value of 390 °C and another with a higher value of 440 °C. A cold TES temperature of 410 °C is excluded since it can be presumed to have an efficiency intermediate to the 390 °C and 440 °C calculated values. Cold TES temperature is found to have a negligible effect on cycle efficiency between the two studied cases, with the 440 °C case gaining 0.35 percentage points. The component that has the largest change in values is the CSP HX with a large drop in capacitance ratio and UA value, therefore the lower temperature of 390 °C for cold TES temperature is ideal increasing the performances of the heat exchanger.

Combining the two-cycle efficiencies using Equation (3.11) gives a more direct comparison to the single cycle configurations; C-1HTR1T and C-2HTR3T. Two combined efficiencies are calculated for the two-cycle configuration combination. The first has the highest efficiency, combining the unconstrained C-LFR-ON LFR low temperature and C-CSP-ON 440 °C cold TES cases. This combined efficiency yields a value of 46.1% (which is almost identical to the efficiency achieved by C-2HTR3T-ON shown in Table 3.3). The second combined configuration has a lower efficiency with favorable LFR characteristics and solar salt mass flow rate. This combination has the constrained C-LFR-ON LFR low temperature and C-CSP-ON 390 °C cold TES cases with a combined efficiency of 45.1%.

C-1HTR1T-ON

The single cycle configuration, C-1HTR1T-ON, has the CSP and LFR heat additions in parallel causing identical inlet conditions. Due to the 10 °C approach temperature, the identical inlet conditions lead to a lower bound of 410 °C on the cold TES temperature when the sCO_2 LFR inlet temperature is constrained to 400 °C. A supplementary 440 °C cold TES study is run to test the effects that higher temperature storage has on cycle efficiency. Raising the temperature of the cold TES from 410 °C to 440 °C has no effect on cycle efficiency but did raise the solar salt mass flow rate to accommodate for the lower temperature difference across the CSP HX hot side. Increasing the solar salt mass flow rate requires more storage for the same CSP heat input, a reduction in dispatchability, and larger pumps, increasing the cost of the system. Therefore, a lower cold TES temperature is desirable. Without the constraint on the sCO_2 LFR inlet temperature, a study is additionally conducted with cold TES temperature set to 390 °C. Of these three sensitivity studies, the cycle that yielded the highest efficiency is the unconstrained, 390 °C cold TES with an efficiency gain of 0.68 percentage points over the constrained cases. The high temperature difference between the hot and cold TES reduces the mass flow rate of solar salt and subsequent cost of system components. The sCO_2 LFR inlet temperature for the 390 °C cold TES study is 380 °C, which increases the performance of the LFR heat exchanger as well as allowing for a higher core power.

C-2HTR3T-ON

C-2HTR3T-ON has dedicated recuperators and turbines for the LFR and CSP, allowing for independent inlet temperatures. Three studies are conducted on this cycle with two being constrained and one unconstrained sCO_2 LFR inlet conditions. The constrained studies have cold TES temperatures of 390 °C and 440 °C, both of which have negligible efficiency differences. Similarly to the studies done on C-1HTR1T-ON, the 440 °C cold TES temperature case has a larger mass flow rate of solar salt and therefore increases

component cost. The 390 °C unconstrained study has the highest efficiency with a value of 46.10%, 1.76 percentage points more than the constrained cases. Additionally, the sCO_2 LFR inlet temperature is 415.2 °C, 15.2 °C more than constrained cases, causing heat exchanger parameters to be less than ideal but increasing LFR efficiency.

Thermal Energy Storage Charging Techniques

When the focus of the cycles is thermal storage for later use, the LFR charges the hot TES through the C2S heat exchanger. Studies done on the charging techniques have constrained sCO_2 LFR inlet temperatures to 400 °C with set values of cold TES temperature of 390 °C, 410 °C, or 440 °C. The two charging techniques which run the full recompression cycle are C-LFR-PRE, with the turbine before the heat extraction, and C-LFR-PAR, with heat extraction in parallel to the turbine. The third charging technique, C-LFR-CIRC, has a dedicated circulation loop and additional chiller and circulator pump to avoid losses associated with the compressors and turbines. The results are presented in Table 3.4.

Table 3.4: Calculated system parameters for charging cycle configurations. All cases were evaluated with constrained (C) lead-cooled fast reactor low-end temperature.

		C-LFR-PRE	**C-LFR-PAR**		**C-LFR-CIRC**		
Definition	**Variable**	*C*	*C*	*C*	*C*	*C*	*C*
Cold TES Temperature (°C)	T_{CS}	390	390	440	390	410	440
LFR Inlet Temperature (°C)	$T_{4,1C}$	400	400	400	400	400	400
Heat Storage Efficiency (%)	$\eta_{heatstorage}$	34.53	45.30	45.30	99.92	89.66	74.29
Alternator Power (MW)	$\dot{W}_A$	0	0	0	·	·	·
PC Heat Transfer (MW)	$\dot{Q}_{PC}$	622	519.6	519.6	·	·	·
MC Power (MW)	$\dot{W}_{MC}$	142.3	118.9	118.9	·	·	·
RC Power (MW)	$\dot{W}_{RC}$	21.89	77.28	77.28	·	·	·
Turbine Power (MW)	$\dot{W}_T$	164.2	196.2	196.2	·	·	·
Chiller Heat Transfer (MW)	$\dot{Q}_{chill}$	·	·	·	0.7245	98.25	244.2
MC Mass Flow Fraction (-)	y_1	0.9389	0.7844	0.7844	·	·	·
C2S Mass Flow Fraction (-)	y_2	·	0.6867	0.6867	·	·	·
Valve Mass Flow Fraction (-)	y_5	0.7378	·	·	·	·	·
LTR UA Value (MW/ °C)	UA_{LTR}	6.99	22.83	22.83	·	·	·
LTR Capacitance Ratio (-)	CR_{LTR}	0.6754	0.8473	0.8743	·	·	·
LTR Heat Transfer Rate (MW)	$\dot{Q}_{LTR}$	93.05	366.4	366.4	·	·	·
LTR Effectiveness (-)	ε_{LTR}	0.6384	0.8742	0.8742	·	·	·
HTR UA Value (MW/ °C)	UA_{HTR}	41.69	42.69	42.69	·	·	·
HTR Capacitance Ratio (-)	CR_{HTR}	0.7531	0.8143	0.8143	·	·	·
HTR Heat Transfer Rate (MW)	$\dot{Q}_{HTR}$	1567	1160	1160	·	·	·
HTR Effectiveness (-)	ε_{HTR}	0.9695	0.9627	0.9627	·	·	·
C2S UA Value (MW/ °C)	UA_{C2S}	9.04	8.037	14.24	48.29	43.16	35.63
C2S Capacitance Ratio (-)	CR_{C2S}	0.4735	0.7556	0.9339	0.8755	0.8599	0.8294
C2S Heat Transfer Rate (MW)	$\dot{Q}_{C2S}$	328	430.4	430.4	949.3	851.8	705.8
C2S Effectiveness (-)	ε_{C2S}	0.9368	0.8275	0.8307	0.9511	0.9459	0.9355
C2S Approach Temperature (°C)	δ_{C2S}	10	35	26.27	10	10	10

C-LFR-PRE

The TES charging technique with the turbine prior to the C2S heat exchanger, C-LFR-PRE, requires the temperature of the C2S inlet to be high enough to charge the hot TES. The hot TES is at a temperature of 560 °C, with a 10 °C approach temperature, therefore the inlet temperature to C2S is required to be at least 570 °C. In cases where the turbine outlet temperature is less than 570 °C, a isenthalpic valve bypasses flow from the high temperature turbine inlet and mixes with the low temperature turbine outlet raising the temperature prior to the C2S heat exchanger. For the C-LFR-PRE configuration to be viable, it requires a larger temperature than the set LFR HX outlet temperature of 595 °C. With this low of a LFR outlet temperature, 73.78% of the flow is redirected around the turbine to raise the temperature prior to C2S. As the temperature of the hot TES is raised above a value of

540 °C, the amount of flow around the turbine approaches 100% and balancing the turbine power to compressor power is infeasible. The temperature in the hot TES is therefore set to a lower value of 540 °C to allow for operation of this cycle. With heat storage efficiency maximized, 93.89% of the flow is sent to the main compressor, rejecting 622 MW of heat out of the cycle through the precooler. This amount of rejected heat is reflected in a heat storage efficiency of 34.53%, the lowest of all tested TES charging configurations.

C-LFR-PAR

To test the effects of splitting flow prior to the turbine, a parallel configuration C-LFR-PAR is studied. To reduce the pressure from 288 Bar to 88 Bar, an isenthalpic valve is required after heat is extracted for storage through C2S. With this configuration two different values for cold TES are studied, one with a cold TES storage of 390 °C the other with a temperature of 440 °C. A noteworthy difference for this cycle is the C2S approach temperature is not set to 10 °C. Defining the approach temperature as 10 °C causes the energy balance governing combiner 2 to be over constrained. Therefore this value is free and calculated to be 35 °C for the 390 °C case and 26.27 °C for the 440 °C case. Both of these different temperature cold TES studies do not change the cycle parameters because, as seen in C-1HTR1T-ON and C-2HTR3T-ON, the solar salt mass flow rate adjusts to accommodate for the temperature difference. The higher cold TES temperature of 440 °C causes the mass flow rate in the CSP to increase by approximately 650 kg/s. Increasing the mass flow rate has a higher demand on system components but in this situation it allows for the salt to be charged at a higher rate, increasing the storage capabilities. Both cycles have a heat storage efficiency of 45.30%.

C-LFR-CIRC

C-LFR-CIRC is a thermal energy storage charging technique which does not suffer from significant losses associated with turbines, compressors, and heat exchangers. The separate recirculation cycle is modeled extracting heat directly from the LFR, passes the high

temperature mass flow through a circulator, exchanges the heat into the hot TES through C2S, then removes heat in a chiller to bring the temperature of the flow down to the inlet temperature of the LFR, ideally 400 °C. This is the most adoptable TES charging technique with a wide range of possible TES charging temperatures while transferring a majority of the heat from the LFR into the hot TES. Multiple temperatures for the cold TES are studied; 390 °C, 410 °C, and 440 °C. Of these three temperatures, the highest efficiency is a cold TES temperature of 390 ° with a heat storage efficiency of 100% (not accounting for pressure drop losses, which will be small). The heat storage efficiency reduces as the temperature of the cold TES is increased; the 410 °C case has an efficiency of 90% while the 440 °C case has an efficiency of 74%. This reduction in efficiency is due to the inlet temperature condition on the LFR, the higher the temperature of the cold TES the higher the temperature of the C2S outlet and therefore more heat is being extracted through the chiller to bring the flow temperature down to the LFR inlet temperature.

There is an interaction between the temperatures selected here and the non-charging cycle configuration. For C-LFR-CIRC, the highest efficiencies are achieved when the cold TES temperature is 10 °C less than the inlet to the LFR, this is due to the approach temperature on the C2S heat exchanger. If the sCO_2 LFR inlet temperature is constrained to 400 °C, then the desired cold TES temperature is 390 °C to allow for the approach temperature. If the cold TES is at a higher temperature, then the chiller is needed. This then implies that the sCO_2 inlet temperature in the salt-to-sCO_2 heat exchanger is 380 °C. From the results of the previous section, this is clearly achievable for the C-2HTR3T-ON configuration and the separate cycle configuration, but for the C-1HTR1T-ON configuration the LFR and CSP inlet temperatures are constrained to be the same. In this case, the LFR and CSP inlet temperatures would then be 400 °C, implying a cold TES temperature of 410 °C and hence a 90% heat storage efficiency with a requirement for a chiller.

3.4 Summary

This chapter analyzed contending sCO_2 Brayton cycles containing integrated CSP and LFR heat inputs with TES capability. Modeling methodology and descriptions of cycle component design are presented and discussed with assumptions, challenges, and calculations described in detail. The sCO_2 Brayton non-charging cycle configurations focuses on electrical generation while an additional operating mode — hot TES charging by the LFR — is considered when grid demand is low. Charging mode configurations consider heat extraction at different locations around the turbine in a sCO_2 Brayton recompression cycle. Two performance parameters that are used for comparison of the cycles. Cycle efficiency is used when the cycle is producing electricity, while heat storage efficiency is used when energy is being stored for later use in the charging mode. These efficiencies are maximized for each cycle configuration using optimized flow splitter fractions, adapting to the particular temperatures of the cold TES and constrained or unconstrained sCO_2 LFR inlet. The non-charging and charging cycle configuration results are discussed with advantages and disadvantages of each configuration explained. Cycle diagrams for these configurations are provided in Appendix C.

4 SUPERCRITICAL STEAM-RANKINE CYCLE

4.1 Introduction

This chapter develops a model that examines how an integrated CSP-LFR SSRC can also incorporate TES to improve dispatchability. The SSRC contains multiple components, including: LFR heat exchanger, condenser, closed shell-and-tube feedwater heaters (FWH), open FWH, steam turbines, pumps, CSP, and TES. The FWH chain is comprised of an open FWH, four low pressure FWHs, and three high pressure FWHs. The FWHs have drains pumped backwards, cascaded from high to low pressure with the high-pressure FWH drain flowing, driven by the pressure difference, to the subsequent lower-pressure FWH. These eight FWHs gradually increase the feedwater temperature on the outlet of the condenser to meet the inlet requirements of the LFR and increase cycle thermodynamic efficiency. The cycle is comprised of three turbines that are designed with a total of eight high temperature extractions that supply heat to the FWH chain. The feedwater is circulated through the cycle by low pressure and high pressure pumps positioned after the condenser and open FWH, respectively. The TES extracts heat after the highest pressure (and temperature) turbine exhaust and inserts heat at the inlet of the intermediate pressure turbine. The LFR operates at a supercritical pressure of 330 Bar leading to certain advantages — 6% increase in average thermal efficiency with increased cycle power generation for given heat input — when compared to subcritical systems. One drawback of supercritical operation is required reheat incorporation into the cycle to increase the turbine qualities above 90% [52]. Reference operating temperatures for the LFR have been provided by an industry partner and are set as constants. The heat input from the LFR is 950 MW with an inlet and outlet temperatures of 340°C and 632°C, respectively. The heat input to the CSP is assumed to be a constant 750 MW of thermal energy from the solar receiver. The TES temperatures account for the decomposition temperature restrictions on the working fluid — solar salt (60% sodium nitrate and 40% potassium nitrate, by weight) — and LFR feedwater inlet

conditions of 340 °C. Considering the temperature restrictions of solar salt and LFR inlet conditions, the TES operates with hot tank and cold tanks at 560°C and 350°C, respectively.

The SSRC has three modes of operation which depend on whether the TES is storing energy, dispatching energy, or omitted and are conventionally labeled: 'charging', 'discharging', or 'off'. In the 'charging' mode, heat is being extracted from the highest pressure turbine exhaust through the water-to-salt heat exchanger (W2S) and stored in the hot TES tank. 'Discharging' mode has salt flowing from the hot TES tank and exchanges heat into the cycle through the salt-to-water heat exchanger (S2W). The additional mass flow is injected prior to the intermediate pressure turbine (IPT) and proportionally increases the total cycle power output. When the TES is neither charging nor discharging heat, the SSRC is operating in the 'off' mode with the LFR acting as the sole heat input into the cycle. Cycle off-design performance studies for 'charging' and 'discharging' scenarios are conducted by varying the mass flow rates of salt and steam n the W2S and S2W heat exchangers, respectively, and by computing the corresponding FWH UA values using a scaling technique described below.

The cycle component modeling methodology used in the combined solar-nuclear SSRC is first explained in the following section. Discussion includes heat exchanger model types, turbine modeling and considerations, SSRC with CSP integration, and 'charging' and 'discharging' off-design studies. The methodology is followed by power generation, cycle efficiency, and design criteria results.

4.2 Methodology

To achieve insight and a thermally accurate representation of the SSRC plus LFR and CSP technologies, a state-point model is developed in Engineering Equation Solver (EES). EES is chosen as the primary modeling software because of the integrated thermodynamic property libraries, iterative solver, and parametric study capability [48, 53, 54].

Heat Exchangers

Multiple heat exchanger models are required to capture on-design performance metrics while considering internal phase changes and dissimilar fluid types. Depending on the situation, methodologies used for heat exchanger model include sub-heat exchanger, FWH, and simple 'black box' models. The sub-heat exchanger model spatially discretizes a heat exchanger to capture more detailed behavior including local phase and capacitance rate changes. Figure 4.1 illustrates how a larger counter-flow heat exchanger is broken up into several (N) subsections with the inlet and outlet states of the internal sub-heat exchanger being determined by the neighboring sub-heat exchangers.

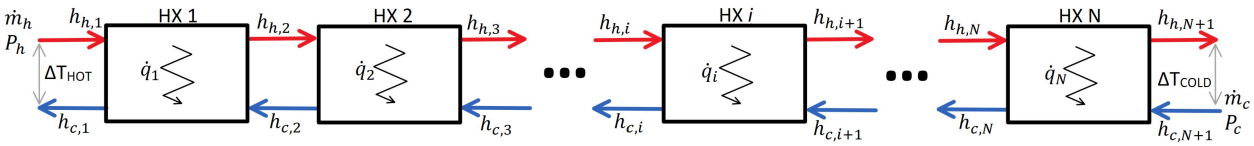

Figure 4.1: Sub-heat exchanger diagram for counter-flow heat exchanger with approach temperature defined.

A sub-heat exchanger model is developed as a procedure in EES and described below [47, 48]. The inputs to the model are the fluid names, mass flow rates ($\dot{m}_h$ and $\dot{m}_c$), inlet enthalpies ($h_{h,1}$ and $h_{c,N+1}$), and constant pressures (P_h and P_c), for the hot and cold streams. Additionally, the number of desired heat exchanger subsections, (N), and an approach temperature (ΔT), are defined. This procedure works by initially assuming an approach temperature on the 'COLD' side of the counter-flow heat exchanger setting the outlet temperature and therefore enthalpy $(h_{h,N+1})$ of the hot outlet stream. Utilizing an energy balance, the total heat transfer rate required to lower the hot stream to the approach temperature is computed and divided evenly among the N sections. The evenly distributed heat transfer rates $(\dot{q}_{1...N})$ are applied to the individual sub-heat exchangers in an energy balance function. The function repeats the energy balance calculation for each sub-heat exchanger and builds arrays for the hot and cold enthalpy inlet and outlet conditions. With the enthalpy arrays calculated, the temperature difference of the 'HOT' side is compared

to the set 'COLD' side. If the temperature difference is less than the specified approach temperature, the procedure is run again with the approach temperature starting on the 'HOT' side. This check is done to ensure that the heat exchanger is operating at the design approach temperature and not converging to solution comprised of a physically larger heat exchanger with a smaller approach temperature. The model state points are used to calculated design criteria such as conductance (UA), number of transfer units (NTU), and effectiveness (ϵ). This sub-heat exchanger model is implemented in the multi-fluid-type S2W and W2S heat exchangers, and to computes performance characteristics like UA, NTU, and temperature profiles in the desuperheating, condensing, and drain cooler regions of the FWH procedure.

Feed Water Heaters

The previously-discussed sub-heat exchanger model can calculate internal states points for counter-flow heat exchangers with multiple fluid types and phase changes, but special considerations are needed for a FWH in which the drains cascade backwards. Flow through this FWH design is driven by the pressure difference between the previous higher temperature-and-pressure turbine and the subsequent lower temperature-and-pressure FWH. This flow is known as the "drain," and it increases the number of inlets in each FWH to three: feedwater, turbine exhaust, and drain. The turbine exhaust enters the FWH as higher-temperature steam and exchanges heat with the relatively colder feedwater in the desuperheater, condenser, and drain cooler regions. In the desuperheater region, the superheated turbine exhaust transfers heat to the feedwater until the flow cools to the vapor saturation temperature. If the turbine exhaust is already at the saturated vapor condition, such as in the case of the low pressure turbine, the model disables the desuperheating region calculations. The constant-temperature flow continues through the condenser region transferring heat to the feedwater until the flow condenses to saturated liquid. The condensed turbine exhaust mixes with the drain from the adjacent higher-pressure FWH

and continues to subcool in the drain cooler region. Figure 4.2 illustrates how an individual FWH is configured in the FWH chain, connected to the previous and subsequent FWH, while being divided into the three regions, receiving three inlets, and a drain mixer.

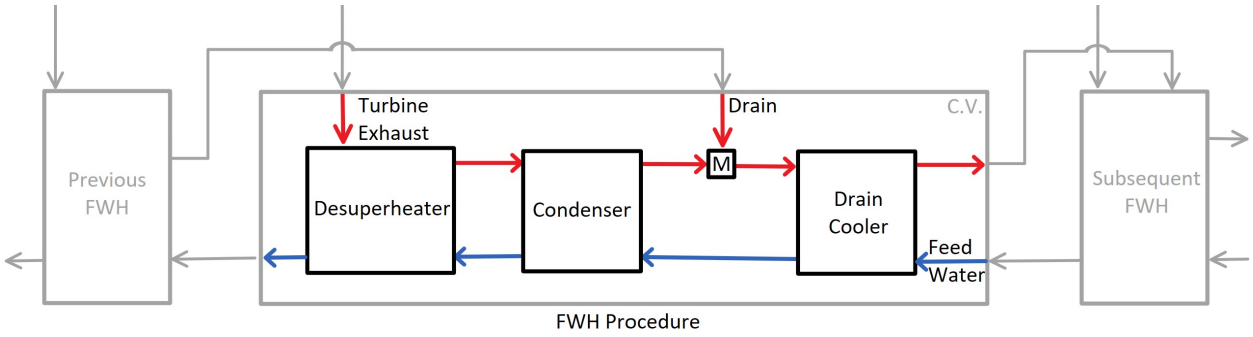

Figure 4.2: The subsections of a FWH as modeled in EES, including the desuperheater, condenser, drain cooler, and drain mixer (labeled M). Flow into the FWH includes the turbine exhaust and drain inlet on the hot side and the feedwater on the cold side.

The desuperheater, condenser, and drain cooler regions utilize the sub-heat exchanger model procedure to resolve each region's internal behavior and design point calculations. The pressure on the turbine exhaust is specified using the terminal temperature difference (TTD), defined as the difference between the saturation temperature of the turbine exhaust and the outlet of the feedwater. If the turbine exhaust pressure is set to an inadequately low value, the turbine exhaust begins condensing at a temperature which crosses over the feedwater temperature, transferring heat from cold to hot and violating the second law of thermodynamics. Specifying the TTD guarantees that the inlet turbine exhaust begins condensing at a temperature above the feedwater temperature, forcing the feedwater heater to operate at conditions which satisfy the second law of thermodynamics. The TTD is typically within a range of 0 to 3 °C and -3 to 0 °C for the low and high pressure FWHs, respectively [6].

Increasing the number of subsections inside of each heat exchanger increases computation time, model complexity, and the likeliness that EES will fail to converge to a solution. Some heat exchangers such as the LFR, CSP receiver, and the cycle condenser can be accurately modeled without high amounts of detail by using 'black box' heat exchangers.

'Black box' heat exchangers use a single energy balance with a heat transfer into or out of the cycle to calculate inlet and outlet state points. The open feedwater heater — assuming perfect mixing of fluids — acts as a 'black box' heat exchanger and is modeled using an energy balance on the drain, feedwater, and turbine exhaust inlet flows while providing feedwater to the high pressure (HP) pump.

Turbines

Power generation ($\dot{W}_{gen}$) in the SSRC is the summation of high pressure turbine (HPT), intermediate pressure turbine, and low pressure turbine (LPT) work outputs. Each of the turbines contain multiple stages and exhaust flows feeding into the individual FWHs, the exhaust pressures from the turbines are determined by the previously discussed TTD values. The HP and IP turbines are modeled isentropically, comparing the real irreversible turbine to an ideal reversible turbine by way of an isentropic efficiency parameter. The isentropic efficiencies used for all turbines in the SSRC are set to 90%. The inputs to the procedure are comprised of the fluid name, mass flow rate, inlet enthalpy and pressure, outlet pressure, and the isentropic efficiency. However, the LP turbine operates in the saturated vapor region where an excess of water droplets in steam can cause flow-accelerated corrosion on the turbine blades and a reduction in mechanical efficiency [55]. This level of moisture is typically found in flows with steam quality less than 90%. Due to the size restrictions for additional heat exchangers in the LFR, boiler reheat is not a feasible solution in this application. Other variations for reheat such as moisture separator reheaters are expensive and physically large, reducing their economic feasibility. Another plausible solution is moisture drying/separation by way of integrated grooves in the turbine shell and hollow blades which have been modeled and experimentally studied with up to 57% liquid separation from the steam flow [56, 57]. Direct modeling of this technology is difficult and would require computational fluid dynamics which is out of scope for this research. To simplify the moisture separation in the LP turbine stages, a fraction of the liquid (70%) is

assumed to be removed from the steam entering the next turbine stage and drained to the turbine exhaust. A LPT stage with liquid extraction can be seen in Figure 4.3.

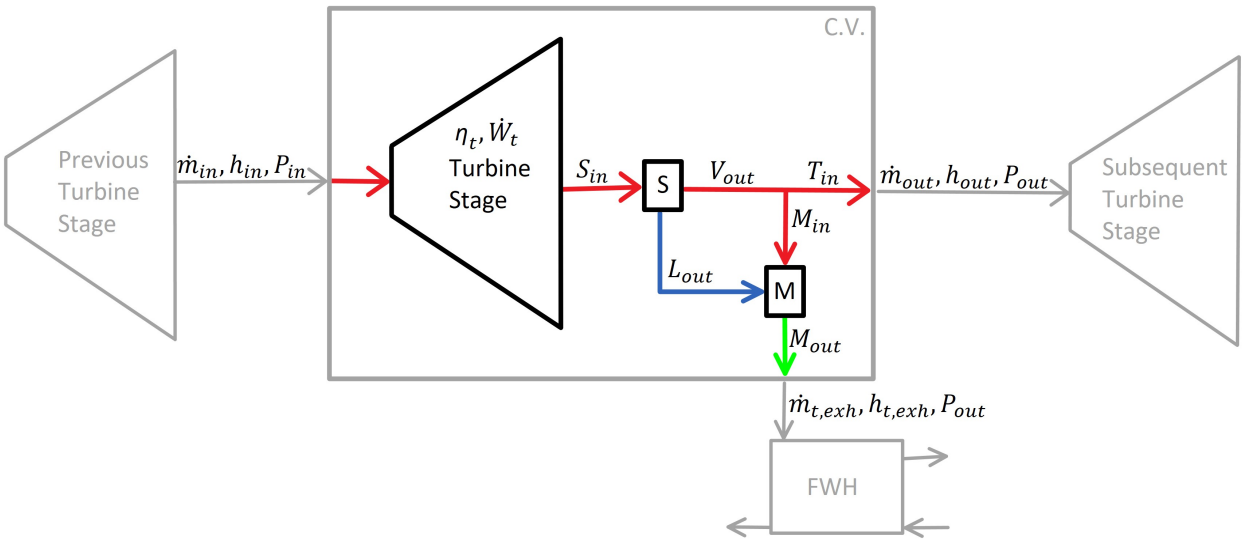

Figure 4.3: Low pressure turbine liquid extraction diagram with previous turbine (left) and subsequent turbine (right).

The methodology for modeling turbine behavior and moisture separation is as follows. The inlet conditions to the turbine ($\dot{m}_{in}$, h_{in}, and P_{in}) are calculated by the previous turbine stage procedure. The turbine stage operates with the isentropic efficiency (η_t) is specified to a constant 90%. The outlet state from the stage (S_{in}) has quality calculated, defined as the ratio of vapor mass to the total mass. The vapor mass can be determined and subtracted from the total mass to obtain the liquid mass. 70% of the liquid is removed and flows to the exhaust (L_{out}) while the higher quality steam from the moisture separation (V_{out}) flows to the subsequent turbine stage. The FWH requires a specific amount of heat input to raise the temperature of the feedwater, therefore a portion of the higher quality steam (M_{in}) is combined with the extracted liquid in the mixer (M) using a simple energy balance. The combined liquid and vapor (M_{out}) serves as the turbine exhaust to the FWH while the majority of the flow (T_{in}) serves as an input to subsequent LP turbine stages with qualities above 90%. The turbine procedure additionally outputs the turbine stage work ($\dot{W}_t$), with the total turbine power generation ($\dot{W}_{HPT}$, $\dot{W}_{IPT}$, $\dot{W}_{LPT}$) being a summation of

these internal stage works.

SSRC with Concentrating Solar Power

The heat inputs into the SSRC are comprised of the LFR and CSP. The CSP salt cycle contains multiple components: the receiver with heat input of 750 MW, two salt storage tanks for hot, 560 °C, and cold, 350 °C, TES, pumps to circulate the solar salt, and depending on the mode of operation, either charging with the W2S heat exchanger, or discharging, with the S2W heat exchanger. The CSP operates in three separate modes: 'off', 'charging' and 'discharging'. When the CSP is in 'off' mode, the LFR is the sole heat input, operating as a typical Rankine cycle with a base power output. The CSP enters 'charging' mode if grid demand and price of electricity is low, storing the energy for the 'discharging' mode that can be used during higher-demand and price periods. When the CSP is in 'charging' mode, salt is pumped from the cold tank through the W2S heat exchanger. The HP turbine provides high temperature and pressure steam to the W2S inlet, heating the cold salt to 560 °C for storage in the hot tank. When in 'discharging' mode, salt is pumped from the hot tank and exchanges heat to the SSRC until the salt temperature reaches 390 °C. The cold solar salt is then stored in the cold tank. Figure 4.4 displays a diagram of the full SSRC with accented 'charging' and 'discharging' flow paths and highlighted CSP salt cycle.

The locations of the CSP W2S and S2W heat exchangers in the SSRC are constrained by the operating temperatures of the hot and cold TES which are, in turn, specified by the decomposition of the solar salt and LFR inlet conditions, respectively. Due to the specified approach temperature of 10 °C, the W2S turbine exhaust inlet must be greater than 570 °C and the S2W feedwater inlet must be less than 340 °C. The ideal location for the CSP W2S in charging mode utilizes supercritical exhaust from the HP turbine at 236.5 Bar and 570 °C to charge the hot TES. The outlet steam from the W2S flows to FWH G in Fig. 4.4, increasing the temperature of the feedwater to the required LFR inlet temperature, 340 °C. In discharging mode, the S2W heat exchanger receives redirected flow from the

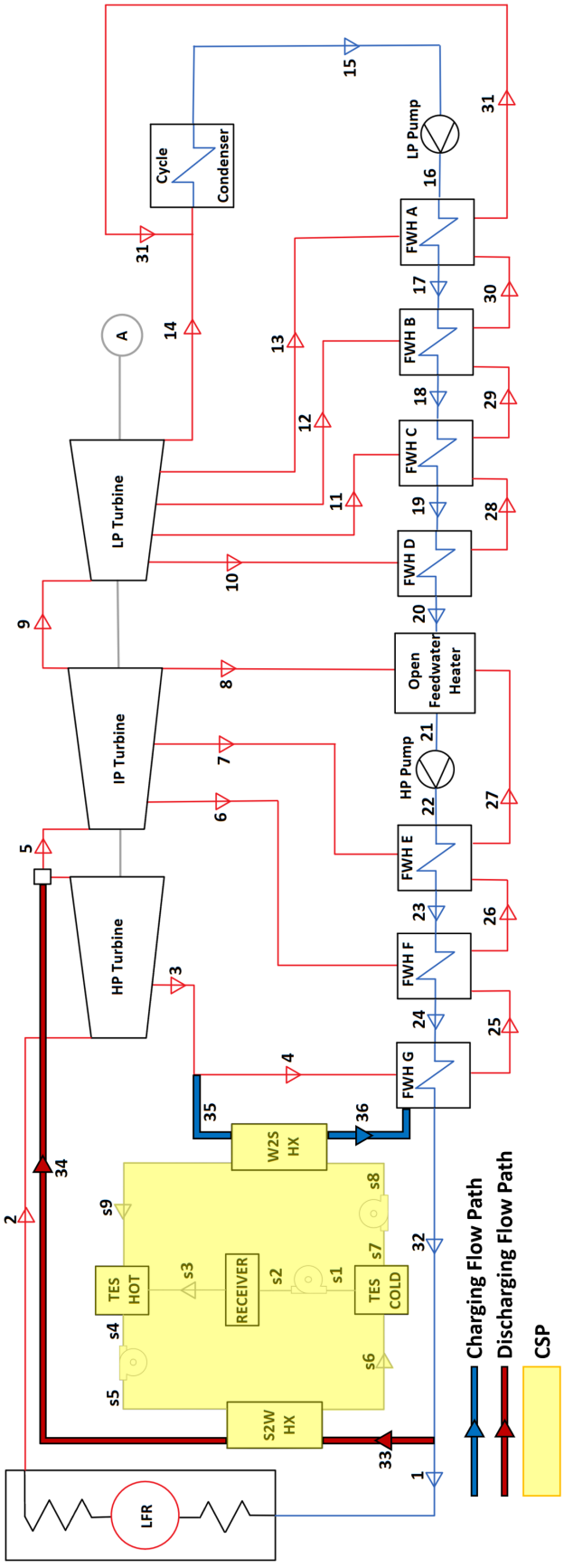

Figure 4.4: Full Complementary LFR and CSP technology SSRC diagram with highlighted 'charging' (red), 'discharging' (blue), and CSP salt cycle (yellow).

inlet to the LFR at 330 Bar and 340 °C. The S2W transfers heat to the steam flow until the temperature reaches approximately 546 °C, where the flow then reduces pressure through an isenthalpic valve matching properties and combining with the outlet of the HP turbine at state 5. The additional mass flow from the CSP in discharge mode increases the total mass flow rate through the IP and LP turbines and therefore increases the total power generation output of the cycle. The efficiency of the full cycle, η_{cycle}, is calculated using Equation (4.1).

$$\eta_{cycle} = \frac{\dot{W}_{gen} - \dot{W}_{pump}}{\dot{Q}_{input}} = \frac{\dot{W}_{HPT} + \dot{W}_{IPT} + \dot{W}_{LPT} - (\dot{W}_{HP} + \dot{W}_{LP})}{\dot{Q}_{LFR} + \dot{Q}_{S2W}} \tag{4.1}$$

Here, the numerator is the total power generated by the turbines ($\dot{W}_{gen}$) minus the pump work ($\dot{W}_{pump}$). This is equivalent to the summation of the HPT ($\dot{W}_{HPT}$), IPT ($\dot{W}_{IPT}$), and LPT ($\dot{W}_{LPT}$), power outputs minus the LP pump ($\dot{W}_{LP}$) and HP pump ($\dot{W}_{HP}$) work. The denominator is the addition of heat into the cycle, where $\dot{Q}_{input}$ is the summation of the heat input from the LFR ($\dot{Q}_{LFR}$) and S2W ($\dot{Q}_{S2W}$) heat exchanger.

Off-Design

The SSRC is adaptable to grid demand with the cycle electrical generation being dependent on mass flows of salt or steam during the 'charging' and 'discharging' modes of operation. For the 'off' mode of operation, where the SSRC does not exchange heat into or out of the TES, the LFR acts as a base load to the grid, and adjusting power generation is typically not economically advantageous. If grid demand is low, the SSRC enters 'charging' mode of operation, transferring heat from the SSRC to the hot TES while the LFR maintains full capacity operation. Heat is extracted twice from the HPT extraction — initially through the W2S HX for storage, and again through FWH G to increase the temperature of the feedwater. The higher heating potential requires an increased mass flow from the HPT turbine exhaust, therefore decreasing the available mass flow for IPT and LPT and proportionally lowering

the total generation of the cycle. Similarly to 'charging', the 'discharging' mode of operation affects the SSRC generation by introducing an additional heat source through the S2W heat exchanger. The steam flowing through the S2W heat exchanger is injected prior to the IPT, increasing mass flow and, consequently, power production of the subsequent turbines. To gain insight into a quantitative relationship between salt and steam mass flows to electrical generation, a study on the affects of fractional amounts of mass flows for 'charging' and 'discharging' is conducted.

The percentages of mass flows through the W2S for the 'charging' mode of operation are calculated from salt mass flow values, varying from 10%-100% in increments of 10%. The value for 100% 'charging' case, 190 kg/s of salt, is restricted by the maximum flow of HPT exhaust steam, the temperatures of the hot and cold storage in the TES, and the approach temperature of the W2S. 'Discharging' mode of operation has the 100% steam mass flow set at 100 kg/s and varied from 10%-100% in 10% increments with additional above-design cases of 200%, 300%, 400%, and 441% considered. The 100% steam mass flow case is set by evaluating the mass of salt entering and leaving hot TES. In this case, it is assumed that there are 5 hours of full CSP capacity in a day at a storage rate of 2340 kg/s. When the plant is dispatching salt in the 100% 'discharging' case, salt is leaving storage at a rate 525 kg/s while exchanging heat to 100 kg/s of steam flow through the S2W heat exchanger. Therefore, in 24 hours of 100% 'discharging' the total daily salt storage is equal to the total daily salt dispatched. The highest case, 441% or 2340 kg/s of salt, occurs when TES in 'discharging' mode is dispatching salt at a rate equal to the storage rate, implying there is no storage. All studied cases with their respective salt and steam mass flows for 'charging' and 'discharging' modes of operation are displayed in Table 4.1,

Table 4.1: Percentages and values of salt and steam mass flow rates for off-design calculations

Discharging	10%	20%	30%	40%	50%	60%	70%	80%	90%	100%	200%	300%	400%	441%
$\dot{m}_{salt}$ [kg/s]	53	106	159	212	265	318	371	424	477	525	1060	1589	2120	2340
$\dot{m}_{steam}$ [kg/s]	10	20	30	40	50	60	70	80	90	100	200	300	400	441
Charging	10%	20%	30%	40%	50%	60%	70%	80%	90%	100%				
$\dot{m}_{salt}$ [kg/s]	19	38	57	76	95	114	133	152	171	190				
$\dot{m}_{steam}$ [kg/s]	51.23	54.26	57.28	60.3	63.31	66.32	69.33	72.32	75.31	78.29				

When mass flow rate and other fluid properties change throughout a heat exchanger, so does the UA of the heat exchanger. UA value, or conductance, is defined as the effective heat transfer coefficient (U) times the area (A) of a specified heat exchanger to achieve the desired inlet and outlet fluid properties. While the physical size of the heat exchanger represented by the area is unchanged, the overall heat transfer coefficient calculated from thermal resistances and fluid properties varies. The SSRC, operating in 'charging' or 'discharging' modes of operation requires the UA value to scale according to calculated mass flows and fluid properties in the respective mode cases. Adjusting the UA values of the FWHs is accomplished using reference values of UA and mass flows then applying power law scaling to calculate approximate FWH UA values. The scaling factor is from A. Patnode's 2006 thesis [53] and is displayed in Equation (4.2).

$$UA_{FWH} = UA_{REF}\left[\left(\frac{\dot{m}_{c,FWH}^{0.8}\cdot\dot{m}_{h,FWH}^{0.8}}{\dot{m}_{c,REF}^{0.8}\cdot\dot{m}_{h,REF}^{0.8}}\right)\cdot\left(\frac{\dot{m}_{c,REF}^{0.8}+\dot{m}_{h,REF}^{0.8}}{\dot{m}_{c,FWH}^{0.8}+\dot{m}_{h,FWH}^{0.8}}\right)\right] \tag{4.2}$$

The reference values, signified by subscript REF, are compiled from the 100% 'discharging' mode of operation due to this mode requiring the largest physical size of the FWHs. The reference UA values (UA_{REF}) are calculated using the 100% 'discharging' case for FWHs A-F in each desuperheating, condensing, and draincooling regions. FWH G operates with supercritical fluid from the HPT, and by definition there is no phase change or distinguishable regions, therefore UA_{REF} is calculated for the entire FWH. The reference hot ($\dot{m}_{h,REF}$) and cold ($\dot{m}_{c,REF}$) mass flows through the desuperheating and condensing FWH regions are the turbine exhaust and feedwater mass flows while, when incorporated, the draincooling region hot and cold streams are the drain and feedwater mass flows respectively. For the percentage cases in 'charging' and 'discharging' modes, the UA values (UA_{FWH}) for each FWH region are calculated from values of cold and hot stream mass flows. A value of UA_{FWH} according to Equation (4.2) for that case and mode is now known and the TTD and approach temperature of the FWHs are adjusted until the FWHs UA values match the Patnode 2006 thesis scaled values.

4.3 Results

On-Design

This section presents the results of the SSRC evaluated in the 'off', 'charging' and 'discharging' modes at the 100% case, or on design, operation. The goal of this analysis is to highlight performance characteristics and to identify challenges and benefits of cycle integration as previously described. To draw comparable results, the LFR inlet and outlet conditions, isentropic efficiencies of turbines, and outlet conditions of the LP turbine are specified to constant values. Additionally, the reference 'discharging' 100% UA values are calculated with TTD values of 3 °C and approach temperatures of 5.55 °C for all FWHs and set as constants across the three modes of operation and percentage case studies. The TTD and approach temperature values are held constant in 100% 'discharging' mode since this mode represents the on-design case with the largest required mass flow rates and, therefore, UA values. The UA values for FWH A-G in 'off' and 'charging' modes are adjusted from reference UA and mass flows from the 'discharging' 100% case. The adjusted values for FWH A-G UA for the three modes of operation at 100% on-design case with the respective TTD and approach temperatures are listed in Table 4.2.

Table 4.2: FWH design criteria for all three charging modes of operation at 100% 'charging' and 'discharging' cases

Mode Dependent Criteria		**Value**		
Description	**Variable** [Units]	*off*	*charging*	*discharging*
FWH A conductance	UA_A [MW/°C]	4.696	4.449	5.453
FWH B conductance	UA_B [MW/°C]	4.478	4.245	5.206
FWH C conductance	UA_C [MW/°C]	4.292	4.067	5.008
FWH D conductance	UA_D [MW/°C]	4.095	3.882	4.877
FWH E conductance	UA_E [MW/°C]	5.457	5.402	6.369
FWH F conductance	UA_F [MW/°C]	4.580	4.600	5.350
FWH G conductance	UA_G [MW/°C]	1.827	2.528	2.130
FWH A TTD	TTD_A [°C]	2.72	2.63	3.00
FWH B TTD	TTD_B [°C]	2.72	2.62	3.00
FWH C TTD	TTD_C [°C]	2.74	2.64	3.00
FWH D TTD	TTD_D [°C]	2.90	2.79	3.00
FWH E TTD	TTD_E [°C]	2.43	2.86	3.00
FWH F TTD	TTD_F [°C]	2.28	2.84	3.00
FWH A approach temperature	ΔT_A [°C]	5.07	4.93	5.55
FWH B approach temperature	ΔT_B [°C]	5.03	4.89	5.55
FWH C approach temperature	ΔT_C [°C]	5.01	4.86	5.55
FWH D approach temperature	ΔT_D [°C]	4.99	4.86	5.55
FWH E approach temperature	ΔT_E [°C]	5.05	6.57	5.55
FWH F approach temperature	ΔT_F [°C]	5.00	6.83	5.55
FWH G approach temperature	ΔT_G [°C]	4.37	6.40	5.55

One complication and interesting result from this analysis is that FWH G does not have a TTD value because the turbine exhaust at this point is supercritical and by definition does not have a saturation pressure. The value for UA in this case is adjusted based solely on the approach temperature of FWH G. The several modes of operation correspond to what is expected for their individual use scenarios and have efficiencies, mass flow rates, and power output performance metrics calculated. The results from these calculations are displayed in Table 4.3.

Table 4.3: SSRC performance metrics for complementary LFR and CSP with three modes of operation

		Value		
Performance Metrics	**Variable** [Units]	*off*	*charging*	*discharging*
Low Pressure Turbine Work	$\dot{W}_{LPT}$ [MW]	240.3	224.7	288.2
Intermediate Pressure Turbine Work	$\dot{W}_{IPT}$ [MW]	171.5	159.7	204.9
High Pressure Turbine Work	$\dot{W}_{HPT}$ [MW]	92.63	93.66	94.67
Total Power Output	$\dot{W}_{gen}$ [MW]	508.0	477.1	587.8
Condenser Heat Rejection	$\dot{Q}_{cond}$ [MW]	462.3	432.2	555.2
Maximum Mass Flow Rate	$\dot{m}_{max}$ [kg/s]	480.1	480.1	580.1
Cycle Efficiency	η_{cycle} [%]	52.35	49.18	51.42

In 'discharging' mode, an additional 100 kg/s of steam is heated through the S2W heat exchanger and mixed prior to the IPT, generating 79.8 MW more power than the 'off' base mode of operation. A minor decrease in efficiency of 0.93% is observed when comparing the 'discharging' and 'off' modes. This decrease in efficiency is mostly attributed to the increase in feedwater mass flow rate, resulting in higher required pump power to circulate the feedwater and increased turbine exhaust mass flow rates to heat the feedwater. The 'charging' mode stores heat from the LFR for later use and therefore decreases generation by 30.9 MW with a reduction in cycle efficiency of 3.17%. This diversion in power is attributed to an increase in turbine exhaust to FWH G, reducing the available mass flow rate for generation in the IPT and LPT. Additionally, the cycle efficiency decreases because the energy stored — 60.9 MW in the hot TES during 'charging' mode — is not considered when calculating this metric. Appendix A provides a complete tabulation of mass flow rate, $\dot{m}$, temperature, T, and pressure, P, calculated by the full SSRC model with the three modes of operation: 'off', 'charging', and 'discharging'.

Off-Design

The on-design studies discussed above examine the 100% 'charging' and 'discharging' modes of operation, but fractional amounts of power are required for the SSRC power output to be flexible to grid demand. Therefore, off-design studies with 10%-100% 'charging' and 10%-441% 'discharging' mode of operation are conducted with results discussed below. Mass flows at off-design conditions for FWHs A-G are calculated, and the UA value for each FWH region is adjusted via the TTD and approach temperatures to match calculated UA from Equation (4.2). When UA adjusting is finalized, the FWH TTD and approach temperature are scaled according to their respective off-design requirements. In 'discharging' mode from 10% to 441% the quantity of steam mass flow increases from 10 kg/s to 441 kg/s and is injected prior to the IPT. A plot of UA as a function of steam mass flow through the S2W heat exchanger is displayed in Figure 4.5

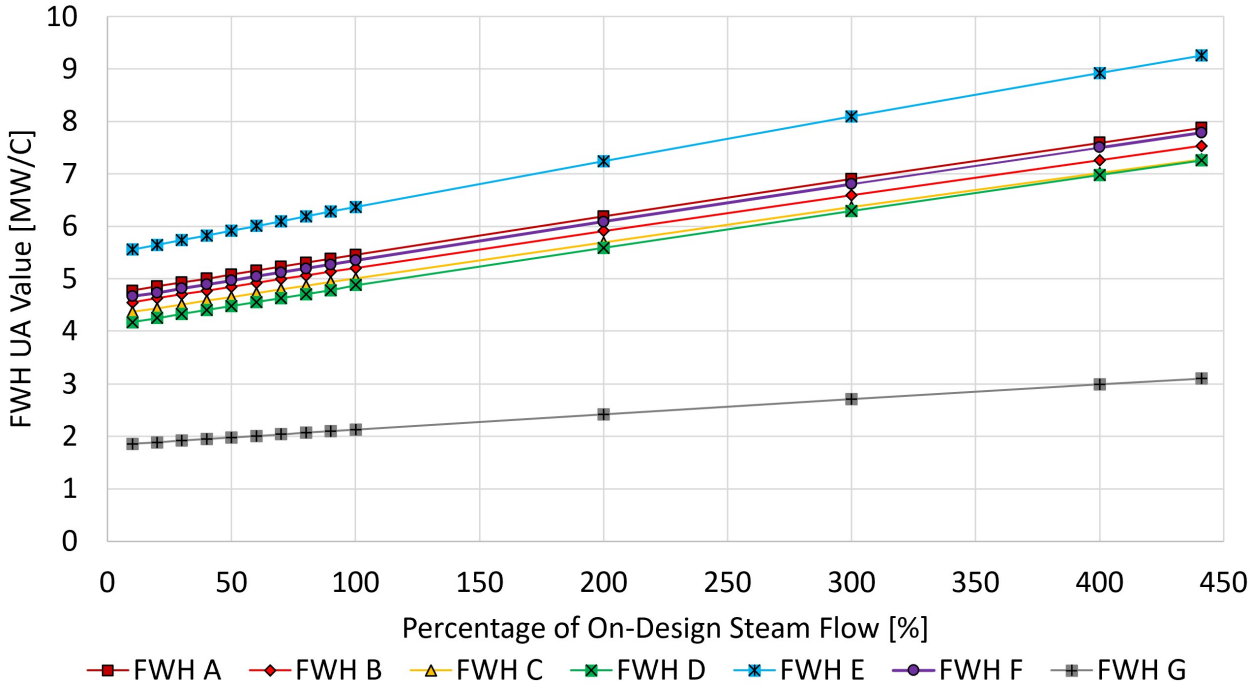

Figure 4.5: UA value for FWH A-G as a function of percentage steam mass flow through the S2W heat exchanger

As the amount of mass flow increases through the S2W heat exchanger in 'discharging' mode, the UA values of the FWHs also increase. This behavior is due to fixed-area FWHs

accommodating larger mass flow rates and requiring the flow velocity of the hot and cold streams to simultaneously increases according to conservation of mass. Increasing flow velocity increases the convective heat transfer coefficient, consequently decreasing the thermal resistance. UA is defined as inversely proportional to the total thermal resistances in a heat exchanger, therefore as the thermal resistance decreases with increased mass flow, UA also increases. The high pressure FWHs, E and F, require the largest UA values due to the relatively higher mass flows of turbine exhaust steam and feedwater when compared to the low pressure FWHs. The anomaly in this plot is FWH G, which has the lowest calculated UA value for all percentage cases while experiencing the largest quantity of HPT exhaust mass flow and, as a consequence, the highest required heat transfer rate from the HPT exhaust to the feedwater through FWH G when compared to FWHs A-F. The dissimilar behavior is due to FWH G operating with supercritical steam from the HPT exhaust which does not have a saturation point or a condensing region. The condensing region creates a point internally to the FWH where the difference between the feedwater temperature and the saturation temperature of the turbine exhaust converge to a small value, known as the pinch point. Without a phase change or pinch point, FWH G has a more balanced capacitance ratio and therefore a smaller UA value. The relationship between the heat transfer rate and steam mass flow rates through the S2W heat exchanger are plotted in Figure 4.6.

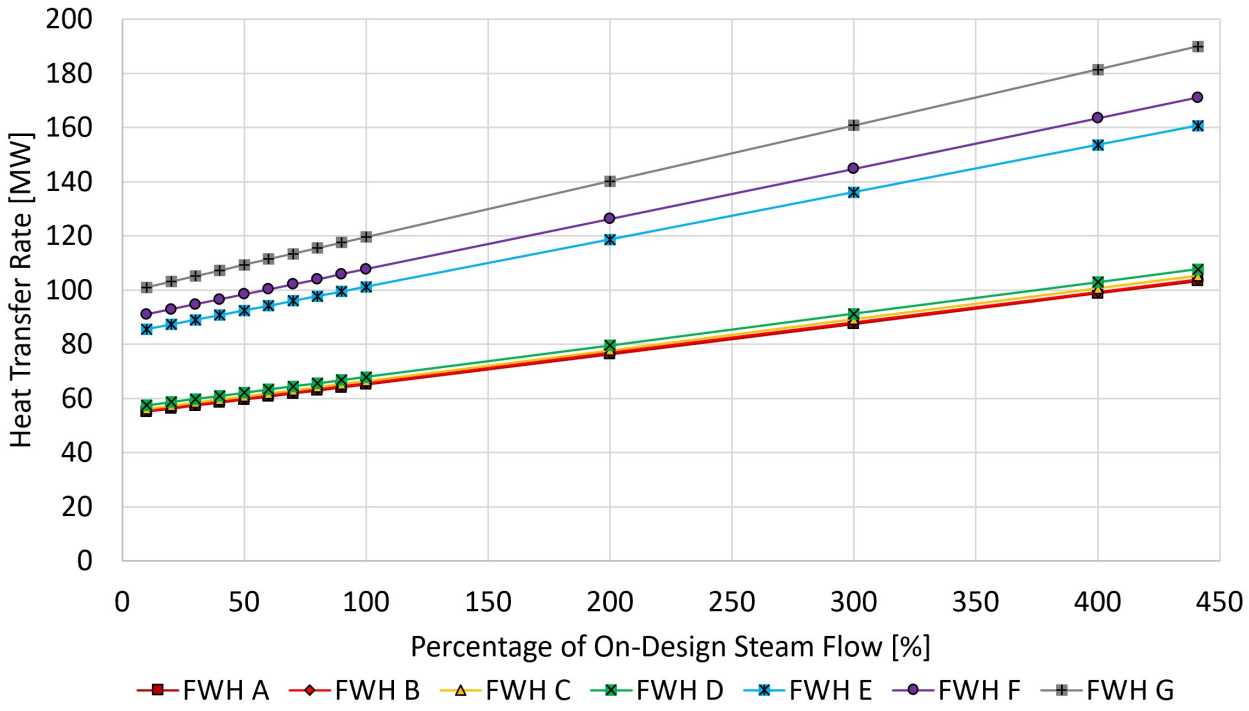

Figure 4.6: Heat transfer in FWH A-G as a function of percentage steam mass flow rate through the S2W heat exchanger

In the 10% to 441% 'discharging' mode cases, steam mass flow varies and the turbines experience changes in power output. Larger amounts of mass flow through the turbine stages proportionally increase the amount of power produced by each turbine. The additional mass flow through IPT and LPT turbines increases from 10 kg/s to 441 kg/s, increasing the turbines power outputs and, therefore, the total SSRC cycle generation. The high pressure turbine does not receive additional steam mass flow because of its placement in the SSRC prior to the IPT, and consequently the power generated by the HPT is nearly constant throughout the 'discharging' percentage case study. The power produced by all three turbines as a function of on design steam flow percentage in 'discharging' 10%-441% case studies are plotted in Figure 4.7.

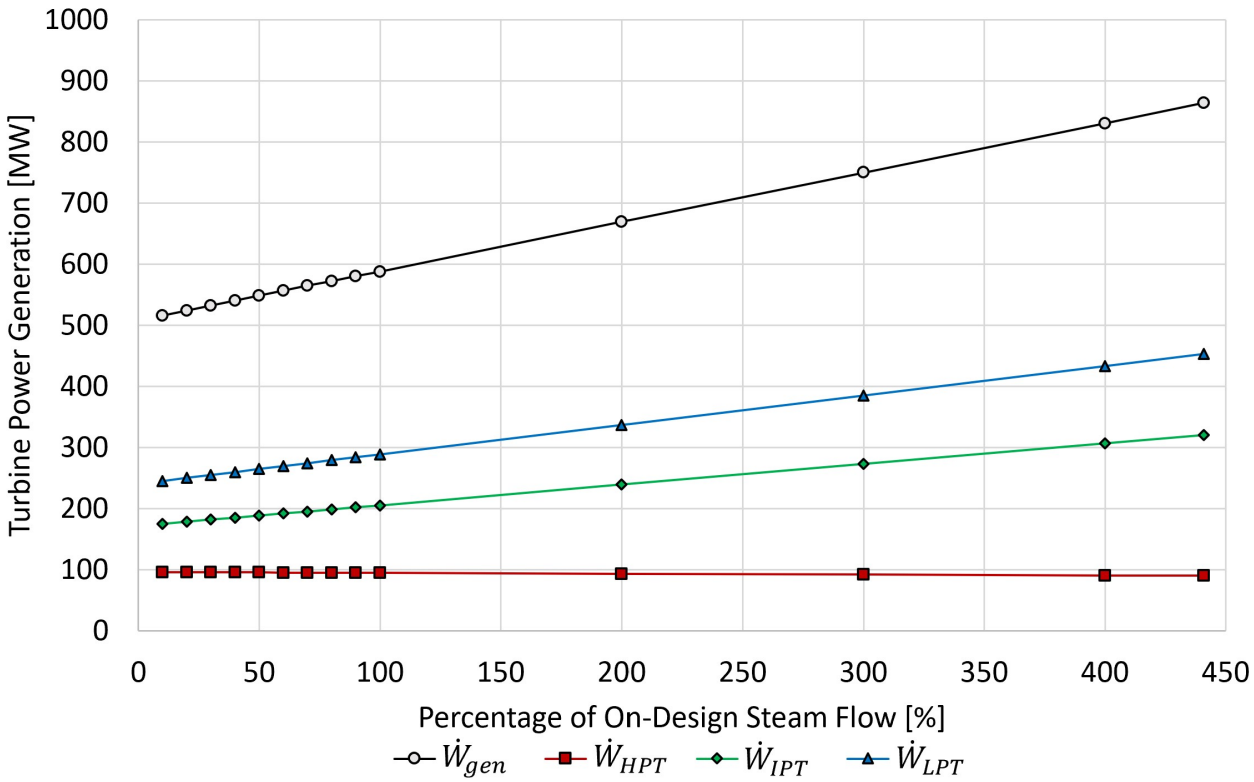

Figure 4.7: HPT, IPT, LPT, and total turbine generation power as a function of percentage steam mass flow rate through the S2W heat exchanger

The increase in mass flow and overall cycle generation reduces the SSRC cycle efficiency from 52.35% in a case with with no salt dispatch, or in 'off' mode, to a value of 51.42% when operating at 100% 'discharging' mode. When increasing mass flow to the above-design conditions, as seen in the maximum 441% 'discharging' case, the efficiency drops further to 49.76%. This observed decrease in cycle efficiency is attributed to the additional heat source — the S2W heat exchanger — lowering the average heat addition temperature of the cycle and increasing the overall mass flow for the IPT and LPT. The 'Discharging' mode of operation increases the mass flow inlet into the IPT and LPT by means of the TES S2W heat exchanger, but due to the lower operating temperature of the hot TES, the mixed steam temperature is reduced at the IPT inlet. With increased mass flow rate through the LPT and IPT turbines power generation proportionally increases while consequently increasing exergy destruction. Additionally, the feedwater mass flow rate increases while operating in the 'discharging' mode cases, requiring a higher work input from the high and low

pressure pumps. All three of these 'discharging' characteristics increase in the 10% to 441% cases negatively impacting cycle efficiency. Displayed in Figure 4.8, a plot of cycle efficiency and total cycle generation as a function of steam mass flow percentages in 'discharging' mode case studies exhibits the aforementioned relationship.

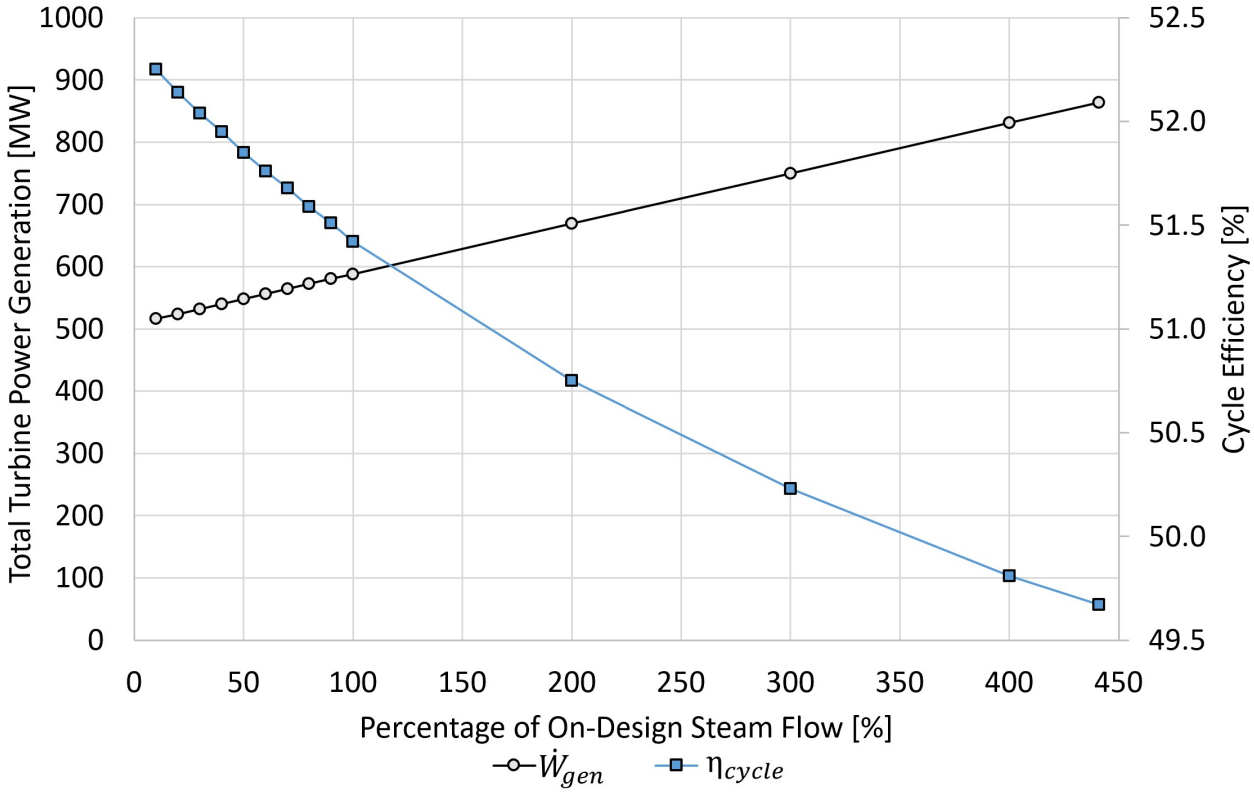

Figure 4.8: Total turbine power generation and cycle efficiency as a function of percentage steam mass flow through S2W heat exchanger

The 'charging' mode of operation experiences smaller changes in mass flow from the turbine exhausts and feedwater through the FWH chain. The small decrease in mass flow rates for FWH A-F in the 10% to 100% 'charging' mode cases results in the FWH UA values decreasing by a marginal amount. The outlier in this case is again FWH G with an increasing UA value as salt mass flow to storage increases. This increasing behavior is attributed to the W2S extracting more heat as the quantity of salt mass flow increases and consequently reduces the heating potential of the HPT turbine exhaust through FWH G. With the heating potential of the turbine exhaust reduced, FWH G UA value is increased to maintain the required heat transfer rate to raise the feedwater temperature. Plots of the UA values and heat transfer rates for FWHs A-G during the 10%-100% 'charging' cases are displayed in Figure 4.9 and Figure 4.10 respectively.

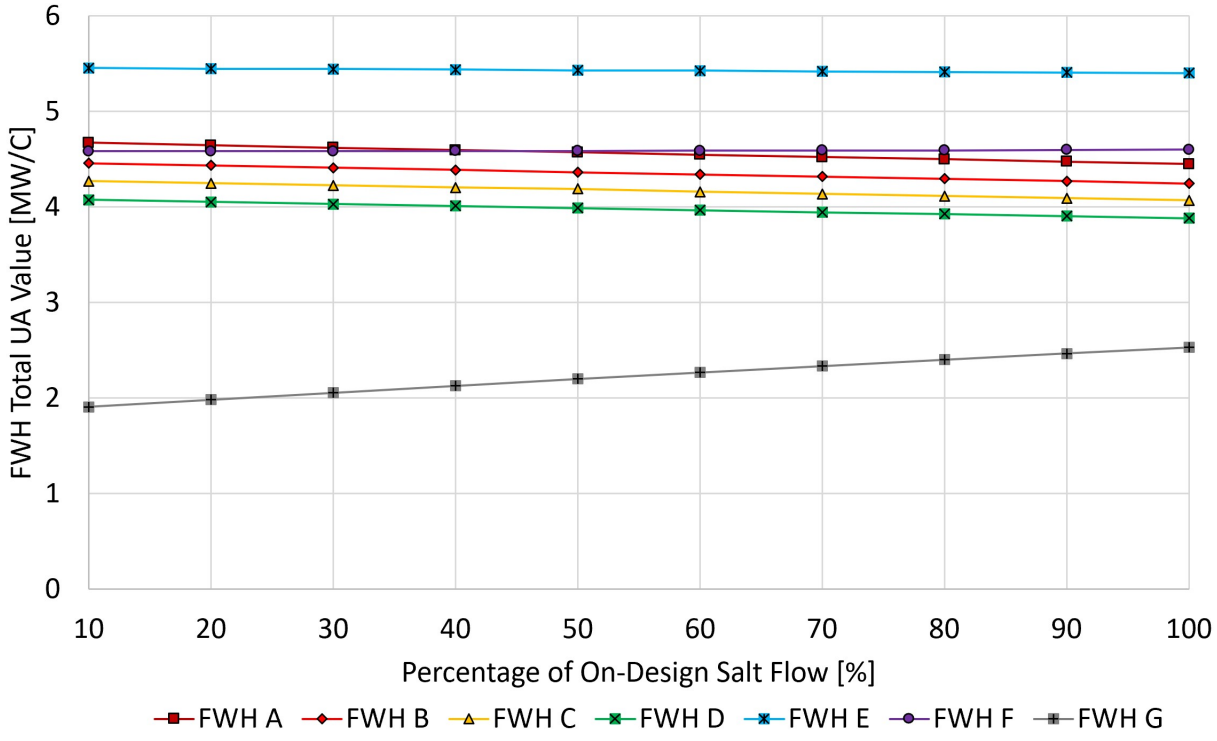

Figure 4.9: UA value for FWH A-G as a function of percentage salt mass flow to storage through the W2S heat exchanger

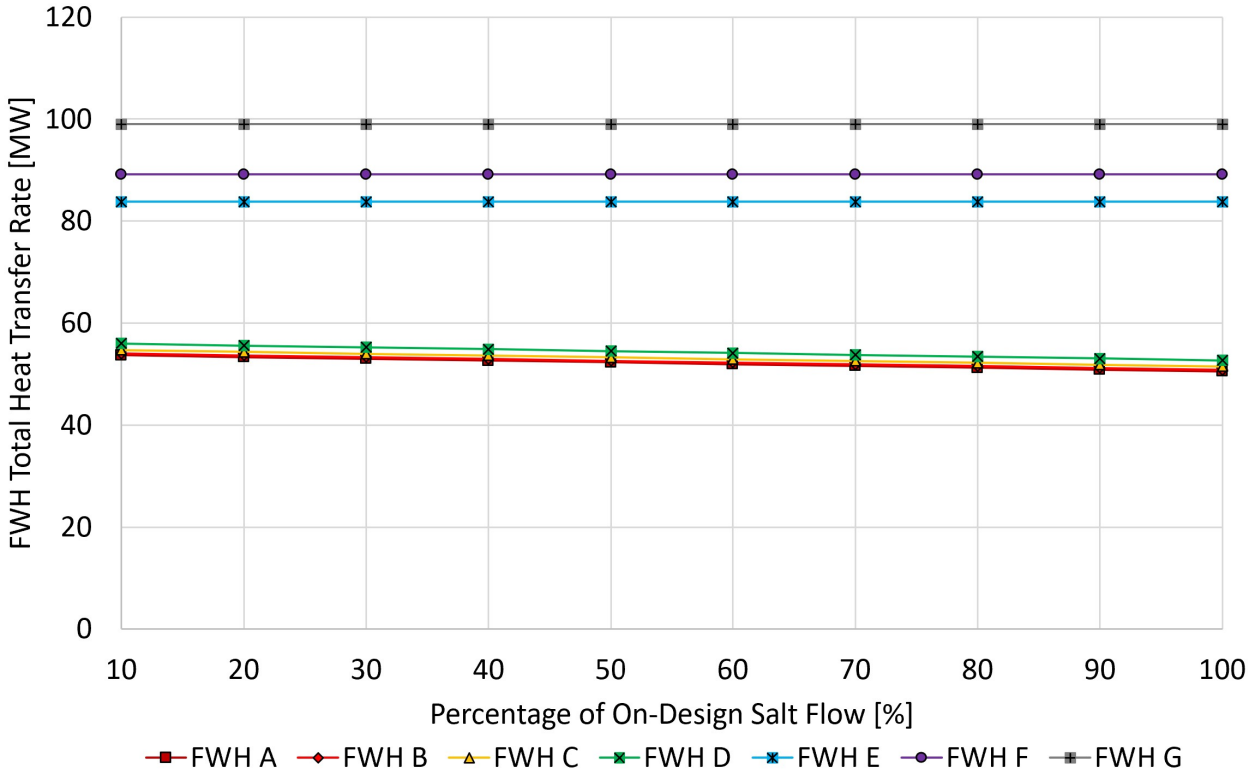

Figure 4.10: Heat transfer in FWH A-G as a function of percentage salt flow to storage through the W2S heat exchanger

In the 'charging' mode of operation cases, a higher percentage of salt mass flow requires a larger quantity of steam mass flow extraction from the HPT exhaust. Increasing the steam mass flow extraction from the HPT reduces the mass flow of high quality steam to the subsequent IPT and LPT turbines, resulting in a reduction in the total power generation. The additional mass flow extracted from the HPT reduces the total power generation, dropping from 508 MW in the 'off' mode to 477.1 MW in 100% 'charging' mode case for a difference of 30.9 MW in generation. The HPT, IPT, and LPT generation and total cycle generation for the 10%-100% 'charging' mode cases is plotted in Figure 4.11.

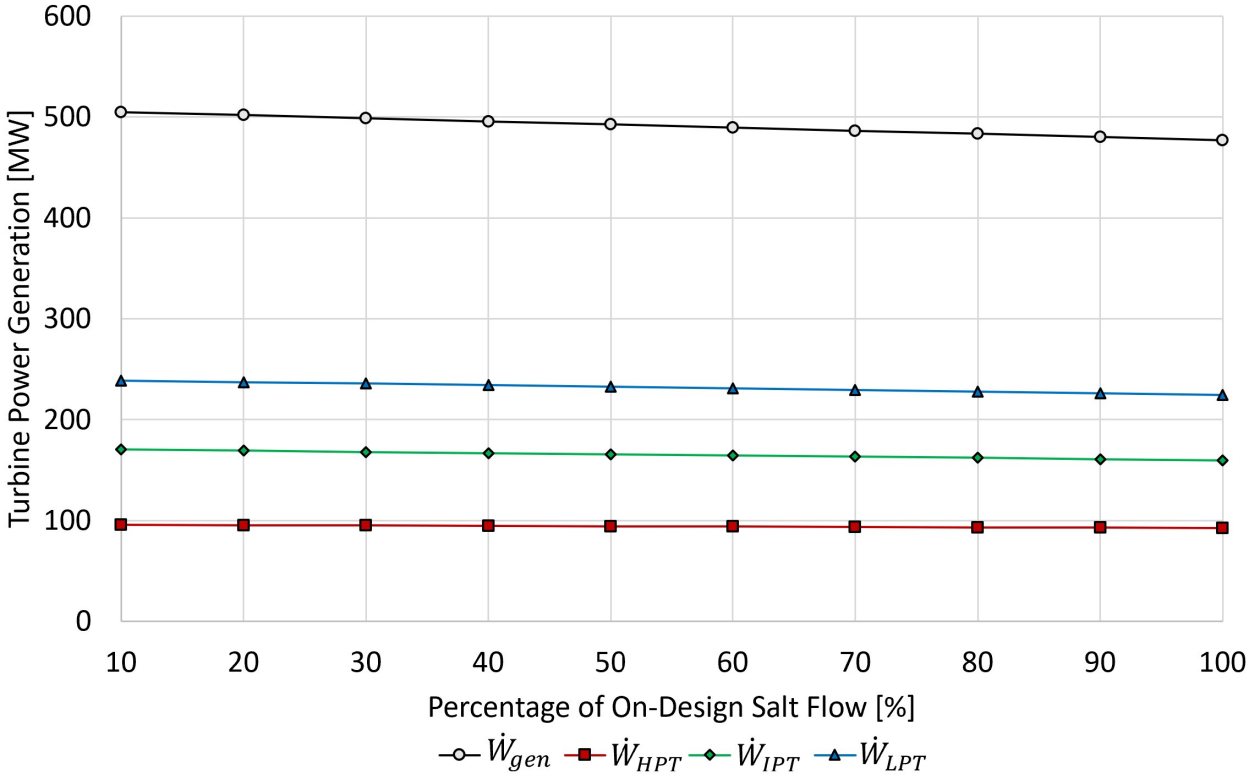

Figure 4.11: HPT, IPT, LPT, and total turbine generation power as a function of percentage salt mass flow rate to storage through the W2S heat exchanger

Cycle efficiency is reduced in the 'charging' mode cases with higher percentages of mass flow because of how cycle efficiency is defined in Equation (4.1). Cycle efficiency is calculated as the ratio of turbine generation minus the pump work to the total heat input into the cycle and does not account for the amount of heat transferred into storage through the W2S heat exchanger. The heat transferred out of the cycle into storage is treated as a loss, when in fact the heat is being stored for later use. Cycle efficiency reduces from 52.35% to 49.18% for a total reduction of 3.17% from 10%-100% 'charging' mode cases. A plot of cycle efficiency and total power generation as a function of the 10% to 100% 'charging' cases is displayed in Figure 4.12.

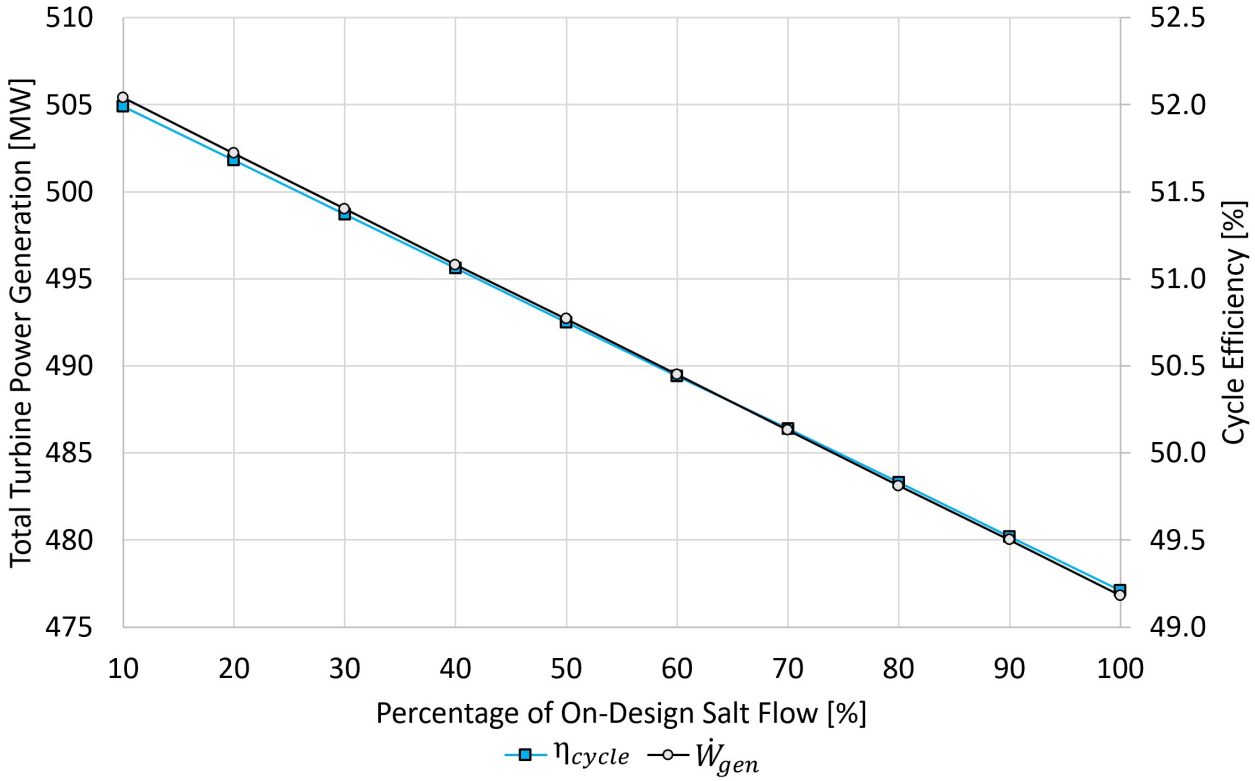

Figure 4.12: Total turbine power generation and cycle efficiency as a function of percentage salt mass flow to storage through W2S heat exchanger

Effective Turbine Isentropic Efficiency

The previous studies for SSRC on-design and off-design assume constant 90% isentropic efficiencies for the HPT, IPT, and LPT turbine stages. This enables equal comparisons between the SSRC and sCO_2 Brayton cycle configurations. However, turbine isentropic efficiency is reduced when the mass flow rate through any given turbine stage deviates from the design-point condition. The study described below considers the effects of varying mass flow rates through the turbines on turbine and cycle efficiency using a scaling technique for the turbine isentropic efficiency that is adapted from Bartlett, 1958 [58]. A cubic curve fit is applied to the data presented from Bartlett et al. for a condensing turbine with one governing stage. Reduction in efficiency (RIE) is calculated from the curve using the throttle flow ratio (TFR) as the independent variable. The data from Bartlett et al. is shown in Figure 4.13 with the equation for the fit curve overlaid onto the data.

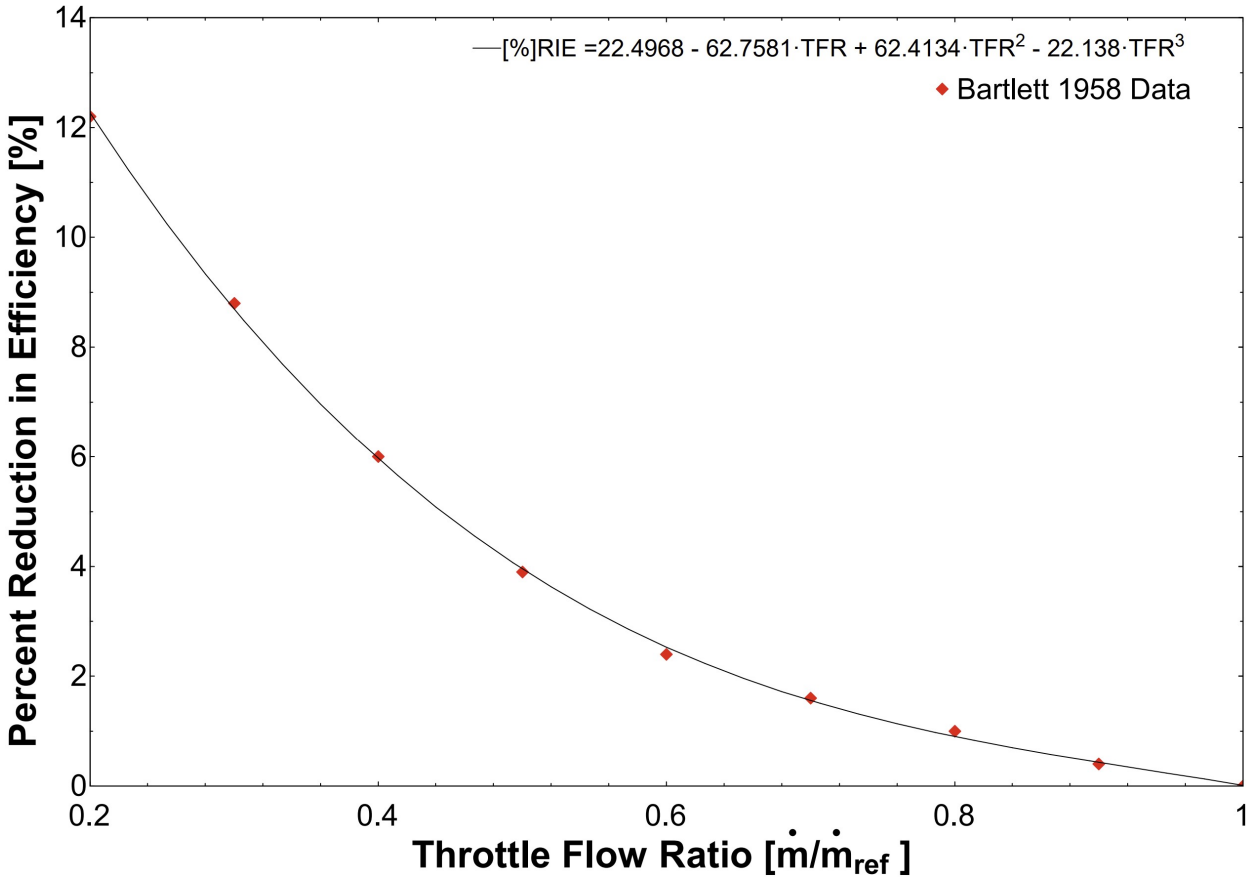

Figure 4.13: Percentage reduction in efficiency for turbine stage as a function of throttle flow ratio

With an equation relating percentage RIE to TFR established, a reference mass flow rate for the inlet to each turbine stage is required. The highest observed mass flow rates, power outputs, and turbine sizing occur in the 100% 'discharging' case, so reference mass flow rates are adopted from this mode of operation. In 'off' and 'charging' mode of operations, TFR value are calculated for the HPT, IPT, and LPT stages, then the individual stages' RIE are calculated from the relationship in Figure 4.13. The RIE value is then used to calculate the isentropic efficiency for each stage in off-design operation and is plotted in Figure 4.14.

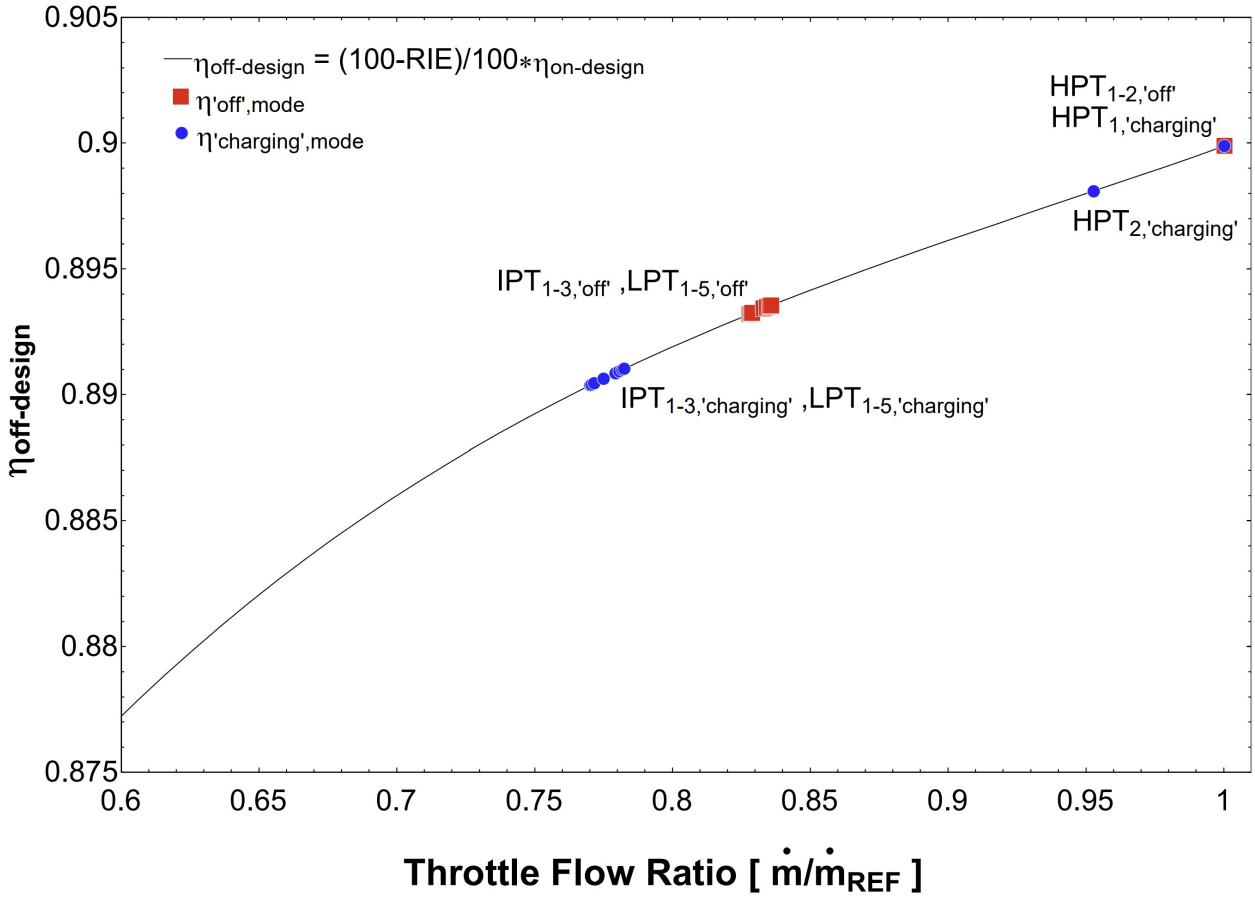

Figure 4.14: Isentropic efficiency in off-design as a function of throttle flow ratio with overlaid stage efficiencies for 100% 'charging' and 'off' modes of operation

In 'off' and 100% 'charging' modes of operation, the mass flow through the turbine stages are lower than in the 100% 'discharging' mode of operation, reducing the efficiencies of turbine stages after the HPT. The second HPT stage in 100% 'charging' mode of operation, HPT2, has a reduced isentropic efficiency because of the higher HPT1 turbine exhaust mass flow rate required to provide heat for TES storage through the W2S heat exchanger. The subsequent turbine stages — IPT1 to IPT3 and LPT1 to LPT5 — experience lower mass flow rates in both 'off' and 100% 'charging' modes than when in 100% 'discharging.' Therefore, the associated isentropic efficiencies for these stages are reduced. Throughout the scaling studies, the isentropic efficiencies are reduced by less than 1% with the lowest predicted efficiencies in 'off' and 100% 'charging' modes of operation at 89.32% and 89.04%, respectively. The power output for 'off' with turbine scaling is 505.8 MW, or a 2.2 MW reduction

due to turbine scaling compared to the case without isentropic efficiency scaling. Similarly, 100% 'charging' mode of operation with turbine scaling is 474.2 MW, or a reduction of 2.9 MW compared to the unscaled 100% 'charging' case.

Round-Trip Efficiency

The heat transfer processes through the S2W and W2S heat exchangers introduce exergetic loss, so use of the TES system has an associated loss in conversion efficiency when 'charging' and 'discharging'. The efficiency loss for heat exchanged into and out of the TES is conventionally termed 'round-trip efficiency.' To calculate accurate round-trip efficiency, FWH UA and turbine isentropic efficiency scaling techniques are employed to calculate the increase of cycle power generation in a 35.8% 'discharging' mode case and the reduction in cycle power generation in the 100% 'charging' mode. The 35.8% 'discharging' case is used because the heat transfer rate through the S2W heat exchanger, 60.9 MW, is equivalent to the 100% 'charging' mode heat transfer rate through the W2S heat exchanger. The round-trip efficiency is then calculated by dividing the 35.8% 'discharging' power gain by the 100% 'charging' power reduction. In 100% 'charging,' the power output with turbine scaling is 474.2 MW, or 33.8 MW less than 'off.' In 35.8% 'discharging,' the cycle power output is 535.4 MW, or 27.4 MW more than 'off'. Therefore, without considering pipe and storage tank thermal losses, the calculated round trip efficiency of the TES is 81.1%.

CSP Conversion Efficiency

Comparison of a CSP steam-Rankine cycle operating in isolation and the CSP integrated into a combined nuclear-solar SSRC can be established by defining a CSP conversion efficiency. The CSP conversion efficiency for the SSRC is defined by the additional cycle power generation divided by the CSP heat contribution to the cycle. In the 100% 'discharging' mode of operation, the cycle is generating 587.8 MW, generating an additional 79.8 MW of power to the grid. The quantity of heat transfer through the S2W heat exchanger, which

represents the total amount of heat put into the cycle by the CSP, in 100% 'discharging' case is calculated at a value of 168.5 MW. Considering the gain in cycle power, 79.8 MW, divided by the amount of additional heat when the TES is discharging, 168.5 MW, the CSP conversion efficiency is calculated at 47.4%. This CSP conversion efficiency is higher than the CSP operation in isolation, 40-45%, exemplifying the observed benefits of a combined nuclear-solar power cycle [59, 60].

4.4 Summary

In this chapter, an integrated CSP and LFR SSRC with TES is modeled, and design criteria and performance metrics are calculated for the three modes of operation: 'off', 'charging' and 'discharging'. The design approach is outlined with discussions of the heat exchanger, FWH, turbine, CSP, full SSRC model, and off-design methodology. Important complications — specifically on the turbine moisture separation and FWH G — are analyzed with plausible solutions explained. The calculations used to scale the FWH on-design UA values to the representative off-design UA values in the mode of operation case studies are provided with procedure descriptions. The results from on-design 100% 'off', 'charging', and 'discharging' modes of operation are examined, with performance metrics discussed. Appendix B provides SSRC and CSP cycle diagrams with overlaid states points for the three on-design modes of operation. Finally, off-design cases characterize 'charging' mode in the range of 10%-100% and 'discharging' mode in the range of 10%-441%. Results are plotted with trends of performance metrics as functions of salt or steam mass flow percentages are analyzed.

5 CONCLUSIONS AND FUTURE WORK

5.1 Conclusion

This thesis studies the modeling of integrated LFR and CSP power cycles with TES. Two dissimilar power cycles, sCO_2 recompression Brayton and SSRC are considered; the modeling methodologies of the full cycles and cycle components are explained, and associated equations, challenges, and assumptions are discussed. The resulting performance metrics and design criteria from the integrated LFR and CSP power cycle studies are presented with outcomes justified. The cycle descriptions and associated conclusions serve as a reference for future cycle design and proof-of-concept considerations. Further study and validation must be done before these cycles are used for plant design. The conclusions from the integrated power cycle studies are stated below starting with sCO_2 Brayton cycle (non-charging and charging) configurations, then SSRC (on-design and off-design) modes of operation, and finally comparisons between the two cycle types. The conclusions are followed by multiple areas of future work with an integrated energy system and modeling improvements outlined.

sCO_2 Brayton Cycle Configurations

Non-charging configurations:

The non-charging sCO_2 Brayton cycle configurations are listed below. This list aims to provide an overview of each non-charging cycle configuration with discussion of cycle performance and considerations.

- Two-cycle "C-LFR-ON and C-CSP-ON": This cycle configuration has dedicated recompression cycles for the LFR and CSP heat inputs, offering the highest cycle efficiency of the studied sCO_2 Brayton cycle configurations. The high observed cycle efficiency is due to the two cycles operating individually when generating electrical power,

allowing for tailored optimization. With separate cycles, components are not shared between heat sources and therefore there is a lack of synergy.

- C-1HTR1T-ON: This single cycle configuration has parallel heat additions from the CSP and LFR. Due to sharing of cycle components, this configuration is the least complex and therefore the most cost efficient and compact. With both CSP and LFR discharging, cycle efficiency is reduced by 0.88% when compared to the two-cycle configuration combined efficiency.

- C-2HTR3T-ON: This single cycle configuration has dedicated turbines and HTRs for the LFR and CSP. This cycle offers a compromise between (i) complexity with reduced cycle component redundancy, (ii) flexibility for dissimilar inlet temperatures on the CSP and LFR inlet, and (iii) median efficiency. The efficiency is only marginally higher than C-1HTR1T-ON, but heat storage efficiency is improved when using the LFR to charge the salt due to flexibility in setting the CSP and LFR inlet temperatures. As the additional turbines would likely be present in practice, the cost and complexity of this cycle is not expected to be significantly higher than C-1HTR1T-ON. The merits of C-2HTR3T-ON and C-1HTR1T-ON are therefore relatively similar. It is noted that for the unconstrained case C-2HTR3T achieves almost identical performance to the two-cycle configuration with an efficiency of 46.1%, and, hence, the drop in performance relative to using separate cycles is attributable to the constraint on LFR inlet temperature being more limiting.

Thermal energy storage charging techniques:

Thermal energy storage charging techniques are listed below with their orientation in the non-charging configurations described. This list includes implementation considerations for each technique with emphasis on complexity, flexibility to heat inputs, and heat storage efficiency.

- C-LFR-POST: This charging technique has the turbine after the C2S heat exchanger and was found to be infeasible due to large reductions in thermodynamic efficiency.
- C-LFR-PRE: This charging technique has the turbine before the C2S heat exchanger with a valve that bypasses the turbine, demanding a higher outlet temperature for the LFR to be effective. Due to LFR outlet temperature limitations, this configuration has the next lowest heat storage efficiency.
- C-LFR-PAR: This charging technique splits the flow directly after the LFR with the turbine and C2S heat exchanger positioned in a parallel configuration. The resulting heat storage efficiency for C-LFR-PAR is higher than the C-LFR-PRE charging technique.
- C-LFR-CIRC: This charging technique has a separate circulation loop and is the most flexible charging technique with the heat storage efficiency being highly dependent on cold TES temperature and LFR inlet temperature. This charging technique achieves heat storage efficiency to near 100% by eliminating losses associated with the turbines and compressors. When implemented into C-1HTR1T-ON cycle configuration, the heat storage efficiency is limited to 90% because the inlet temperatures to the LFR and CSP are constrained to be the same. The additional chiller and circulator components in the circulation loop increases complexity and cost of this charging technique.

The non-charging configurations offer trade-offs between complexity and flexibility to CSP and LFR inlets: the two-cycle configuration has redundant cycle components, C1HTR1T-ON is least complex but rigid on CSP and LFR temperatures, and the C-2HTR3T-ON is a median between complexity and flexibility. Therefore, choice of cycle is determined by the cycle use-case, with advantages and disadvantages contemplated. Regarding thermal energy storage techniques, the C-LFR-PAR and C-LFR-CIRC are the most promising options going forward. The choice among these two involves a trade-off between heat storage efficiency

and component costs, and the performance of C-LFR-CIRC also depends on the choice of the charging configuration.

Supercritical Steam-Rankine Cycle

The three on-design SSRC modes of operation are briefly described and listed below. The list includes efficiency and power output of each mode of operation.

On-design:

- 'off': The SSRC in this mode of operation has the LFR operating as a base load to the grid in without interactions from CSP or TES. The results indicate that the cycle efficiencies are the highest of all three modes of operation at 52.35% and an intermediate power generation value of 508.0 MW.
- 'charging': In this mode of operation the steam exhaust extraction from the HPT is increased and has a fractional amount of heating potential stored through the W2S heat exchanger into hot TES for dispatch at a later time. The lower mass flow rates through subsequent IPT and LPT reduces total power production from the SSRC to 477.1 MW while lower efficiencies of 49.18% are observed.
- 'discharging': In this mode of operation salt from hot TES is dispatched exchanging heat to the SSRC through the S2W heat exchanger, increasing steam mass flow rate through IPT and LPT, and beneficially increasing cycle power generation. The cycle efficiency is 51.42% and generation increases to 587.8 MW during this mode of operation.

Off-design:

Fractional amounts of the 'charging' and 'discharging' modes of operation, or off-design cases, are listed below. The range of power production and salt or steam mass flow for

each mode of operation are included.

- 10%-100% 'charging': This study examined the 'charging' mode of operation when mass flow of salt to storage is varying from 19 kg/s to 190 kg/s. The results show incremental reductions in cycle power output from 508.0 MW to 477.1 MW for a range of 30.9 MW.

- 10%-100% 'discharging': In this study, additional steam mass flow rate through IPT and LPT during 'discharging' mode of operation is increased from 10 kg/s to 100 kg/s. The resulting cycle power generation is increased from 508 MW to 587.8 MW for a range of 79.8 MW.

- 100%-441% above-design 'discharging': In the above-design study salt is dispatched from hot TES at a higher rate than on-design. Larger salt mass flows increase the heat transfer through the S2W heat exchanger resulting in increased additional steam mass flow rates from 100 kg/s up to 441 kg/s. The increased steam mass flow to IPT and LPT consequently increases the total power output up to 863.8 MW at 49.67% cycle efficiency. These above-design cases assume feasible turbine operation when steam mass flow rates are increased by a large margin.

The on-design modes of operation demonstrate the SSRC's load following capability from 477.1 MW to 587.8 MW with a range of 110.7 MW. Higher resolution off-design studies for incremental percentages of 'charging', 'discharging', and above-design 'discharging' modes of operation are conducted with UA values adjusted. The on-design and off-design case studies show persuasive results for integrated CSP and LFR SSRC with TES adaptability to grid demand by incrementally increasing or decreasing TES salt dispatch or storage while the LFR maintains full capacity operation.

sCO_2 Brayton Cycle and Supercritical Steam-Rankine Cycle

This concluding section compares and contrasts the two cycle types with an emphasis on synergy, cycle efficiency, and power generation. Synergistic operation of the LFR and CSP is an important consideration that enables cost reduction. Coupling the technologies to a singular cycle takes advantage of shared cycle components. In the context of synergies, the favored sCO_2 Brayton cycle is the C-2HTR3T-ON in which the CSP and LFR heat sources share cycle components while still accommodating the dissimilar operating temperatures of each. C-2HTR3T-ON coupled with the C-LFR-CIRC charging technique allows for flexibility to the distinct operating temperatures required for the LFR and TES. In the SSRC, the turbine exhaust from the HPT can have its extraction pressure and mass flow adjusted to accommodate different TES hot and cold storage tank temperatures. Additionally, turbine extraction mass flow to the FWHs can be increased or decreased to raise the temperature of the feedwater to an appropriate level for the LFR inlet conditions. If chosen technologies for the nuclear or solar heat inputs largely differ in temperature or heat input, both of these cycles with their high associated synergies are attractive.

Comparing cycle efficiency yields a different sCO_2 Brayton cycle configuration. The 2-Cycle sCO_2 Brayton cycle configuration with C-LFR-ON and C-CSP-ON allows for individual efficiency optimization for the two cycles operating with dissimilar heat sources. Efficiencies of 45.28% and 45.93% are observed for C-LFR-ON and C-CSP-ON respectively. Comparing to the SSRC in the three on-design modes of operation, 'off', 'charging' and 'discharging' with respective cycle efficiencies of 52.35%, 49.18%, and 51.42%, the SSRC has higher cycle efficiencies across all cases. Therefore, if cycle efficiency is an important decision parameter, then a reasonable choice is the SSRC.

The non-charging sCO_2 recompression Brayton cycle configurations operate without storing salt in the TES hot tank, meaning the salt mass flow rate discharging from the TES hot storage is equal to the flow rate to storage from the receiver. With a cold TES temperature of 390 °C and hot TES temperature of 560 °C, the resulting mass flow rate

of salt through the CSP HX is 2885 kg/s. In the SSRC models, the TES hot tank is at an identical temperature as the sCO_2 Brayton cycles, 560 °C, but the TES cold tank temperature is 40 °C lower at 350 °C due to LFR inlet temperature requirements. Considering the TES hot and cold storage temperatures with no storage term, the most comparable salt mass flow rates through the S2W HX in the SSRC models is 2340 kg/s observed in the SSRC 441% 'discharging' mode of operation case. Therefore, comparisons in cycle generation will be made between the SSRC operating in the 441% 'discharging' case to the sCO_2 Brayton cycle configurations with cold and hot TES tank temperatures of 390 °C and 560 °C respectively. In the SSRC 441% 'discharging' mode case total power generation is 863.8 MW while the sCO_2 Brayton cycle with the highest output power is C-2HTR3T-ON with 783.7 MW. If it is assumed that pumping power for the low pressure and high pressure pumps is provided from the cycle and therefore is subtracted from the power generation, the total power generation of the SSRC 441% 'discharging' mode is still higher than all sCO_2 at 825.0 MW. When power generation is an important choice consideration, SSRC generates 80.1 MW more energy than the sCO_2 Brayton configurations, and would be the preferred option for future work.

5.2 Future Work

The sCO_2 recompression Brayton Cycle and SSRC discussed in this thesis are the candidate power cycles for a future Integrated Energy System (IES). The IES combines multiple models; power cycle, LFR, CSP, electrical grid, and a multi-effect distillation process in an interacting simulation system. A diagram of the IES is illustrated in Figure 5.1.

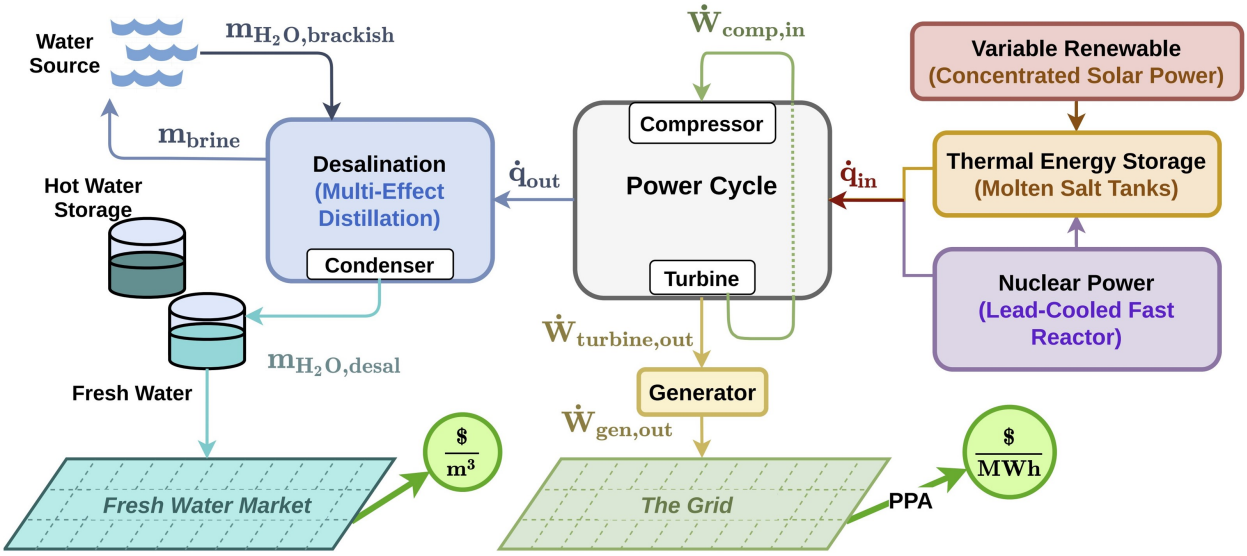

Figure 5.1: IES with the SSRC or sCO_2 Brayton as primary power cycle. [1]

In the IES, the power cycle model receives heat input and temperature performance map information from CSP and LFR models, while outputting heat rejection and electrical generation performance maps. The heat rejection map generated from the power cycle model is utilized in a peripheral system, specifically a multi-effect distillation (MED) process for desalination of sea, or brackish, water. An MED system contains multiple stages where brackish water is sprayed onto a series of heat exchangers which draw heat from the power cycle acting as the cycle's condenser or pre-cooler. In this process, some of the brackish water evaporates and continues to the subsequent MED stages until the salt concentration reduces to an acceptable level. The volume of desalinated water and fresh water market pricing is simulated by the MED model while calculating the additional revenue stream to the IES. The grid simulation model is used to predict the amount of

cycle power generation required to instantaneously match grid demand while calculating the revenue for the IES from a power purchase agreement.

Additional future studies on integrated LFR and CSP power cycles could improve upon the approximations which were made while modeling the power cycles in this thesis. The assumptions and simplifications include turbine and compressor constant isentropic efficiencies, constant pump efficiencies, black-box approximations for LFR and CSP receiver heat inputs, steady state cycle operation, and TES dispatch studies. Implementing scaling techniques for the turbine, compressor, and pump efficiencies would yield power generation and cycle efficiency with increased accuracy. Detailed heat exchanger modeling with transient conditions for the CSP receiver, LFR, and condenser could provide insight into power plant ramp rates and temporal flexibility to grid demand. TES sizing with salt dispatch studies could bring insight into the total amount of energy storage required for daily grid demand. Specifically, the models developed in this thesis for the combined LFR-CSP and LFR or CSP in isolation can be used for dispatch optimization studies on the TES and grid demand within National Renewable Energy Laboratory's System Advisor Model. The final foreseeable study is an economic study on the initial capital and operating costs to examine the cost incentive of constructing an integrated LFR and CSP power cycle with TES.

A SSRC ON-DESIGN STATE POINTS

Table A.1: SSRC model state points from 'off', 'charging', and 'discharging' with CSP.

State	*off*			*charging*			*discharging*		
Number	$\dot{m}$ [kg/s]	P [Bar]	T [°C]	$\dot{m}$ [kg/s]	P [Bar]	T [°C]	$\dot{m}$ [kg/s]	P [Bar]	T [°C]
1	480.10	330.00	340.00	480.10	330.00	340.00	480.10	330.00	340.00
2	480.10	330.00	632.00	480.10	330.00	632.00	480.10	330.00	632.00
3	48.21	236.50	570.00	78.29	236.50	570.00	58.43	236.50	570.00
4	48.21	236.50	570.00				58.43	236.50	570.00
5	431.90	163.60	505.90	401.80	164.00	506.20	521.70	164.10	501.00
6	40.45	90.70	412.80	37.66	91.41	414.00	49.11	91.62	409.40
7	33.17	51.41	333.70	30.65	51.76	334.60	40.28	51.87	330.40
8	21.41	25.44	248.80	18.56	25.44	248.80	25.78	25.44	244.90
9	336.90	25.44	248.80	315.00	25.44	248.80	406.50	25.44	244.90
10	30.87	12.39	189.40	28.89	12.36	189.30	38.60	12.42	189.50
11	34.64	4.87	150.90	32.38	4.86	150.80	41.94	4.91	151.10
12	31.94	1.56	112.50	29.86	1.55	112.40	38.44	1.57	112.80
13	28.91	0.37	74.10	27.02	0.37	74.01	34.73	0.38	74.38
14	210.50	0.05	32.87	196.80	0.05	32.87	252.80	0.05	32.87
15	336.90	0.05	32.87	315.00	0.05	32.87	406.50	0.05	32.87
16	336.90	25.44	33.00	315.00	25.44	33.00	406.50	25.44	33.00
17	336.90	25.44	71.38	315.00	25.44	71.38	406.50	25.44	71.38
18	336.90	25.44	109.80	315.00	25.44	109.80	406.50	25.44	109.80
19	336.90	25.44	148.10	315.00	25.44	148.10	406.50	25.44	148.10
20	336.90	25.44	186.50	315.00	25.44	186.50	406.50	25.44	186.50
21	480.10	25.44	218.30	480.10	25.44	218.30	580.10	25.44	218.30
22	480.10	330.00	224.90	480.10	330.00	224.90	580.10	330.00	224.90
23	480.10	330.00	263.30	480.10	330.00	263.30	580.10	330.00	263.30
24	480.10	330.00	301.60	480.10	330.00	301.60	580.10	330.00	301.60
25	48.21	236.50	306.00	78.29	236.50	308.00	58.43	236.50	307.20
26	88.66	90.70	268.30	116.00	91.41	270.10	107.50	91.62	268.80
27	121.80	51.41	229.90	146.60	51.76	231.40	147.80	51.87	230.40
28	30.87	12.39	153.10	28.89	12.36	153.00	38.60	12.42	153.70
29	65.51	4.87	114.80	61.27	4.86	114.60	80.55	4.91	115.30
30	97.45	1.56	76.41	91.13	1.55	76.27	119.00	1.57	76.93
31	126.40	0.37	38.07	118.20	0.37	37.93	153.70	0.38	38.55
32	480.10	330.00	340.00	480.10	330.00	340.00	580.10	330.00	340.00
33	.	.	.	.	.	.	100.00	330.00	340.00
34	.	.	.	.	.	.	100.00	330.00	545.90
35	.	.	.	78.29	236.50	570.00	.	.	.
36	.	.	.	78.29	236.50	398.30	.	.	.
CSP	*off*			*charging*			*discharging*		
s1	.	.	.	2340.00	30.00	350.00	2340.00	30.00	350.00
s2	.	.	.	2340.00	67.24	350.10	2340.00	67.24	350.10
s3	.	.	.	2340.00	67.24	560.00	2340.00	67.24	560.00
s4	.	.	.	.	.	.	525.00	30.00	560.00
s5	.	.	.	.	.	.	525.00	67.24	560.20
s6	.	.	.	.	.	.	525.00	67.24	350.00
s7	.	.	.	190.00	30.00	350.00	.	.	.
s8	.	.	.	190.00	67.24	350.10	.	.	.
s9	.	.	.	190.00	67.24	560.00	.	.	.

B SSRC 'OFF', 'CHARGING', AND 'DISCHARGING' MODE ON-DESIGN CYCLE DIAGRAMS WITH STATE POINTS

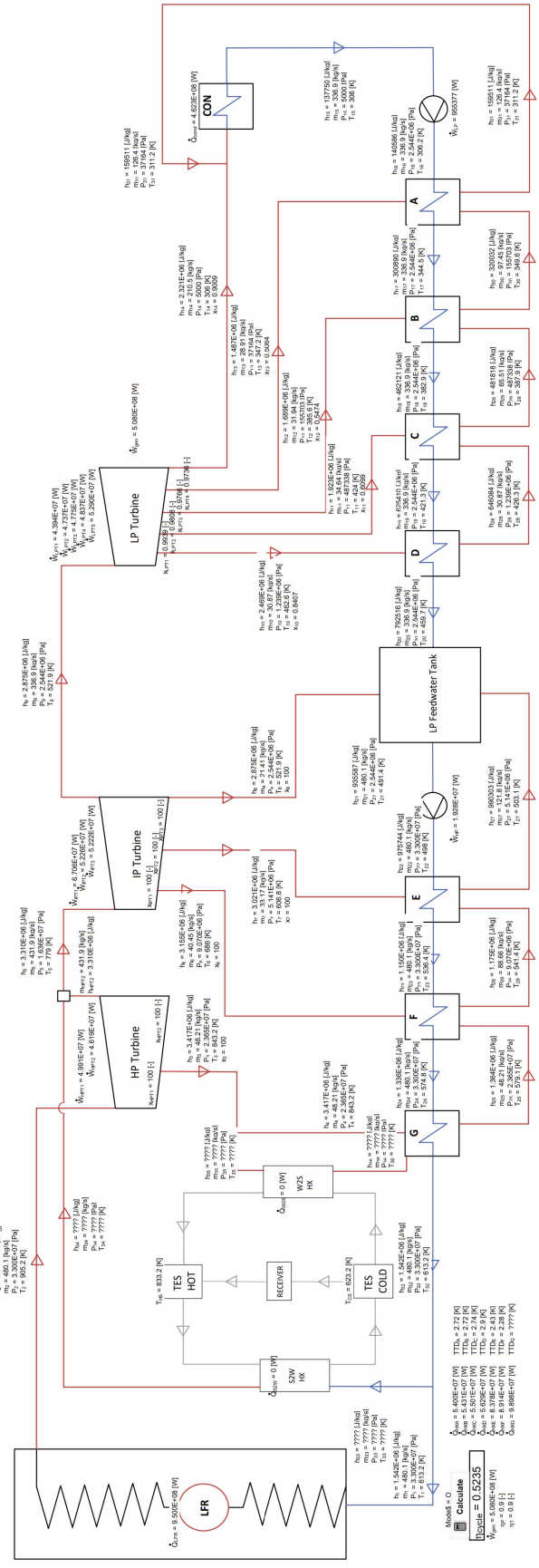

Figure B.1: SSRC state point diagram operating at 100% 'off' mode on-design case

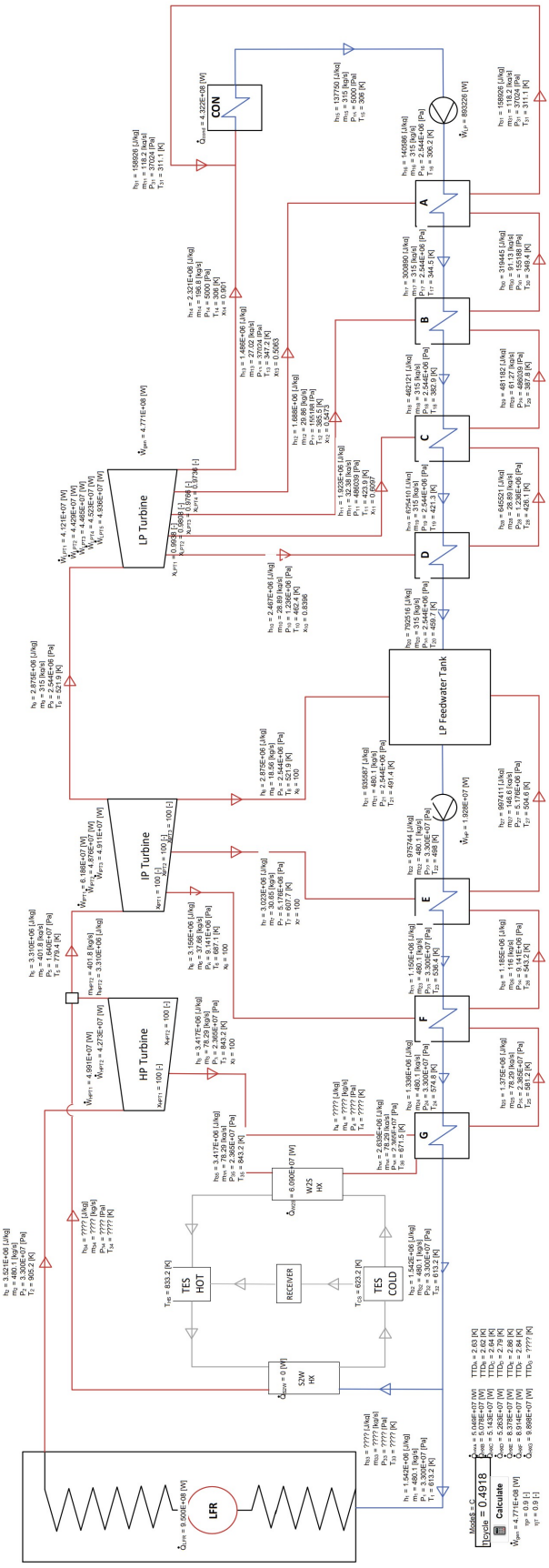

Figure B.2: SSRC state point diagram operating at 100% 'charging' mode on-design case

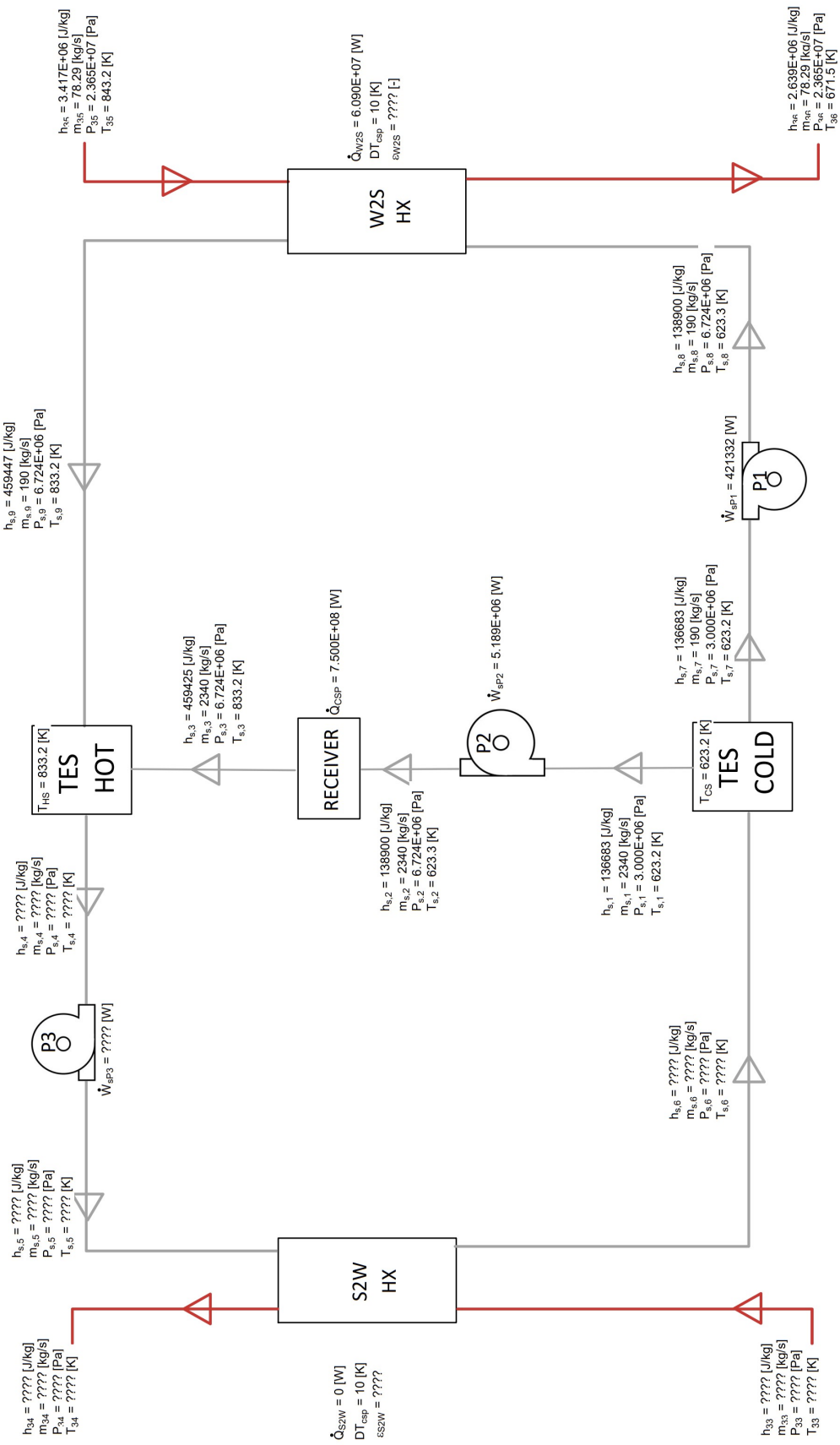

Figure B.3: SSRC CSP state point diagram operating at 100% 'charging' mode on-design case

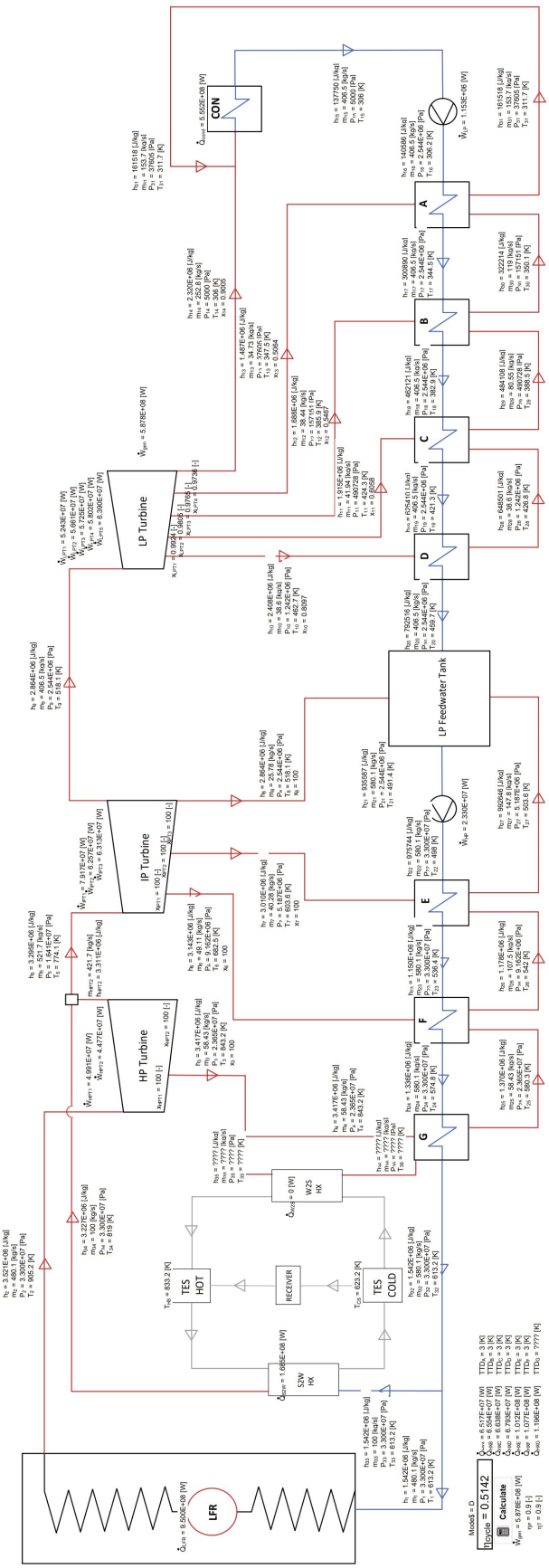

Figure B.4: SSRC state point diagram operating at 100% ‘discharging’ mode on-design case

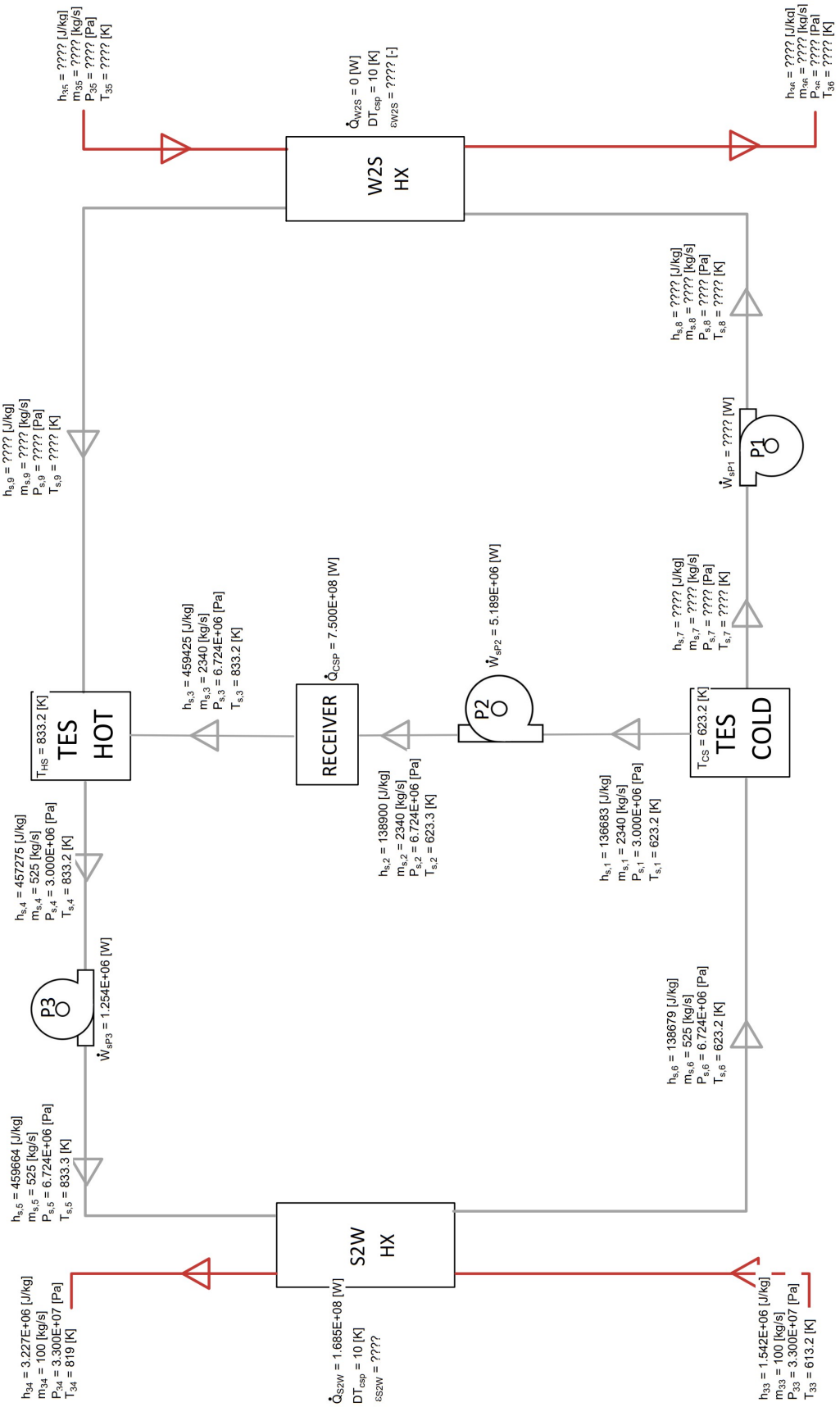

Figure B.5: SSRC CSP state point diagram operating at 100% 'discharging' mode on-design case

C sCO2 BRAYTON CYCLE DIAGRAMS WITH STATE POINTS

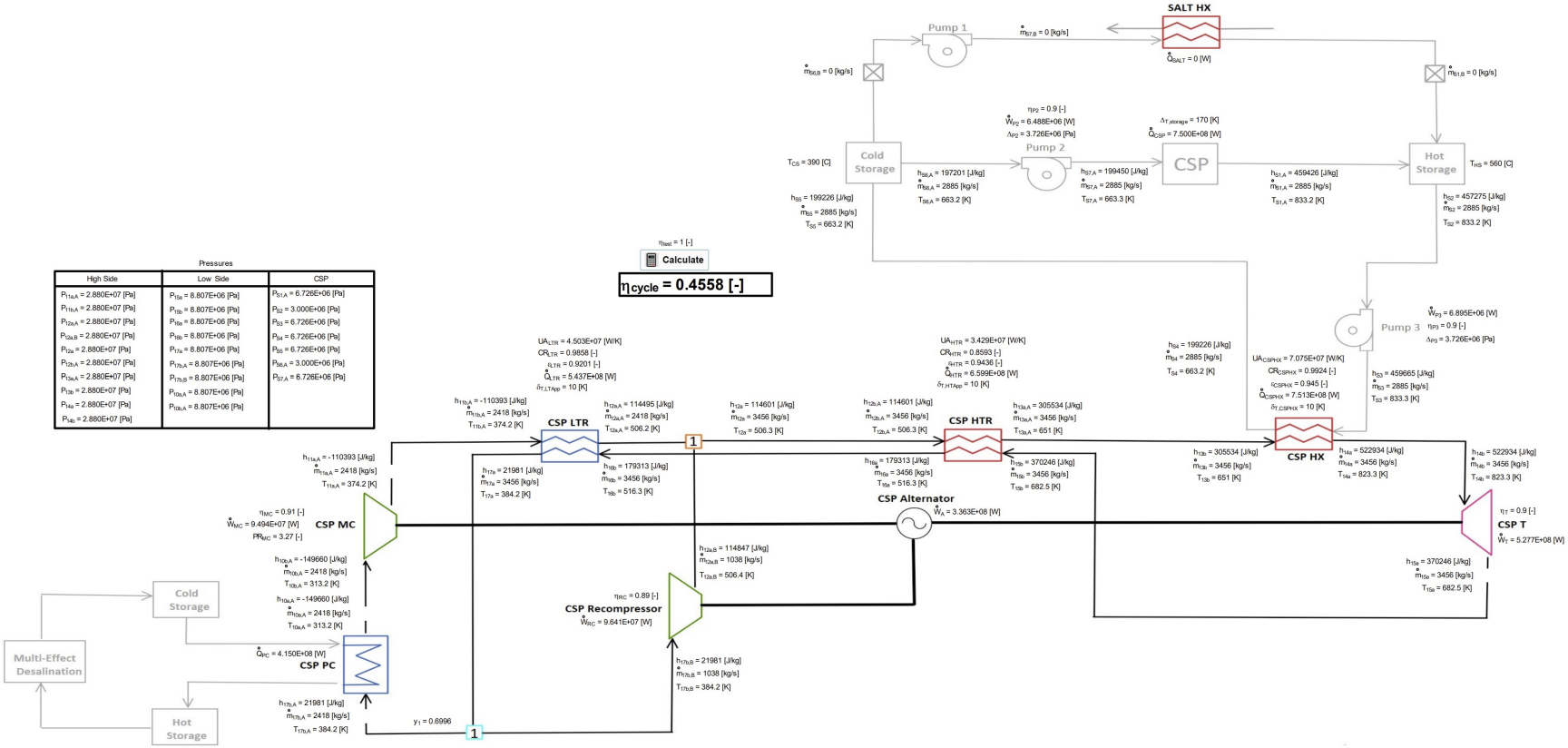

Figure C.1: sCO_2 Brayton Cycle C-CSP-ON operating with cold storage of 390 C

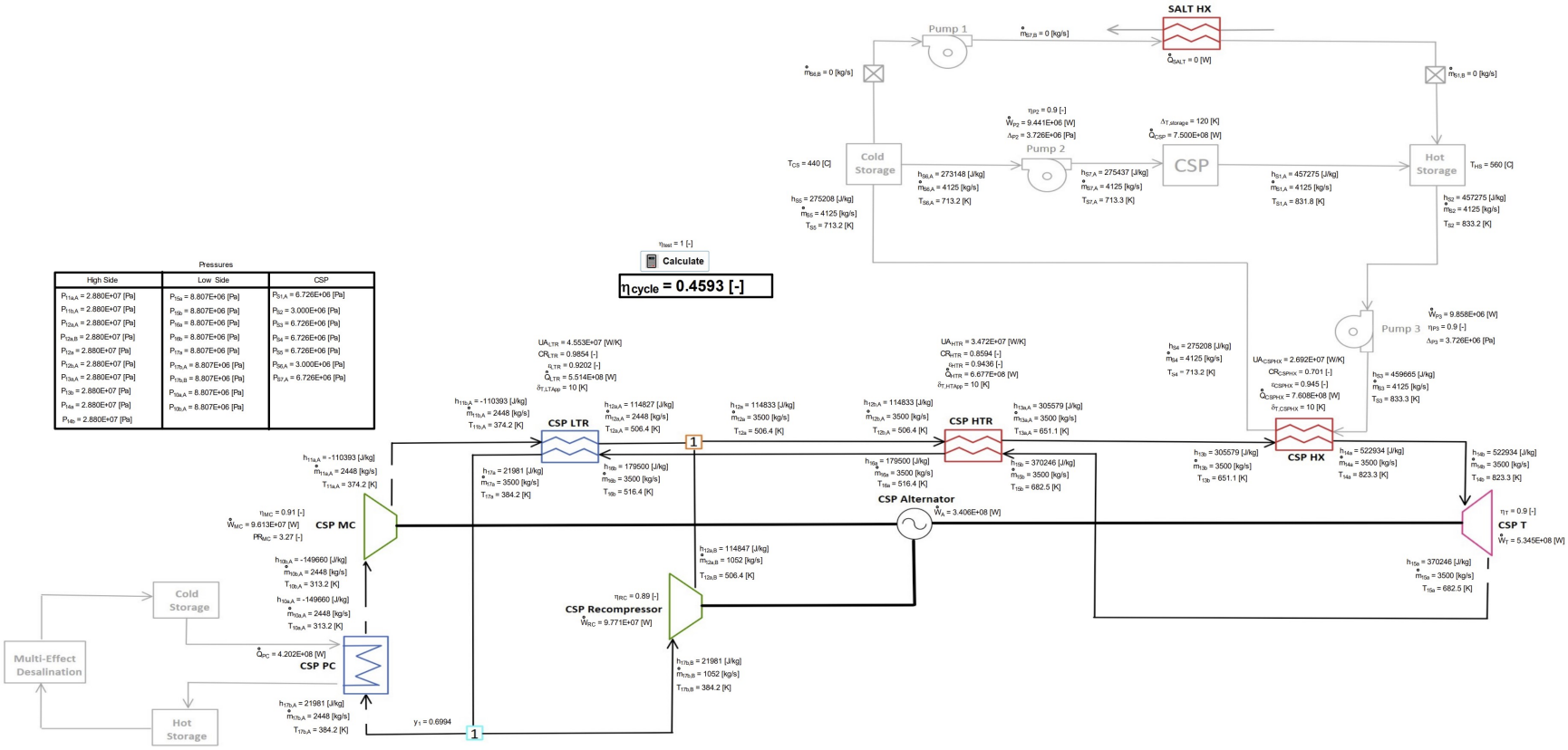

Figure C.2: State point diagram of sCO_2 Brayton cycle C-CSP-ON operating with cold storage of 440 C

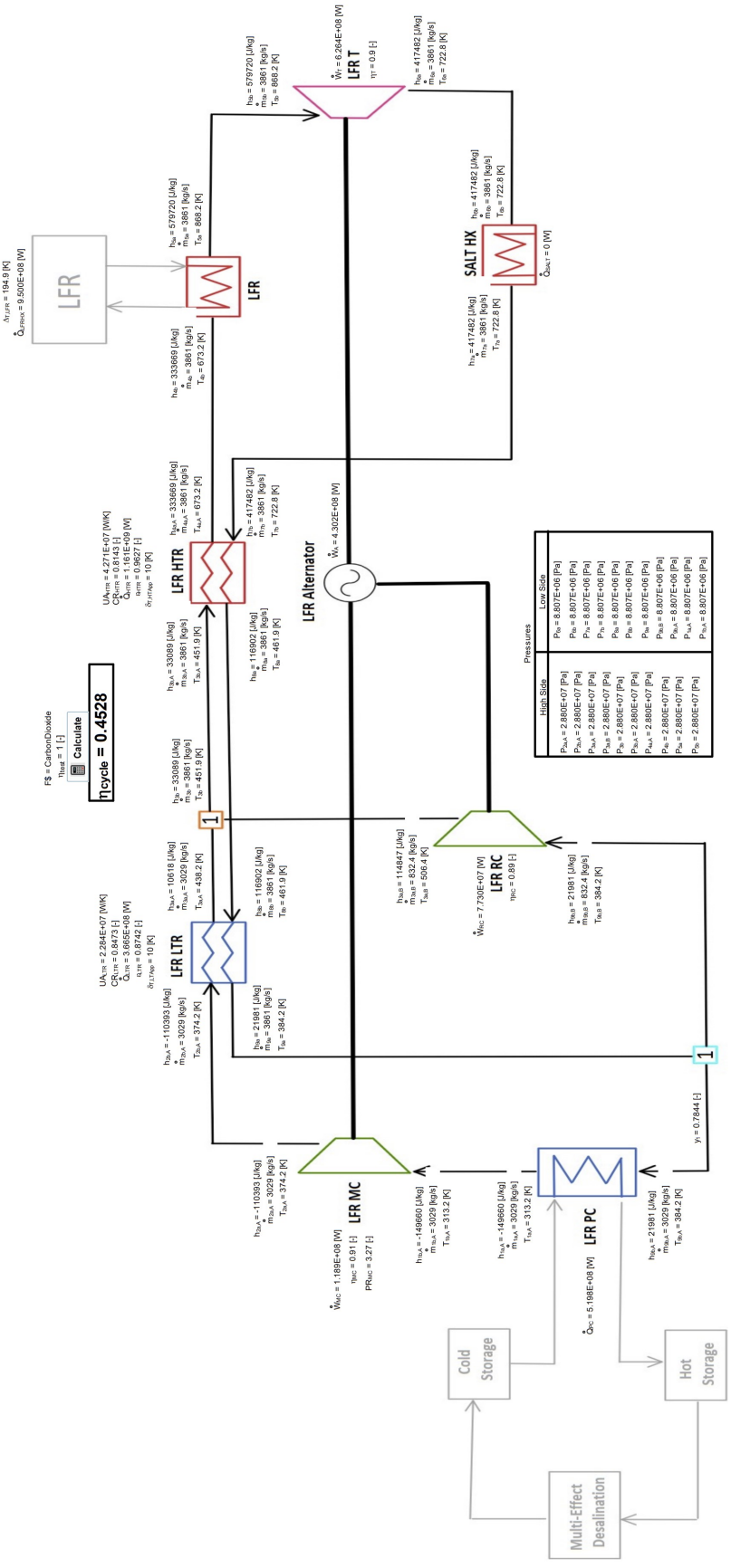

Figure C.3: State point diagram of sCO_2 Brayton Cycle C-LFR-ON

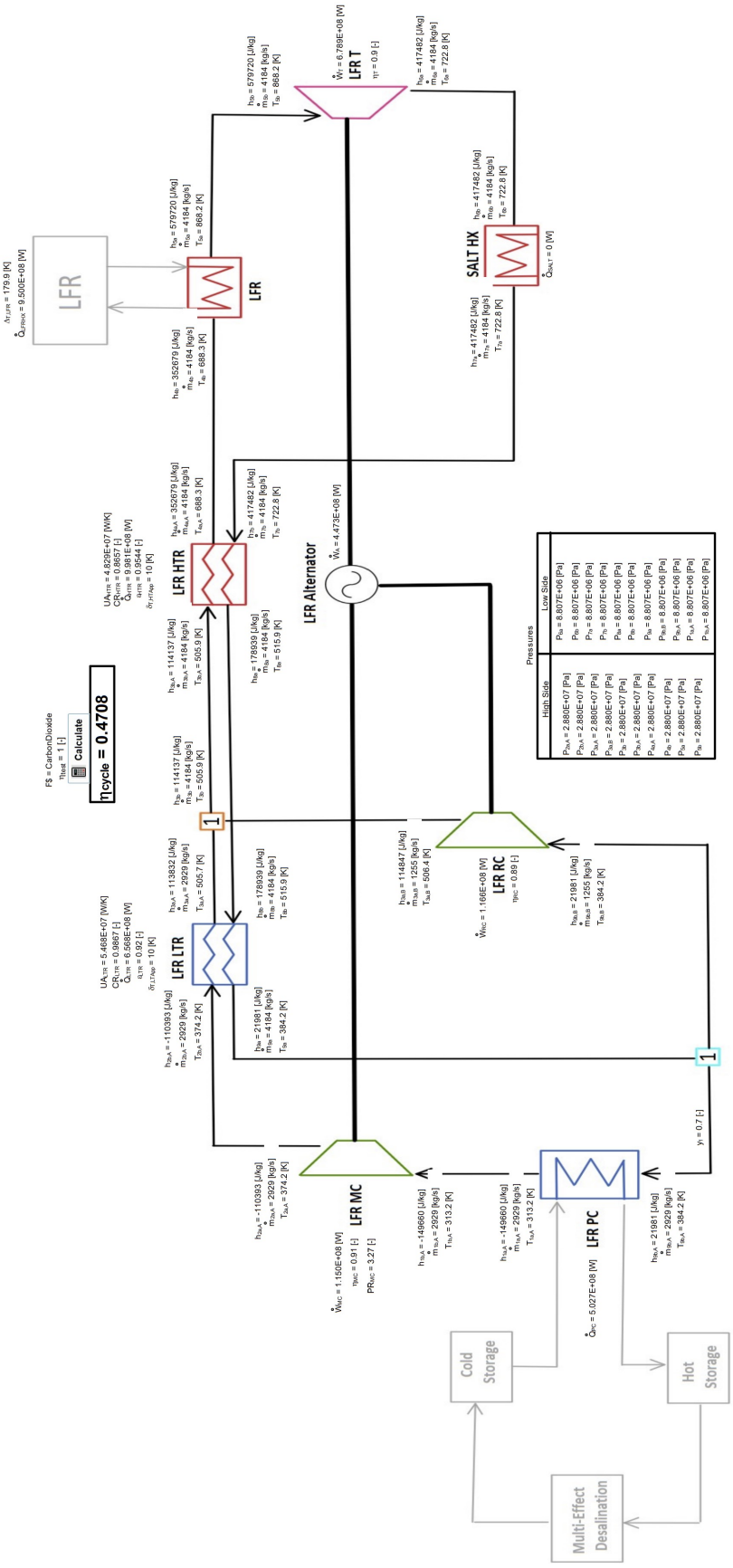

Figure C.4: State point diagram of sCO_2 Brayton Cycle C-LFR-ON without LFR low temperature restrictions

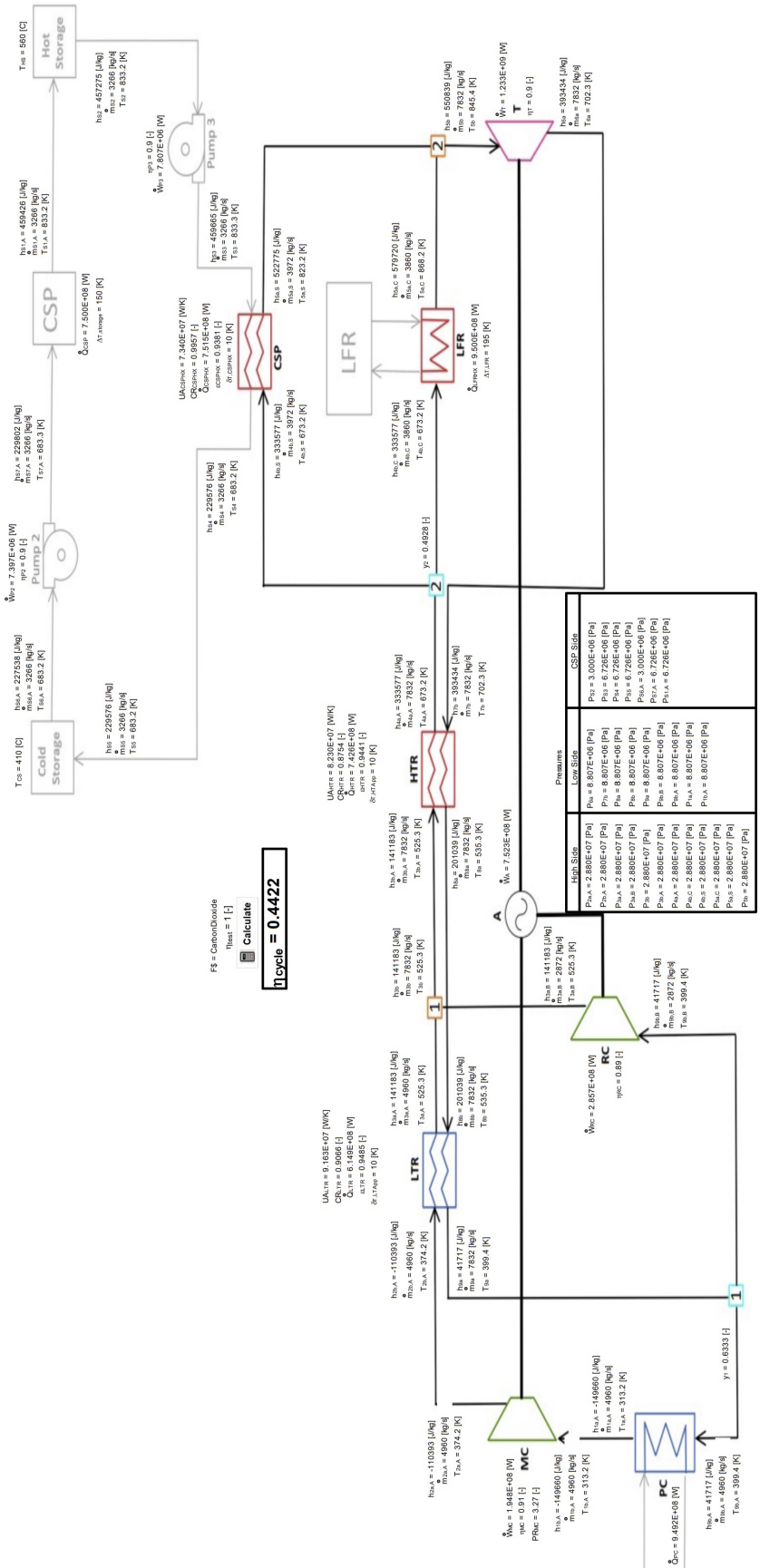

Figure C.5: sCO_2 Brayton Cycle C-1HTR1T-ON operating with cold storage of 410 C

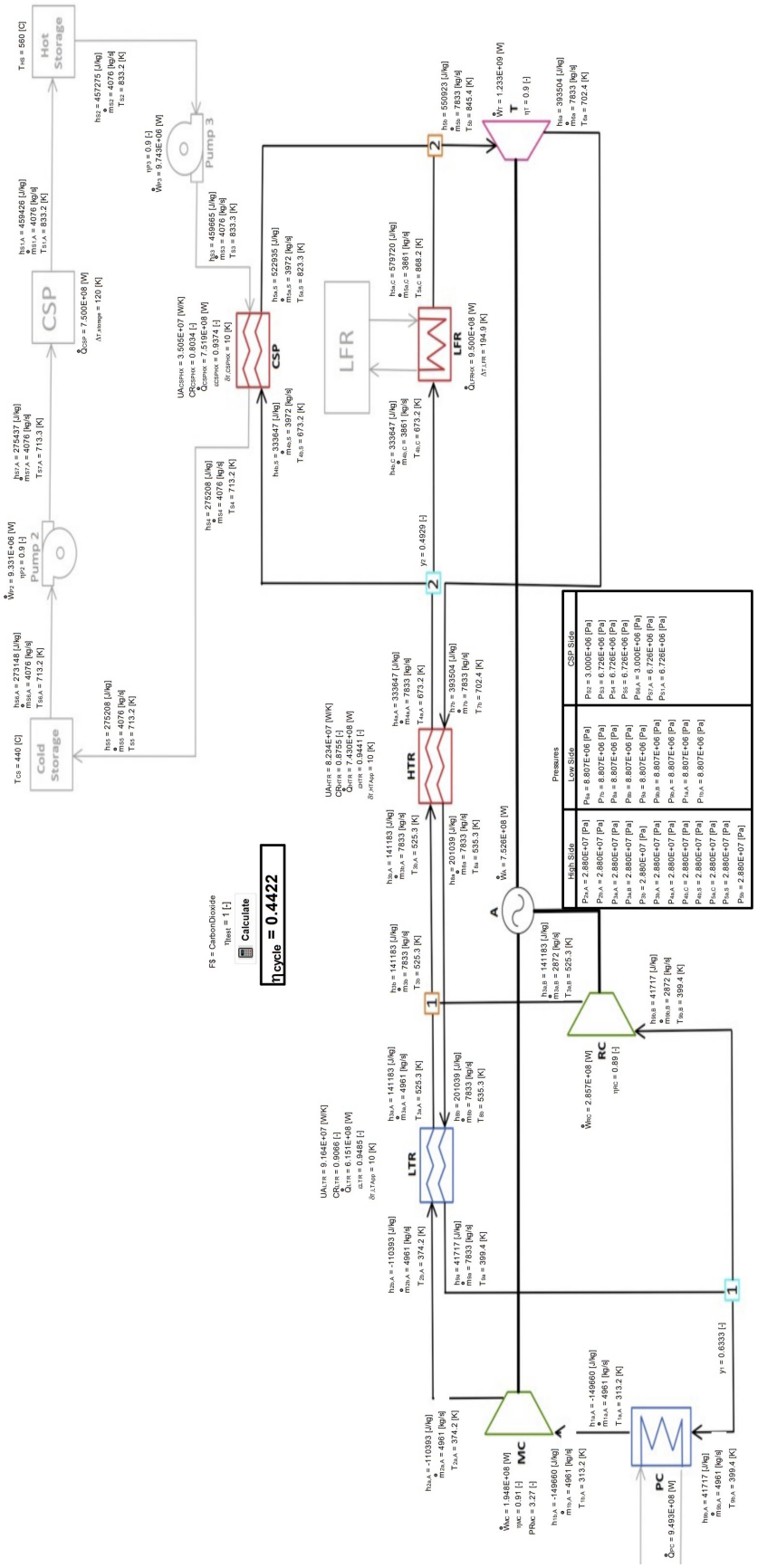

Figure C.6: sCO_2 Brayton Cycle C-1HTR1T-ON operating with cold storage of 440 C

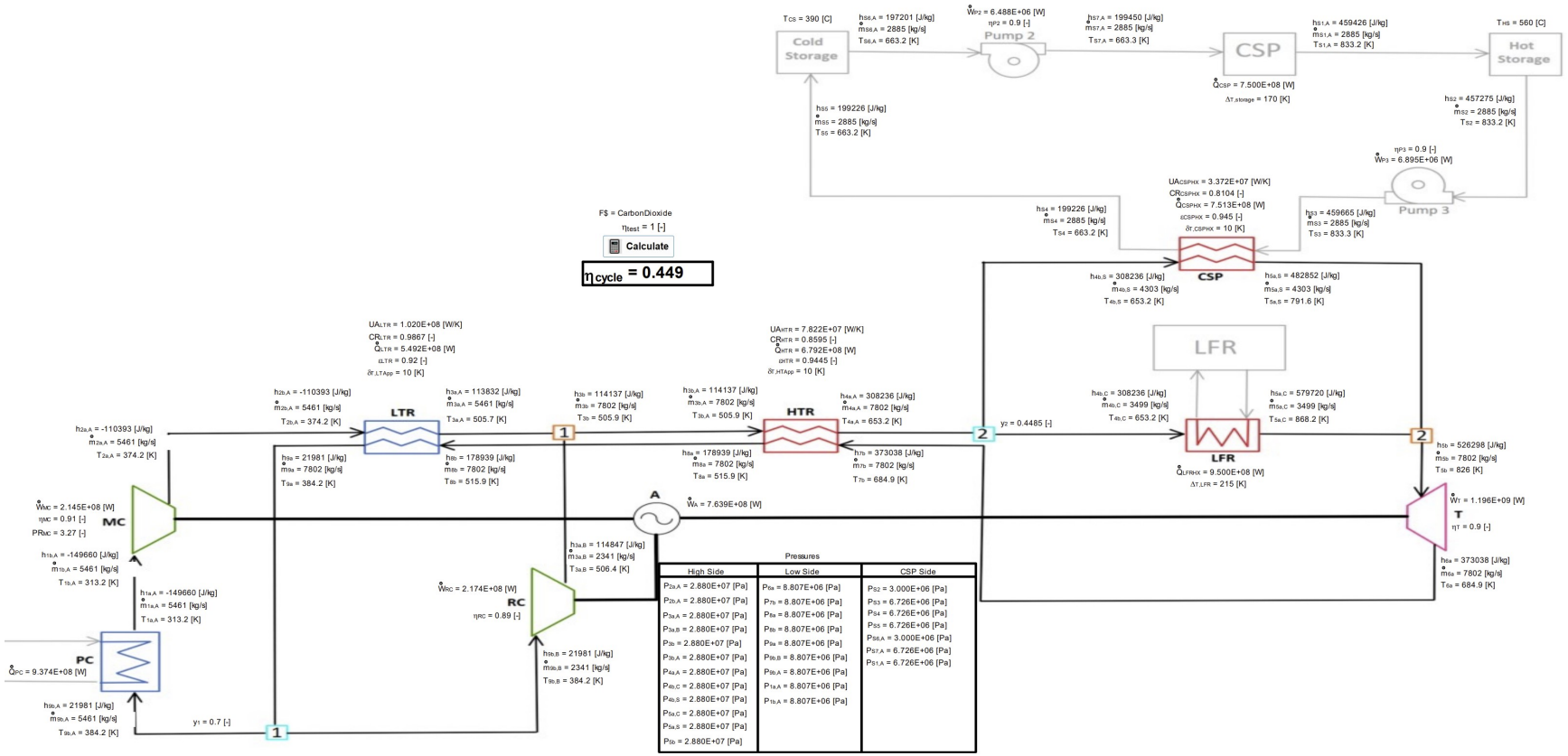

Figure C.7: sCO_2 Brayton Cycle C-1HTR1T-ON operating with cold storage of 390 C and no low temperature restriction on the LFR inlet

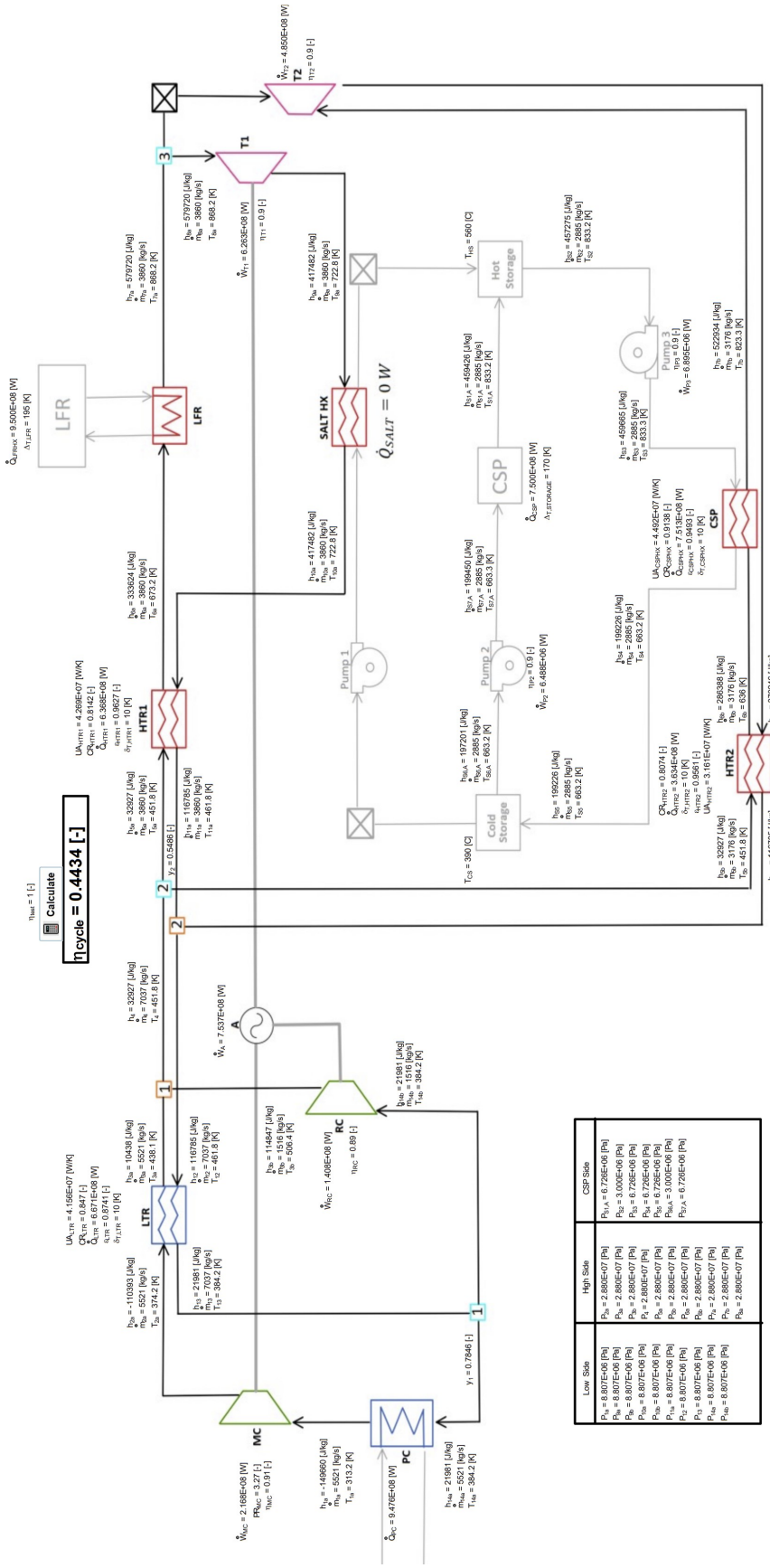

Figure C.8: sCO_2 Brayton Cycle C-2HTR3T-ON operating with cold storage of 390 C

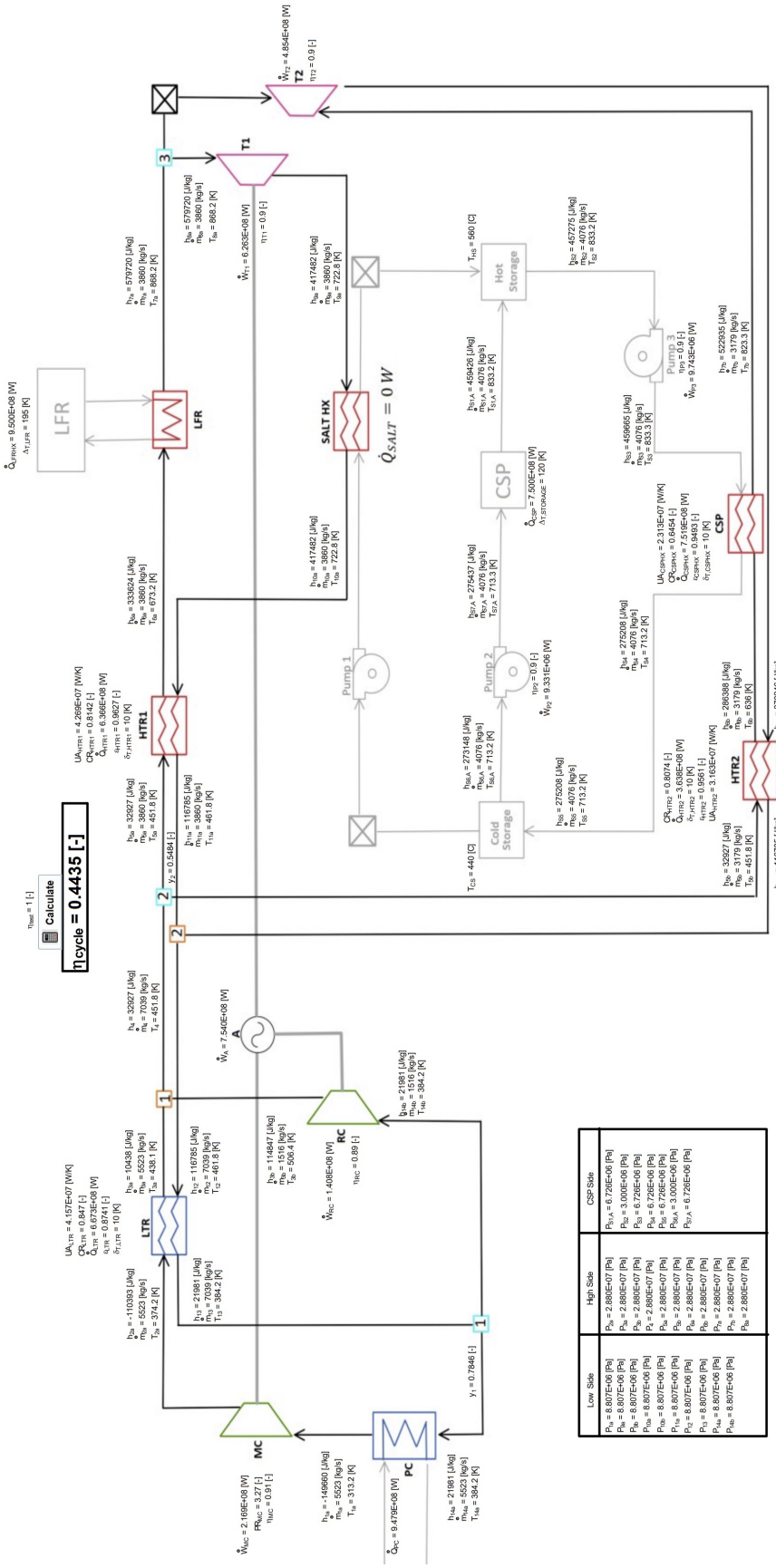

Figure C.9: sCO_2 Brayton Cycle C-2HTR3T-ON operating with cold storage of 440 C

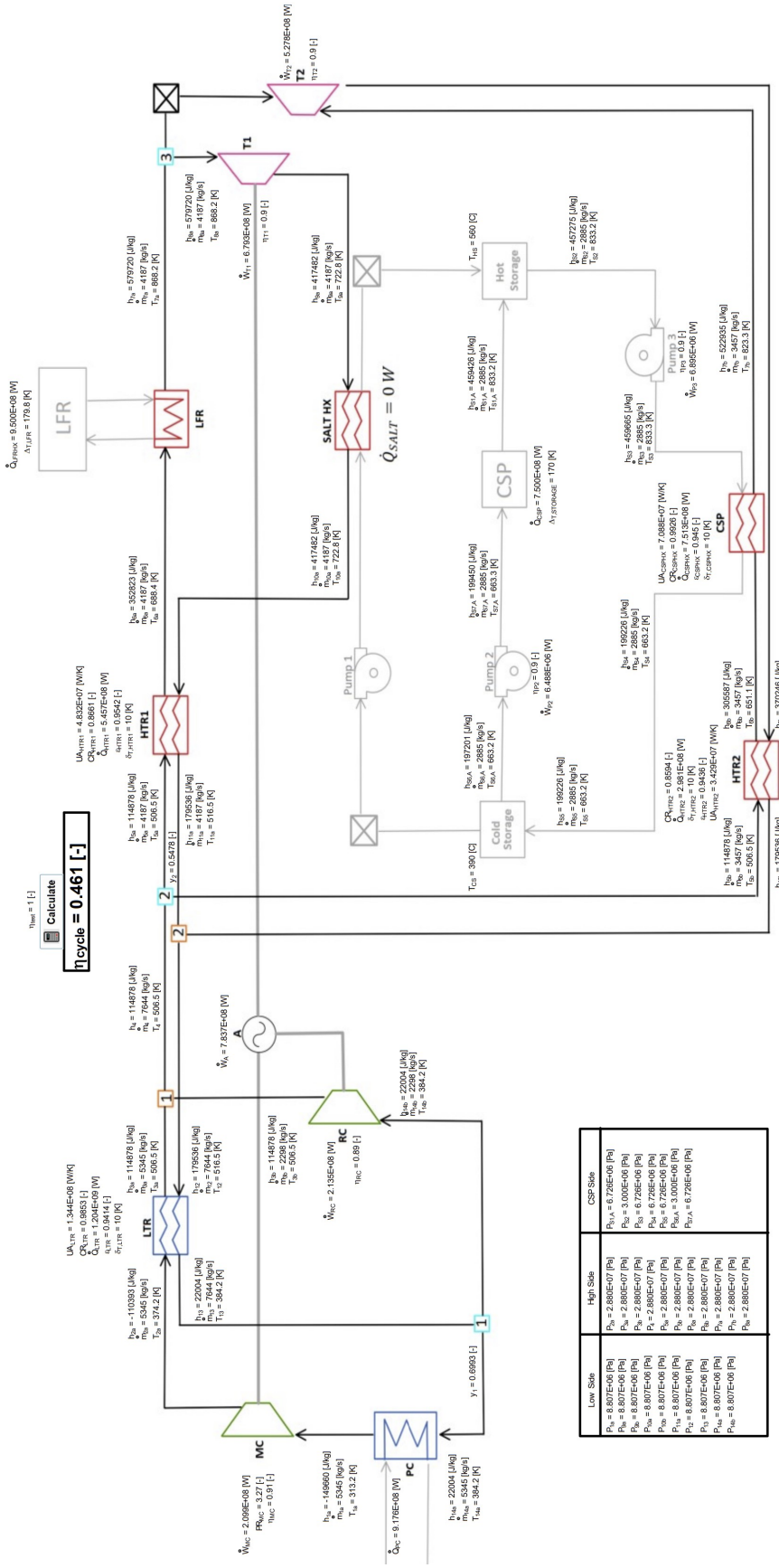

Figure C.10: sCO_2 Brayton Cycle C-2HTR3T-ON operating with cold storage of 390 C and no low temperature restriction on LFR inlet

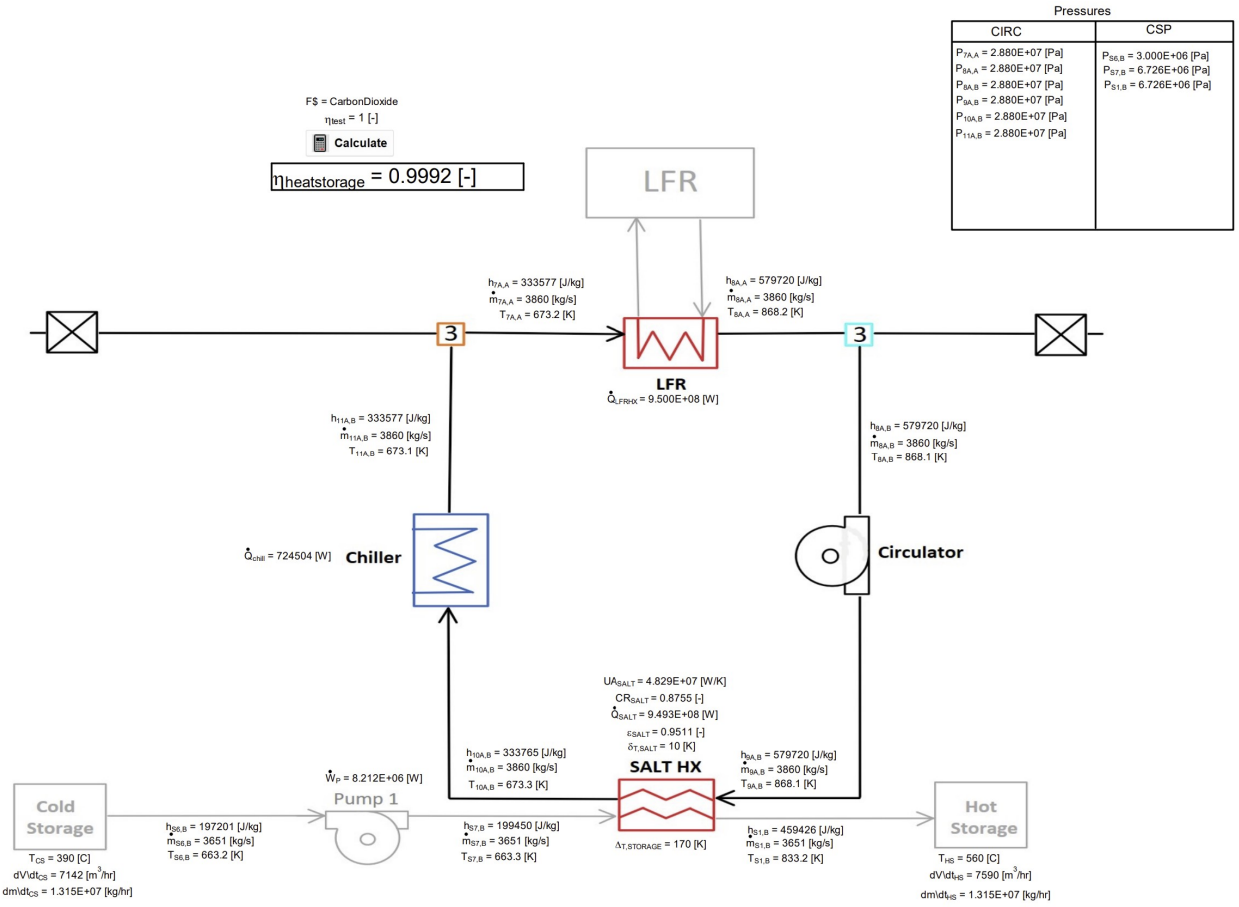

Figure C.11: sCO_2 Brayton Cycle C-LFR-CIRC operating with cold storage of 390 C

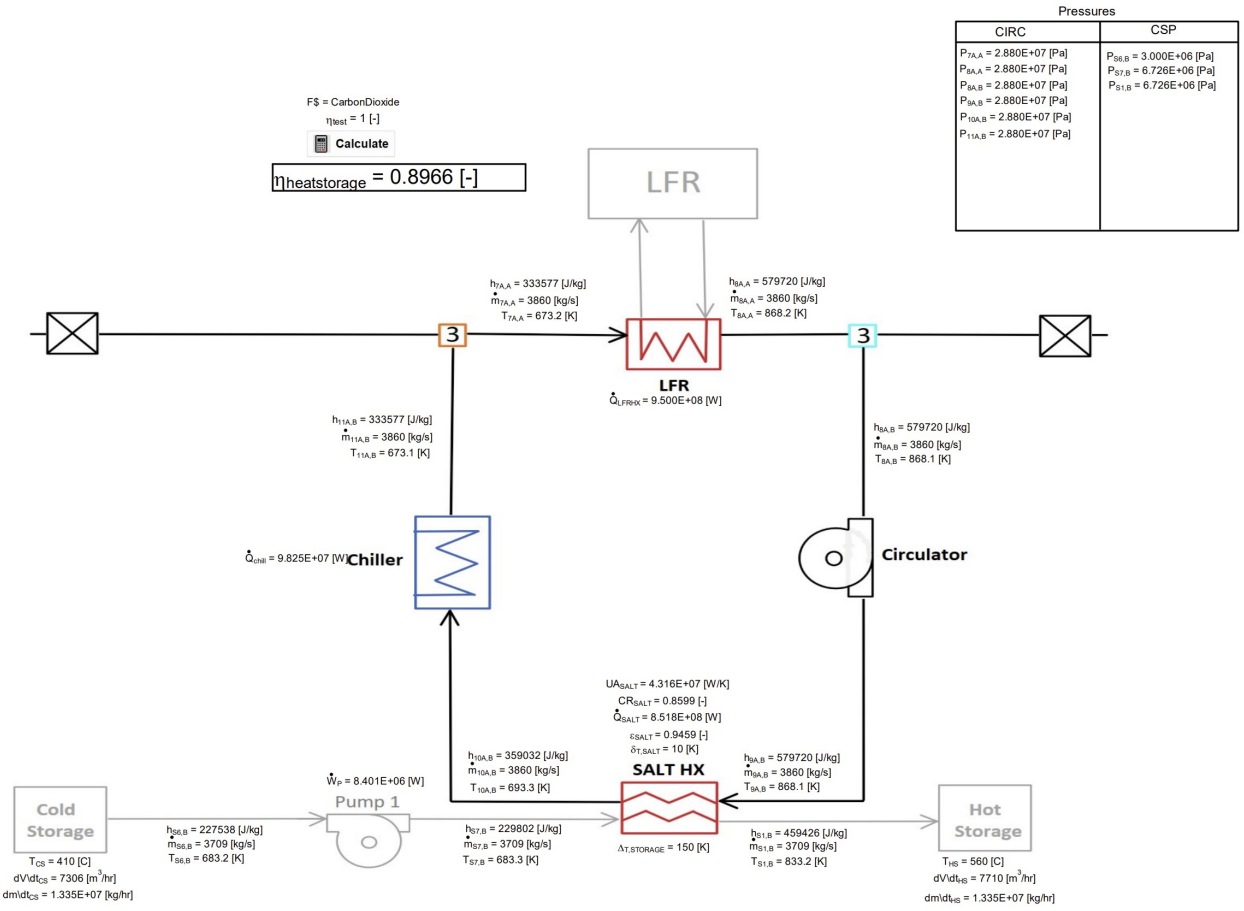

Figure C.12: sCO_2 Brayton Cycle C-LFR-CIRC operating with cold storage of 410 C

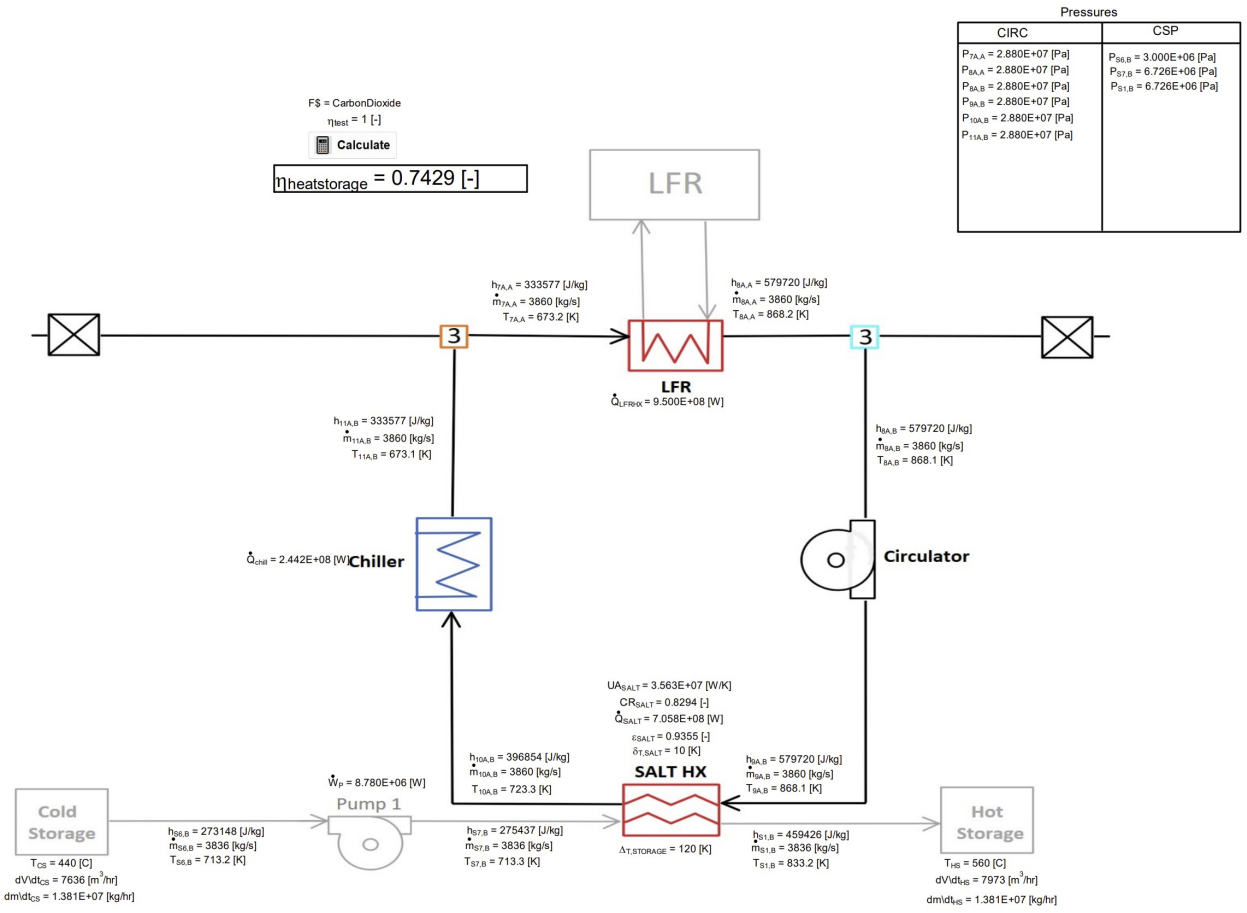

Figure C.13: sCO_2 Brayton Cycle C-LFR-CIRC operating with cold storage of 440 C

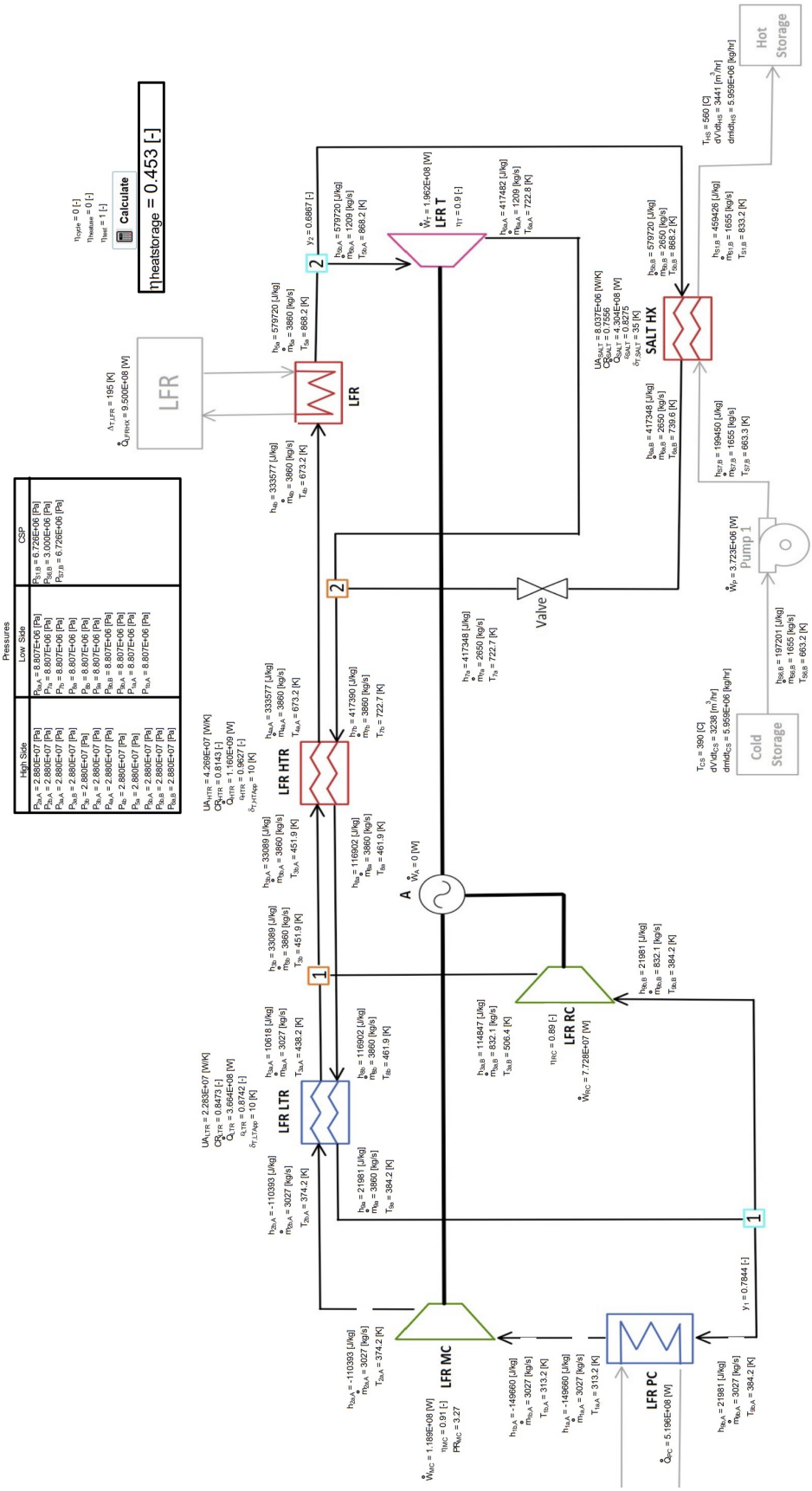

Figure C.14: sCO_2 Brayton Cycle C-LFR-PAR operating with cold storage of 390 C

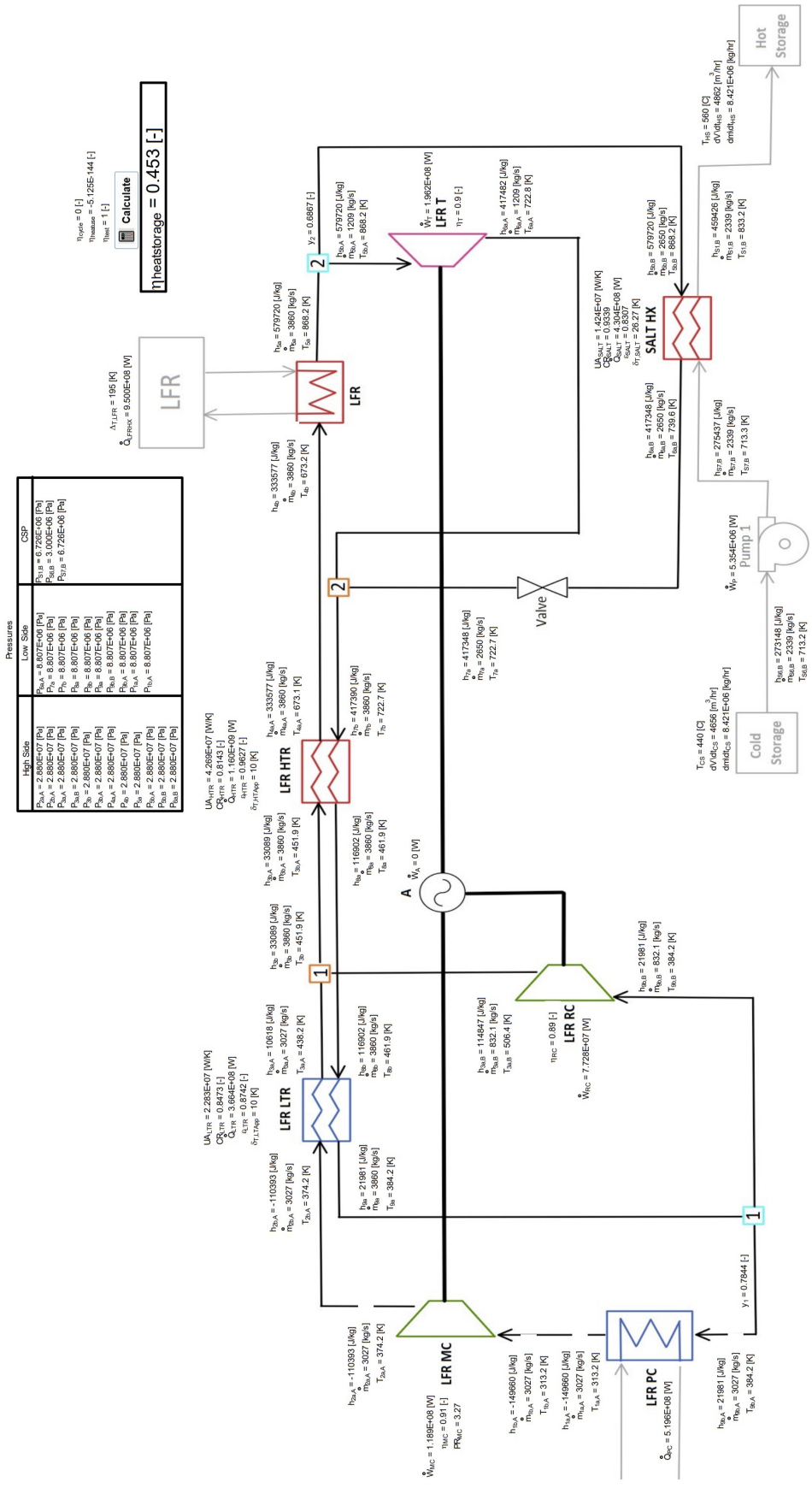

Figure C.15: sCO_2 Brayton Cycle C-LFR-PAR operating with cold storage of 440 C

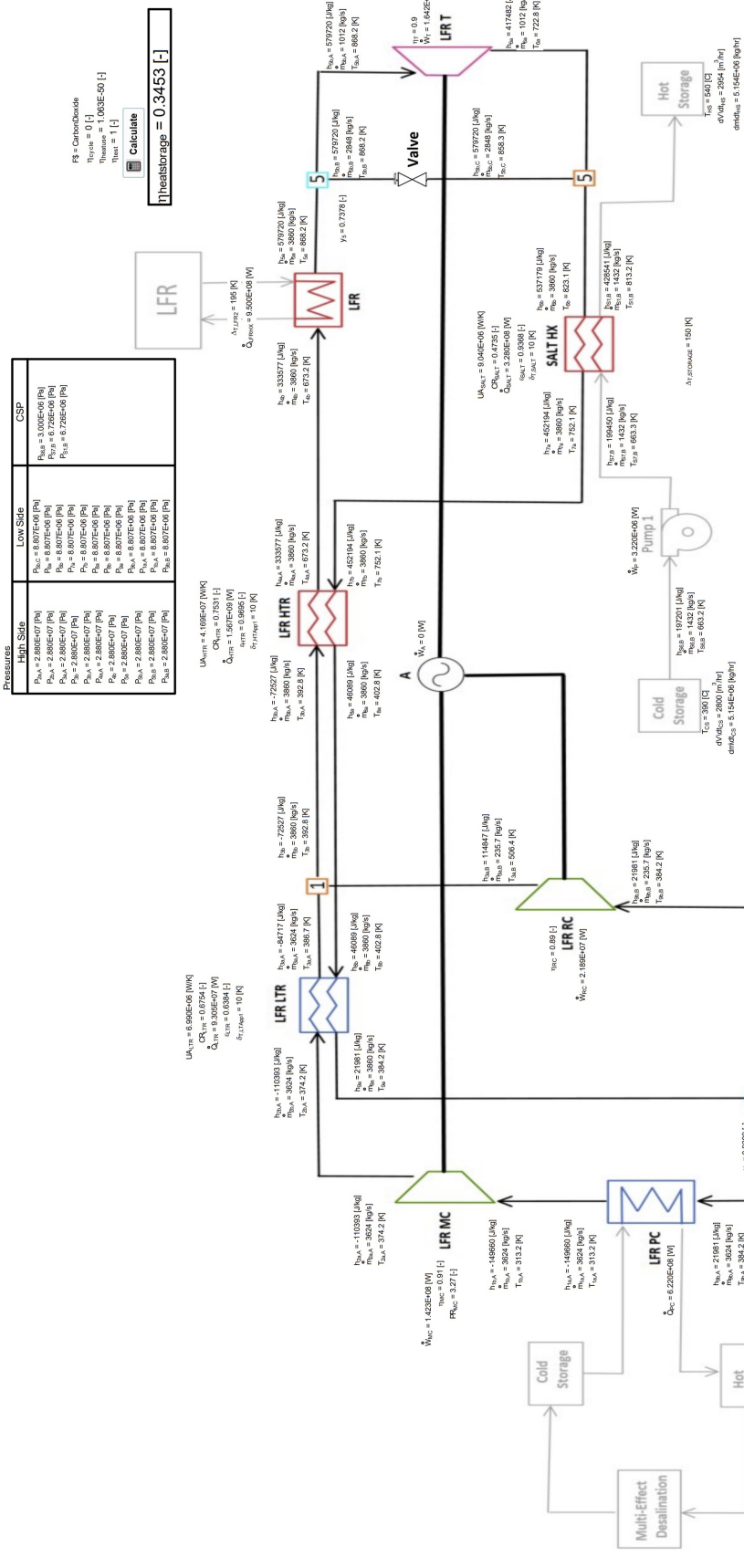

Figure C.16: sCO_2 Brayton Cycle C-LFR-PRE operating with hot storage of 540 C

REFERENCES

[1] Soto, Gabriel J, Una Baker, Brian White, Ben Lindley, and Mike Wagner. 2021. Modeling a lead-cooled fast reactor with thermal energy storage using optimal dispatch and sam. *Transactions of the American Nuclear Society* 125(2116).

[2] U.S. Energy Information Administration. 2022. Net generation by energy source: Total (all sectors), 2012-june 2022.

[3] Ferreira, Helder Lopes, Raquel Garde, Gianluca Fulli, Wil Kling, and Joao Pecas Lopes. 2013. Characterisation of electrical energy storage technologies. *Energy* 53:288–298.

[4] Ait Lahoussine Ouali, Hanane, Benyounes Raillani, Samir Amraqui, Mohammed Amine Moussaoui, Abdelhamid Mezrhab, and Ahmed Mezrhab. 2019. Analysis and optimization of sm and tes hours of central receiver concentrated solar thermal with two-tank molten salt thermal storage. In *International conference on smart information & communication technologies*, 666–673. Springer.

[5] Ferroni, Paolo. 2021. Westinghouse lead fast reactor design and safety.

[6] El-Wakil, Mohamed Mohamed. 1984. Powerplant technology.

[7] Turchi, Craig S, Zhiwen Ma, Ty W Neises, and Michael J Wagner. 2013. Thermodynamic study of advanced supercritical carbon dioxide power cycles for concentrating solar power systems. *Journal of Solar Energy Engineering* 135(4).

[8] Ahn, Yoon Han, Seong Jun Bae, Min Seok Kim, Seong Kuk Cho, Seung Joon Baik, Jeong Ik Lee, and Jae Eun Cha. 2014. Cycle layout studies of s-co2 cycle for the next generation nuclear system application. In *The korean nuclear society autumn meeting (2014)*. The Korean Nuclear Society.

[9] Wang, Kun, Ming-Jia Li, Jia-Qi Guo, Peiwen Li, and Zhan-Bin Liu. 2018. A systematic comparison of different s-co2 brayton cycle layouts based on multi-objective optimization for applications in solar power tower plants. *Applied Energy* 212:109–121.

[10] Wright, Steven A., Paul S. Pickard, Robert Fuller, Ross F. Radel, and Milton E. Vernon. 2009. Supercritical CO2 Brayton Cycle Power Generation Development Program and Initial Test Results ASME 2009 Power Conference:573–583.

[11] Margolis, R., C. Coggeshall, and J. Zuboy. 2012. U.S. Department of Energy, Sunshot Vision Study. `https://www.energy.gov/eere/solar/sunshot-vision-study`. Accessed: 8-20-21.

[12] Mehos, Mark, Craig Turchi, Judith Vidal, Michael Wagner, Zhiwen Ma, Clifford Ho, William Kolb, Charles Andraka, and Alan Kruizenga. 2017. Concentrating solar power gen3 demonstration roadmap. Tech. Rep., National Renewable Energy Lab.(NREL), Golden, CO (United States).

[13] NETL. 2016. Supercritical Carbon Dioxide Pilot Plant Test Facility. `https://netl.doe.gov/project-information?p=FE0028979`. Accessed: 8-30-21.

[14] Brayton Energy. 2015. Brayton Energy. `https://www.energy.gov/eere/solar/project-profile-brayton-energy`. Accessed: 8-30-21.

[15] Iverson, Brian D, Thomas M Conboy, James J Pasch, and Alan M Kruizenga. 2013. Supercritical co2 brayton cycles for solar-thermal energy. *Applied Energy* 111:957–970.

[16] Al-Sulaiman, Fahad A., and Maimoon Atif. 2015. Performance comparison of different supercritical carbon dioxide brayton cycles integrated with a solar power tower. *Energy* 82:61–71.

[17] Ho, Clifford K., Matthew Carlson, Pardeep Garg, and Pramod Kumar. 2015. Cost and performance tradeoffs of alternative solar-driven s-co2 brayton cy-

cle configurations. In *Asme 2015 9th international conference on energy sustainability*. https://asmedigitalcollection.asme.org/ES/proceedings-pdf/ES2015/56840/V001T05A016/4448498/v001t05a016-es2015-49467.pdf.

[18] Neises, Ty. 2020. Steady-state off-design modeling of the supercritical carbon dioxide recompression cycle for concentrating solar power applications with two-tank sensible-heat storage. *Solar Energy* 212:19–33.

[19] Dostal, Vaclav. 2004. A supercritical carbon dioxide cycle for next generation nuclear reactors. Ph.D. thesis, Massachusetts Institute of Technology.

[20] Luo, Dan, and Diangui Huang. 2020. Thermodynamic and exergoeconomic investigation of various sco2 brayton cycles for next generation nuclear reactors. *Energy Conversion and Management* 209:112649.

[21] Wright, Steven Alan, Thomas M Conboy, and Gary Eugene Rochau. 2011. Break-even power transients for two simple recuperated s-co2 brayton cycle test configurations. Tech. Rep., Sandia National Lab.(SNL-NM), Albuquerque, NM (United States).

[22] Cha, Jae Eun, Seong Won Bae, Jekyoung Lee, Seong Kuk Cho, Jeong Ik Lee, and Joo Hyun Park. 2016. Operation results of a closed supercritical co2 simple brayton cycle. In *Proceedings of the 5th international symposium-supercritical co2 power cycles, san antonio, tx, usa*, 28–31.

[23] Held, Timothy J. 2015. Suipercritical co2 cycles for gas turbine combined cycle power plants. In *Power gen international*.

[24] Fetvedt, Jeremy. 2016. Development of the sco2 allam cycle. In *Supercritical co2 power cycles symposium*.

[25] Office of Energy Efficiency and Renewable Energy. 2020. SETO 2020 – Integrated TESTBED – Heliogen, Inc. https://www.energy.gov/eere/solar/seto-2020-integrated-testbed-heliogen-inc. Accessed: 12-04-21.

[26] Monnerie, Nathalie, Mark Schmitz, Martin Roeb, Dominik Quantius, Daniela Graf, Christian Sattler, and Daniel De Lorenzo. 2011. Potential of hybridisation of the thermochemical hybrid-sulphur cycle for the production of hydrogen by using nuclear and solar energy in the same plant. *International Journal of Nuclear Hydrogen Production and Applications* 2(3):178–201.

[27] Curtis, Daniel Joseph. 2015. Nuclear renewable oil shale hybrid energy systems: configuration, performance, and development pathways. Ph.D. thesis, Massachusetts Institute of Technology.

[28] Wang, Gang, Cheng Wang, Zeshao Chen, and Peng Hu. 2020. Design and performance evaluation of an innovative solar-nuclear complementarity power system using the s–co2 brayton cycle. *Energy* 197:117282.

[29] Son, In Woo, Yong Hoon Jeong, Young Jae Choi, and Jeong Ik Lee. 2021. Feasibility study of solar-nuclear hybrid system for distributed power source. *Energy Conversion and Management* 230:113808.

[30] Turchi, Craig S, Judith Vidal, and Matthew Bauer. 2018. Molten salt power towers operating at 600–650 c: Salt selection and cost benefits. *Solar Energy* 164:38–46.

[31] Carlson, Fletcher, Jane H Davidson, Nam Tran, and Andreas Stein. 2019. Model of the impact of use of thermal energy storage on operation of a nuclear power plant rankine cycle. *Energy Conversion and Management* 181:36–47.

[32] Carlson, Fletcher, and Jane H Davidson. 2021. Parametric study of thermodynamic and cost performance of thermal energy storage coupled with nuclear power. *Energy Conversion and Management* 236:114054.

[33] Meroueh, Laureen, and Gang Chen. 2020. Thermal energy storage radiatively coupled to a supercritical rankine cycle for electric grid support. *Renewable Energy* 145:604–621.

[34] Wang, Gang, and Junhui Yin. 2020. Design and exergy evaluation of a novel parabolic trough solar-nuclear combined system. *Annals of Nuclear Energy* 144.

[35] Popov, Dimityr, and Ana Borissova. 2017. Innovative configuration of a hybrid nuclear-solar tower power plant. *Energy* 125:736–746.

[36] Wang, Gang, Junhui Yin, Jianqing Lin, Zeshao Chen, and Peng Hu. 2021. Design and economic analysis of a novel hybrid nuclear-solar complementary power system for power generation and desalination. *Applied Thermal Engineering* 187:116564.

[37] Zhao, Bing-chen, Mao-song Cheng, Chang Liu, and Zhi-min Dai. 2018. Conceptual design and preliminary performance analysis of a hybrid nuclear-solar power system with molten-salt packed-bed thermal energy storage for on-demand power supply. *Energy Conversion and Management* 166:174–186.

[38] Miller, Jason D, David J Buckmaster, Katherine Hart, Timothy J Held, David Thimsen, Andrew Maxson, Jeffrey N Phillips, and Scott Hume. 2017. Comparison of supercritical co2 power cycles to steam rankine cycles in coal-fired applications. In *Turbo expo: Power for land, sea, and air*, vol. 50961, V009T38A026. American Society of Mechanical Engineers.

[39] Xu, Jinliang, Xue Wang, Enhui Sun, and Mingjia Li. 2021. Economic comparison between sco2 power cycle and water-steam rankine cycle for coal-fired power generation system. *Energy Conversion and Management* 238:114150.

[40] Cheang, VT, RA Hedderwick, and C McGregor. 2015. Benchmarking supercritical carbon dioxide cycles against steam rankine cycles for concentrated solar power. *Solar Energy* 113:199–211.

[41] Garg, P, K Srinivasan, P Dutta, and P Kumar. 2014. Comparison of co2 and steam in transcritical rankine cycles for concentrated solar power. *Energy procedia* 49:1138–1146.

[42] Dostal, Vaclav, Pavel Hejzlar, and Michael J Driscoll. 2006. The supercritical carbon dioxide power cycle: comparison to other advanced power cycles. *Nuclear technology* 154(3):283–301.

[43] Klein, Sanford, and Gregory Nellis. 2011. *Thermodynamics*. Cambridge University Press.

[44] Seidel, William. 2010. Model development and annual simulation of the supercritical carbon dioxide brayton cycle for concentrating solar power applications. Ph.D. thesis, University of Wisconsin - Madison.

[45] Pacheco, J E, M E Ralph, J M Chavez, S R Dunkin, E E Rush, C M Ghanbari, and M W Matthews. 1995. Results of molten salt panel and component experiments for solar central receivers: Cold fill, freeze/thaw, thermal cycling and shock, and instrumentation tests.

[46] Span, Roland, and Wolfgang Wagner. 1996. A new equation of state for carbon dioxide covering the fluid region from the triple-point temperature to 1100 k at pressures up to 800 mpa. *Journal of Physical and Chemical Reference Data* 25(6):1509–1596. https://doi.org/10.1063/1.555991.

[47] Nellis, Gregory, and Sanford Klein. 2008. *Heat transfer*. Cambridge University Press.

[48] Dyreby, John J. 2014. Modeling the supercritical carbon dioxide brayton cycle with recompression. Ph.D. thesis, University of Wisconsin-Madison. Copyright - Database copyright ProQuest LLC; ProQuest does not claim copyright in the individual underlying works; Last updated - 2021-10-26.

[49] Smith, C.F., and L. Cinotti. 2016. 6 - lead-cooled fast reactor. In *Handbook of generation iv nuclear reactors*, ed. Igor L. Pioro, 119–155. Woodhead Publishing Series in Energy, Woodhead Publishing.

[50] Alemberti, Alessandro, Valery Smirnov, Craig F. Smith, and Minoru Takahashi. 2014. Overview of lead-cooled fast reactor activities. *Progress in Nuclear Energy* 77:300–307.

[51] Hamilton, William T, Mark A Husted, Alexandra M Newman, Robert J Braun, and Michael J Wagner. 2020. Dispatch optimization of concentrating solar power with utility-scale photovoltaics. *Optimization and Engineering* 21(1):335–369.

[52] Salazar-Pereyra, Martín, Raúl Lugo-Leyte, Angélica Elizabeth Bonilla-Blancas, and Helen Denise Lugo-Méndez. 2016. Thermodynamic analysis of supercritical and subcritical rankine cycles. In *Turbo expo: Power for land, sea, and air*, vol. 49866, V008T26A041. American Society of Mechanical Engineers.

[53] Patnode, Angela M. 2006. Simulation and performance evaluation of parabolic trough solar power plants. Master's thesis.

[54] Hamilton, William T, Alexandra M Newman, Michael J Wagner, and Robert J Braun. 2020. Off-design performance of molten salt-driven rankine cycles and its impact on the optimal dispatch of concentrating solar power systems. *Energy Conversion and Management* 220:113025.

[55] Manabe, Jun, Jiro Kasahara, Issaku Fujita, and Toshiki Kojima. 2010. Recent moisture separator reheater design technologies. *Journal of engineering for gas turbines and power* 132(10).

[56] Sato, Hideaki, Soichiro Tabata, Naoto Tochitani, Yasuhiro Sasao, Ryo Takata, and Masaki Osako. 2020. Investigation of Moisture Removal on Last Stage Stationary Blade in Actual Steam Turbine Volume 9: Oil and Gas Applications; Organic Rankine Cycle Power Systems; Steam Turbine.

[57] Hoznedl, Michal, Ladislav Tajč, Lukáš Bednář, Aleš Macálka, and Antonín Živný. 2019. Separation of Water Film From Last Stage Guide Blades of 1000 MW Steam

Turbine Volume 8: Microturbines, Turbochargers, and Small Turbomachines; Steam Turbines.

[58] Bartlett, Robert L, JE Mulder, and RC Sheldon. 1958. *Steam turbine performance and economics*. McGraw-Hill.

[59] Weinstein, Lee A, James Loomis, Bikram Bhatia, David M Bierman, Evelyn N Wang, and Gang Chen. 2015. Concentrating solar power. *Chemical Reviews* 115(23):12797–12838.

[60] Weitzel, Paul S. 2011. Steam generator for advanced ultra supercritical power plants 700c to 760c. In *Asme power conference*, vol. 44595, 281–291.